Understanding the Photodissociation Dynamics of Molecular Cluster Ions

by

Nicole D. Delaney

B.S., Massachusetts Institute of Technology, 1992

A thesis submitted to the

Faculty of the Graduate School of the

University of Colorado in partial fulfillment

of the requirements for the degree of

Doctor of Philosophy

Committee on Physical Chemistry

1999

This thesis entitled:
Understanding the Photodissociation Dynamics of Molecular Cluster Ions
written by Nicole D. Delaney
has been approved for the Committee on Physical Chemistry

Robert Parson

W. Carl Lineberger

Date

The final copy of this thesis has been examined by the signatories, and we find that both the content and the form meet acceptable presentation standards of scholarly work in the above mentioned discipline.

Delaney, Nicole D. (Ph.D. Physical Chemistry)

Understanding the Photodissociation Dynamics of Molecular Cluster Ions

Thesis directed by Associate Professor Robert Parson

The effects of solvation on the photodissociation and recombination of I_2^- are studied through nonadiabatic molecular dynamics simulations, using an effective Hamiltonian that accounts for the strong perturbation of the solute electronic structure by the solvent. Methods for analyzing the simulations are developed, including a two-dimensional model for the excited stated dynamics, derived from the theory of electron transfer reactions in solution.

The primary focus is understanding the photodissociation of $I_2^-(CO_2)_n$ clusters. The experimental absorption recovery signal for clusters with $n > 13$ features an enhanced absorption peak, 2 ps after the initial excitation of I_2^-. We present evidence that this feature is due to transitions from the ground state to the spin-orbit excited states, rather than to excited-state absorption as previously assigned. Previously, this possibility was ruled out because the experiments also indicated that the final products contained I_2^- in its lower spin orbit state and there was no known mechanism for spin-orbit relaxation occuring on the experimental detection timescale. Simulations of the photodissociation of $I_2^-(CO_2)_n$ clusters at 395 nm reveal an efficient mechanism for the spin-orbit relaxation of I_2^- via a solvent mediated charge transfer process, and this has subsequently been observed experimentally.

The existence of a strong absorption from the ground state of I_2^- to the spin-orbit excited states affects the interpretation of other experimental measurements on these systems. The dynamics simulations of $I_2^-(CO_2)_n$ and $I_2^-Ar_n$ clusters are analyzed in an effort to shed light on the experimental results.

to the tortoise.

Acknowledgements

My thanks to my advisor, Robert Parson, for letting me join the group at a time when my computing experience barely extended beyond checking my email, for having the faith to let me find my own way to do research, and for all the assistance in pulling this thesis together.

Paul Maslen taught me more than I thought I would ever know about the world of electronic structure calculations. All that time we spent poring over data files that were never intended to be read by human eyes turned out to be perfect training for analyzing the dynamics simulations too!

I'm not sure it's possible to thank Jim Faeder enough for his contributions to this work, and my graduate career in general. Thanks for designing and maintaining all that code. Thanks for patiently fielding so many questions, and for getting impatient when I really needed to just go figure it out for myself. Thanks for setting such a great example of how to do careful, meaningful science. Thanks for being open to my point of view, and for hearing me out even when we disagreed. Thanks for listening to my doubts and fears and for helping me overcome them. Thanks for being a great friend.

It has been very satisfying to work on a project aimed at integrating lessons learned from theoretical simulations and laboratory observations and I would like to thank all of my experimental collaborators. Carl Lineberger has generously shared his ideas and enthusiasm, and I appreciate the dedication to our common goal he has shown by allowing me to pick apart and reinterpret the results from his research group.

John Papanikolas, Sreela Nandi and Andrei Sanov have been invaluable in providing the inside story on their experimental work. John's exceptional scientific insight is matched by his ability to convey information clearly. In the early days of my graduate career, his talks and papers captured my attention and curiosity and the questions he posed have served as a guide for my research. My thanks to Sreela for so patiently re-explaining how the experiments really work each time I asked, and for pushing me to work on OCS. Chapter 7 is the result of our combined efforts. Thanks to past and present Lineberger group members Vasil Vorsa, Maria Nadal, Todd Sanford, Paul Campagnola, and Nancy Levinger.

Over the past few years, I have also had the pleasure of working with Dan Neumark's group from Berkeley. Their results provided an opportunity for us to test our ideas about the dynamics just when we needed it. I especially thank Jeff Greenblatt and Marty Zanni for sharing their data and for many helpful discussions.

My thanks to the JILA staff for all the assistance and friendship. To Ralph Mitchell, Joel Frahm, Alan Dunwell, Nick Metrowsky, Peter Ruprecht, Anne Hammond and Chela Kunasz, thanks for looking after our computing resources. Chela, thanks too for all the inspiration and encouragement. To Karen Melcher, thanks for being a kindred spirit and sharing your strength.

The teachers I've had throughout my life deserve enormous thanks for helping me get to where I am today. Two still stand out of the crowd. To Ms. Neale and Mr. Smith, thank you for all you taught me about being inquisitive and creative. Balancing my passions for art and science has kept me sane, and I hope it has enhanced the quality of the work I've produced.

To my pal, Scott Davis, thanks for being here. I can't even count the number of times I would have just walked away and quit if you hadn't been here cheering me up and cheering me on.

Thanks so much to all of the friends who have stuck by me through the years.

To Amie Strong, Jeanette Sperhac, Sarah Gallagher Faeder, Anita Krishnamurthi and Cindy Mrazek, thanks for all the surprise gifts, warm meals, advice, car rides, and most of all for letting me rant and rave to you. Thanks to all of my camping buddies for making the last few months so much fun.

To my family, thank you for always expecting the best from me. Thank you for being there to support me as I pushed the limits of my capabilities. Thank you for reminding me to do what makes me happy. None of this would have been possible without your love and encouragement.

Contents

Chapter

Figures

Figure

Tables

Table

Chapter 1

Understanding Photodissociation of Molecular Cluster Ions

The fable of the blind men and the elephant [1] teaches us that to reveal the true nature of something mysterious and new we must be careful not to draw our conclusions from any one fragment of information, but rather incorporate a wide range of observations. I have been fortunate to be involved in a course of research at a time when a critical mass of information has become available and it is possible to see how it can all fit together to reveal new insights. The challenge has been in reconciling seemingly contradictory data, filtering out misinformation and irrelevant details, and stripping away false assumptions. What results is a clearer view of the relatively simple pieces that create a complex but understandable whole.

Understanding the effects of solvation on simple chemical reactions is a central goal of chemical dynamics. Recent advances in modeling the photodissociation and recombination of dihalide anions in clusters have enabled us to make predictions of novel dynamics which can be, and in many cases have been, verified experimentally. Furthermore, the strong solute-solvent interactions which result from the charged nature of these systems open up reaction pathways that are not well described by traditional conceptualizations of the dynamics. Results of several recent experiments have the potential to teach us much more about the dynamics on excited electronic states, if we can learn to tease out the information from the experimental signals. This highlights the continued need for analysis of molecular dynamics calculations which reaches beyond

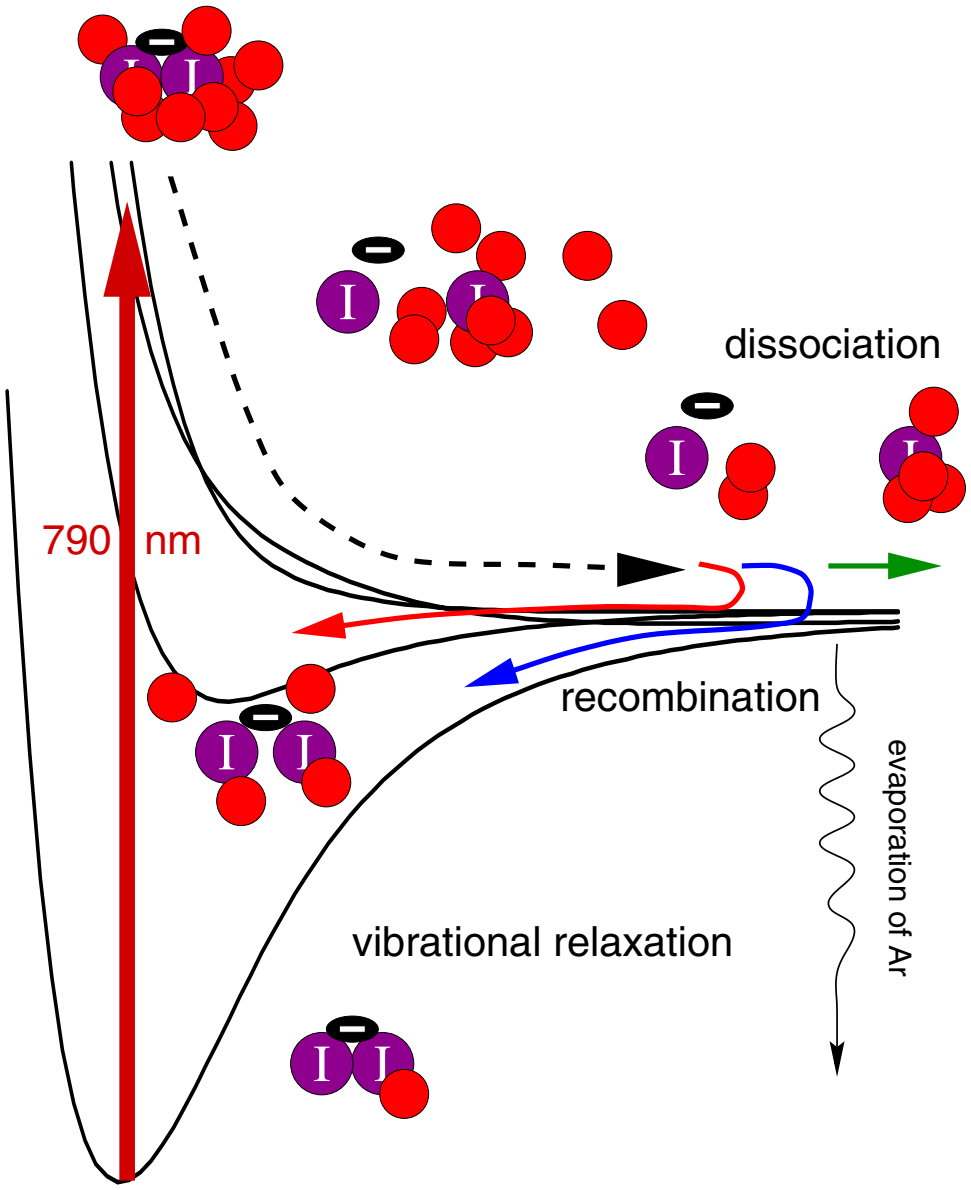

Figure 1.1: Photodissociation and recombination of solvated I_2^-.

comparing final product distributions and seeks to uncover the mechanisms through which the products form. The goal of this thesis is to explore the simulated dynamics and develop techniques to bring simulations to bear on experimental results.

An important lesson featured here is that the reaction dynamics of solvated molecular ions cannot be understood solely in terms of the potential curves of the isolated solute. Nevertheless, these curves provide a starting point for discussion. Figure 1.1

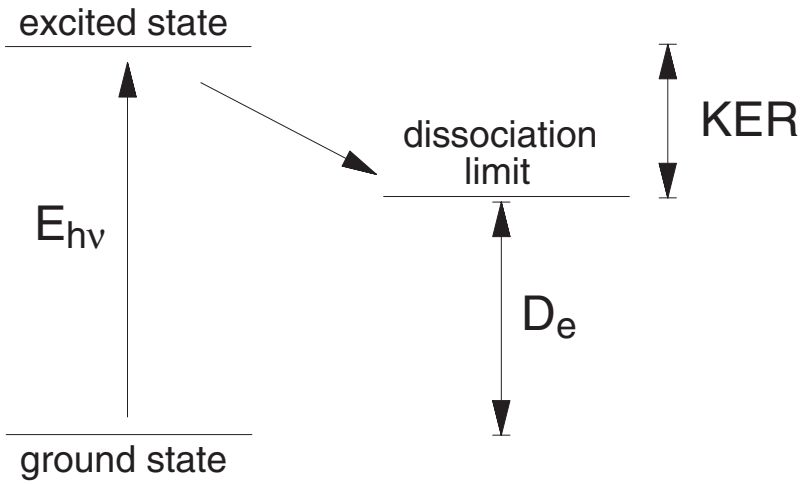

Figure 1.2: Energy disposal following solute excitation.

illustrates the photodissociation dynamics of I_2^- solvated by a small atomic cluster. The potential curves shown are the four lowest electronic states of the isolated solute. The thick arrow represents photoexcitation of I_2^- to a repulsive electronic state. As I_2^- breaks apart, the excess charge localizes onto one iodine atom and the fragments interact with the cluster atoms. In small and weakly bound clusters, the solute dissociates completely. When the interaction with the solvent is strong, dissociation is halted and the fragments recombine on either of the two lowest electronic states. Evaporation of solvent atoms from the cluster removes excess energy, allowing the solute to vibrationally relax.

What is missing from this picture is information about **how** the solvent exerts its influence on the photodissociation reaction. A conventional way to depict the solvent cage is to sketch in a repulsive wall from which the solute recoils at large bondlengths. This illustrates the role of "kinematic caging", which does play an important part in inducing recombination, but utterly fails to describe the Coulombic interactions between the solute and solvent, referred to as "electrostatic caging", which play a crucial role in the dissociation of solvated ions.

The interplay between the solute charge distribution and the solvent environment

is exemplified by the photodissociation of $I_2^-Ar_n$ clusters. In the photofragmentation experiments of Vorsa et al., $I_2^-Ar_n$ clusters were excited at 790 nm and the products were mass analyzed [2]. For intermediate cluster sizes ($n \approx 13$), a bimodal distribution was observed among the dissociative products, I^-Ar_k. One product channel remained peaked around $k = 1$ regardless of the initial cluster size, while the other channel reflected a loss of roughly 7 argon atoms ($k = n - 7$). The heavier products are consistent with the standard interpretation of the photodissociation process as illustrated above, which assumes that the amount of energy available for solvent evaporation is given by the photon energy minus the solute bondstrength, as shown in Fig. 1.2. The implicit assumption about the dynamics of the the process is that the I_2^- bond breaks, leaving I^- solvated by a hot cluster which evaporates argon atoms as it cools. Given this view of the reaction, it is difficult to account for the low mass products, and a satisfactory explanation did not surface until simulations revealed that a second mechanism is at work, in which I^- is ejected, leaving behind a neutral cluster [3]. At the source of this surprising behavior, which has been experimentally verified, is a phenomenon called anomalous charge flow, which will be discussed in detail beginning in Chapter 2. The point to be made here is that the interpretation presented in Fig. 1.1 leads us to believe there is a single dissociative asymptote for I_2^-, whereas in an asymmetric solvent environment, which shifts the relative energies of each electronic state, this is no longer true. The unanticipated dynamics resulting from the strong coupling between the solute and solvent are explored in this thesis. The implications of these results for the analysis of recent experimental findings are also considered.

1.1 Background

The term "caging" was first coined by Franck and Rabinovitch in the 1930's to describe the trapping and recombination of dissociating fragments induced by a solvent bath [4]. Further studies by Noyes and coworkers focused on determining how

excitation wavelength and solvent viscosity affect caging efficiency [5–8]. The first time-resolved experiments on I_2 photodissociation revealed that the overall process required from 50-200 ps up to nanoseconds, depending on the solvent [9]. Modeling of the process by Nesbitt and Hynes determined that the timescale was a measure of the slow vibrational relaxation, not electronic relaxation which was expected to be much faster [10]. This was followed by a second wave of I_2 experiments with better time resolution [11–17].

In the mid 1980's, Lineberger and coworkers began investigating the photodissociation of dihalide ions embedded in mass-selected molecular clusters. Levinger and Alexander developed experimental methods to produce and detect $X_2^-(CO_2)_n$ clusters (X =I, Br) [18, 19]. Their mass selected photofragmentation experiments studied caging efficiency as a function of initial cluster size (n) and found that long range electrostatic forces present in these charged systems greatly enhance caging relative to neutral I_2 in solution.

Building on these results, Papanikolas et al. used a combination of experiments and modeling to elucidate the dynamics of the recombination process [20]. In their pump-probe experiments, a 720 nm pulse excites I_2^- to the A' electronic state, initiating photodissociation. A second 720 nm pulse monitors the progress of the reaction at various delay times. Immediately following the initial pulse, the absorption is bleached, the probe photon is not absorbed. At longer delay times, as I_2^- is caged by the solvent and recombines, its ability to absorb at 720 nm is restored. The absorption recovery profile, therefore, contains information about the timescales for electronic and vibrational relaxation. In addition to the overall recovery of the absorption signal, a transient feature at a time delay of 2 ps was observed for the larger clusters [21, 22]. Barbara and coworkers probed I_2^- photodissociation in liquid solution with direct absorption measurements and also found evidence of enhanced absorption within a few picoseconds of excitation and a similar overall timescale for recombination [23, 24]. These two sets

of experiments generated considerable interest in the photodissociation of molecular cluster ions and yielded several plausible explanations to account for the experimental observations. The most popular theory was that the transient absorption peak was evidence of coherent motion of I_2^- at the inner turning point of the A state; however, this was never conclusively demonstrated.

The first, and for several years the only, theoretical treatment of this problem was carried out by Amar and Perera. Their simulations of the photodissociation of $Br_2^-(CO_2)_n$ clusters were the first to include, in even a crude way, the dynamics on the excited electronic state [25]. Recognizing the importance of incorporating the ionic nature of the system into the dynamics, they modeled charge mobility by assigning a partial charge to each bromine atom and allowing these charges to vary as a function of the solute bondlength, such that as the molecule dissociates, the charge becomes localized on one atom. That is, Br_2^- dissociates to form Br^- and Br. The atom which receives the charge was chosen at random. In the presence of a solvent cluster, this leads to two scenarios: one in which the charge localizes on the solvated atom (Case A) and another in which the charge and solvent are separated (Case B). Although Case A is the result one would conventionally assume, they investigated both possibilities and found that the subsequent dynamics differed greatly in the two cases. For example, the second, counterintuitive, charge localization scheme produced caging from clusters with only one end of the solute 'capped' by a solvent molecule at an axial position, while caging with the normal charge localization scheme required capping at both ends of the solute. The dynamics clearly showed that in both cases, the kinetic energy of the dissociating bromine atoms was effectively quenched by collisions with solvent molecules at the cap sites. Additionally, in Case B, the uncapped, but charged, bromine atom was unable to escape the attractive electrostatic force of the solvent cluster, thus producing caging from half a solvent shell, consistent with the experimental results of Alexander et al. Amar and Perera gave no rationale for this anomalous charge localization, and some

researchers in the field initially dismissed it as an artifact of the simulation procedure; however, Maslen et al. subsequently demonstrated that it is correct [26]. Although the evolution of a more sophisticated treatment of the excited state dynamics required several years and contributions from multiple researchers, the localization of charge on the less solvated atom leading to electrostatic caging, first suggested by Amar and Perera, is now generally accepted as a fundamental characteristic of the photodissociation dynamics.

Until recently, subsequent simulations focused on characterizing the relaxation dynamics following recombination on the ground electronic state. The $I_2^-(CO_2)_n$ cluster dynamics developed by Papanikolas et al. improved on the treatment of the solute electronic structure implemented by Amar and Perera by incorporating the polarization of I_2^- by the solvent [27]. This was accomplished by extending the charge switching function to depend on the strength of the electric field produced by the solvent environment [26]. They found that the delocalization of charge that accompanies recombination forces the solvent to reorganize and therefore efficiently transfers energy from the solute bond into the cluster. This is in agreement with bulk liquid simulations by Hynes, Benjamin and coworkers which conclude that charge flow on the ground electronic state accelerates the rate of vibrational relaxation [28–30].

1.2 Recent Advances

Several additional systems have been studied by the Lineberger group including I_2^- in a variety of solvent clusters and at multiple wavelengths and ICl^- in CO_2 clusters. $I_2^-Ar_n$ clusters were the first of these systems to be explored jointly with experiments and theory on roughly equal footing. In late 1996, Batista and Coker [31], and Faeder et al. [3] independently used nonadiabatic surface hopping methods [32] to simulate the excited state photodissociation and recombination process explicitly. Batista and Coker employed a semiempirical Diatomics-in-Ionic-Systems Hamiltonian, while we

have developed a model Hamiltonian based on **ab initio** electronic structure calculations and the distributed multipole analysis of Stone and coworkers [33]. Both simulations reproduce the experimental product distributions reported by Vorsa et al., which revealed a bimodal distribution of recombined products [2]. Several possible explanations for this had been proposed, but both simulations found that recombination on the first excited state and the ground state of I_2^- was the cause. In addition, our simulations revealed the mechanism for I^- escape, which leads to a bimodal distribution of dissociative products, as mentioned earlier.

These theoretical results have since been verified by time resolved techniques. Femtosecond photoelectron spectroscopy (FPES) techniques developed by Neumark and coworkers provide a complement to the absorption recovery techniques of the Lineberger group by monitoring the cluster energetics through the photodissociation process and providing information about the changing solvation dynamics [34–37]. In these experiments, I_2^- is excited at 780 nm and after a variable delay time a second, high-energy pulse detaches the electron. By measuring the excess kinetic energy of the electron, one can determine the energy of the cluster which in turn is a function of the instantaneous cluster configuration. Comparison of experimental and simulated spectra verify anomalous charge flow on the dissociative excited states and recombination on the first excited state [38, 39]. Furthermore, overall timescales agree well throughout the dynamics (complete relaxation requires $>$200 ps). This is in agreement with earlier results of Lineberger and coworkers [40].

As for the photodissociation of $I_2^-(CO_2)_n$ clusters, the results presented here, considered along with the work of our experimental collaborators in the Lineberger [21, 22, 40–43] and Neumark [39] groups and in the Coker group [44], show we have a solid understanding of this system. The bulk of this thesis is devoted to exploring the dynamics of this system.

Hovering around the fuzzy line between what we do and don't understand are the

dynamics of $ICl^-(CO_2)_n$ clusters. Experiments by Nadal et al. hint at the complexity of solvent perturbation of the solute electronic states [45, 46]. The photofragmentation products, which include I^-, Cl^-, and ICl^- based clusters, show a complicated dependence on the initial cluster size, again emphasizing that the isolated solute potential curves are inadequate for deducing which dissociative asymptotes are accessible. Current research in the Parson and Lineberger groups is aimed at uncovering the mechanisms at work in this system [47, 48].

Finally, there are the experimental results about which theory has thus far had little to say. These include the two-photon photofragmentation experiments [22, 49] and two-color pump-probe experiments [41, 50] on solvated I_2^- clusters of Lineberger and coworkers and the solution phase experiments of the Barbara group which investigate the photodissociation dynamics of I_2^- in a range of solvent baths using multiple probe wavelengths [23, 24]. Each class of experiments provides a wealth of information about the photodissociation process, including details about the break up of the solvent cage (clusters), and lifetimes of the excited electronic states. To date, there has been insufficient knowledge of the spectroscopy of the excited solute-solvent system to extract this information, with confidence, from the experimental signals. This is an ideal opportunity for exploiting the advantages of molecular dynamics simulations and collaborations are underway to make progress on this front.

1.3 Thesis Overview

Chapter 2 gives an overview of the model developed by the Parson group that was used to calculate the results presented in this thesis, and describes methods to analyze the simulation trajectories. Chapter 3 describes the dynamics following 790 nm excitation of $I_2^-(CO_2)_n$. Chapter 4 provides evidence for fast spin-orbit relaxation in $I_2^-(CO_2)_n$ following UV excitation. Simulation of the absorption recovery is presented in Chapter 5. Chapter 6 compares the dynamics of $I_2^-(CO_2)_n$ and $I_2^-Ar_n$. Finally, Chap-

ter 7 describes work in progress developing a potential model for $I_2^-(OCS)_n$ clusters.

References for Chapter 1

[1] A version of this story is given in Appendix A.

[2] V. Vorsa, P. J. Campagnola, S. Nandi, M. Larsson, and W. C. Lineberger, J. Chem. Phys. **105**, 2298 (1996).

[3] J. Faeder, N. Delaney, P. Maslen, and R. Parson, Chem. Phys. Lett. **270**, 196 (1997).

[4] J. Franck and E. Rabinowitch, Trans. Faraday Soc. **30**, 120 (1934).

[5] J. Zimmerman and R. M. Noyes, J. Chem. Phys. **21**, 2086 (1950).

[6] F. W. Lampe and R. M. Noyes, J. Am. Chem. Soc. **76**, 2140 (1954).

[7] D. Booth and R. M. Noyes, J. Am. Chem. Soc. **82**, 1868 (1960).

[8] L. F. Meadows and R. M. Noyes, J. Am. Chem. Soc. **82**, 1872 (1960).

[9] T. Chuang, G. Hoffman, and K. Eisenthal, Chem. Phys. Lett. **25**, 201 (1974).

[10] D. J. Nesbitt and J. T. Hynes, J. Chem. Phys. **77**, 2130 (1982).

[11] Q. Liu, J.-K. Wang, and A. H. Zewail, Nature **364**, 427 (1993).

[12] J.-K. Wong, Q. Liu, and A. H. Zewail, J. Phys. Chem. **99**, 11309 (1995).

[13] R. Zadoyan, Z. Li, C. Martens, and V. Apkarian, J. Chem. Phys. **101**, 6648 (1994).

[14] C. Wan, M. Gupta, J. Baskin, Z. Kim, and A. Zewail, J. Chem. Phys. **106**, 4353 (1997).

[15] Y. Yan, R. Whitnell, K. Wilson, and A. Zewail, Chem. Phys. Lett. **193**, 402 (1992).

[16] C. Lienau and A. Zewail, Chem. Phys. Lett. **222**, 224 (1994).

[17] Q. Liu, J.-K. Wong, and A. H. Zewail, J. Phys. Chem. **99**, 11321 (1995).

[18] N. E. Levinger, Spectroscopy and Dynamics of Large Cluster Ions, PhD thesis, University of Colorado, 1990.

[19] M. L. Alexander, Photodissociation Studies of Mass-Selected Ionic Clusters, PhD thesis, University of Colorado, 1987.

[20] J. M. Papanikolas, I_2^- Photodissociation and Cage Recombination Dynamics in Size-Selected $I_2^-(CO_2)_n$ Clusters, PhD thesis, University of Colorado, 1994.

[21] J. Papanikolas, V. Vorsa, M. Nadal, P. Campagnola, J. Gord, and W. C. Lineberger, J. Chem. Phys. **97**, 7002 (1992).

[22] J. Papanikolas, V. Vorsa, M. Nadal, P. Campagnola, H. Buchenau, and W. C. Lineberger, J. Chem. Phys. **99**, 8733 (1993).

[23] D. A. V. Kliner, J. C. Alfano, and P. F. Barbara, J. Chem. Phys. **98**, 5375 (1993).

[24] P. K. Walhout, J. C. Alfano, K. A. M. Thakur, and P. F. Barbara, J. Phys. Chem. **99**, 7568 (1995).

[25] L. Perera and F. G. Amar, J. Chem. Phys. **90**, 7354 (1989).

[26] P. E. Maslen, J. M. Papanikolas, J. Faeder, R. Parson, and S. V. ONeil, J. Chem. Phys. **101**, 5731 (1994).

[27] J. M. Papanikolas, P. E. Maslen, and R. Parson, J. Chem. Phys. **102**, 2452 (1995).

[28] I. Benjamin and R. M. Whitnell, Chem. Phys. Lett. **204**, 45 (1993).

[29] B. J. Gertner, K. Ando, R. Bianco, and J. T. Hynes, Chem. Phys. **183**, 309 (1994).

[30] I. Benjamin, P. F. Barbara, B. J. Gertner, and J. T. Hynes, J. Phys. Chem. **99**, 7557 (1995).

[31] V. S. Batista and D. F. Coker, J. Chem. Phys. **106**, 7102 (1997).

[32] J. C. Tully, J. Chem. Phys. **93**, 1061 (1990).

[33] A. J. Stone, The Theory of Intermolecular Forces, Oxford, New York, 1996.

[34] R. Parson and J. Faeder, Science **276**, 1660 (1997).

[35] B. J. Greenblatt, M. T. Zanni, and D. M. Neumark, Chem. Phys. Lett. **258**, 523 (1996).

[36] B. J. Greenblatt, M. T. Zanni, and D. M. Neumark, Science **276**, 1675 (1997).

[37] B. J. Greenblatt, M. T. Zanni, and D. M. Neumark, Faraday Discuss. **108**, 101 (1997).

[38] J. Faeder and R. Parson, J. Chem. Phys. **108**, 3909 (1998).

[39] B. J. Greenblatt, M. T. Zanni, and D. M. Neumark, private communication.

[40] V. Vorsa, S. Nandi, P. J. Campagnola, M. Larsson, and W. C. Lineberger, J. Chem. Phys. **106**, 1402 (1997).

[41] A. Sanov, T. Sanford, S. Nandi, and W. C. Lineberger, J. Chem. Phys. **111**, 663 (1999).

[42] J. Papanikolas, J. Gord, N. Levinger, D. Ray, V. Vorsa, and W. C. Lineberger, J. Phys. Chem. **95**, 8028 (1991).

[43] D. Ray, N. Levinger, J. Papanikolas, and W. C. Lineberger, J. Chem. Phys. **91**, 6533 (1989).

[44] C. Margulis and D. F. Coker, J. Chem. Phys. **110**, 5677 (1999).

[45] M. Nadal, The Study of the Photodissociation and Recombination Dynamics of Mass-Selected Cluster Ions: Solvent Effects on the Structure and Dynamics of the Ionic Chromophore, PhD thesis, University of Colorado, 1996.

[46] M. E. Nadal, P. D. Kleiber, and W. C. Lineberger, J. Chem. Phys. **105**, 504 (1996).

[47] J. Faeder and R. Parson, in preparation.

[48] T. Sanford and W. C. Lineberger, private communication.

[49] A. Sanov, S. Nandi, and W. C. Lineberger, J. Chem. Phys. **108**, 5155 (1998).

[50] A. Sanov and W. C. Lineberger, private communication.

Chapter 2

Simulation and Analysis Methods

The work presented in this thesis focuses on applying the nonadiabatic molecular dynamics simulation methods developed in our group to the photodissociation of solvated I_2^- and on interpreting the results of these simulations. The model itself is the product of many years of toil by Jim Faeder, and his thesis and the publications borne of it are the best references for complete details [1–4]. In this chapter I summarize key features of the method and familiarize the reader with the tools we have developed to understand the dynamics.

In the dynamics of solvated I_2^-, the excess charge on the ion plays a critical role by providing strong coupling between the solute and solvent motion. As the iodine atoms move, the solvent reorganizes so as to solvate the charge. This solvent reorganization in turn polarizes the solute charge distribution. In the representation defined by the electronic states of the isolated solute, this polarization is associated with a strong mixing of the basis states. As we will see, the charge localizes either towards or away from the solvent, depending on the bonding character of the solute electronic state. When the solvent and charge are well separated, the electrostatic attraction produces a strong restoring force which can retard dissociation.

Another interesting aspect of the systems considered here is the similar size of the solute bond strength in the ground electronic state ($D_e = 1.01$ eV), the spin-orbit splitting energy ($\Delta_{so} = 0.94$ eV) and the potential created by the first solvation shell.

This last quantity depends on the solvent and the cluster configuration and in a solvent such as CO_2, roughly half of one solvation shell can generate a potential difference of 0.75–1.0 eV between the two iodine atoms.

These factors produce intriguing dynamics, but also pose a considerable challenge for simulations. We require both detailed information about the solute electronic structure and an interaction potential that depends on all of the nuclear degrees of freedom of the solute–solvent system. We achieve this goal using mixed quantum–classical methods. Throughout the course of a molecular dynamics simulation, the solute electronic structure is determined from an **ab initio** calculation, the nuclear degrees of freedom are treated classically and the interplay between the solute and solvent charge distributions enters through the interaction terms of the effective Hamiltonian described below. The Hamiltonian and its derivatives provide the energies, forces and nonadiabatic transition probabilities necessary to calculate cluster structures and perform molecular dynamics simulations of the complete photodissociation and recombination process.

2.1 Effective Hamiltonian for Solvated I_2^-

We assume at the outset that there is no charge transfer to the solvent, and electronic structure calculations indicate this is a valid approximation [5, 6]. In our model, the solvent is treated as a perturbation on the solute electronic states. The effects of this perturbation can be strong since the solute states become nearly degenerate. In its simplest form, the effective Hamiltonian is written as a sum of the Hamiltonians of the isolated molecules plus an interaction term:

$$\hat{H}_{eff} = \hat{h}_{solute} + \hat{H}_{solvent} + \hat{H}_{interaction}. \tag{2.1}$$

We assume the excited electronic states of the solvent are not energetically accessible, thus $\hat{H}_{solvent}$ is a constant and may be omitted. The six low-lying electronic states of

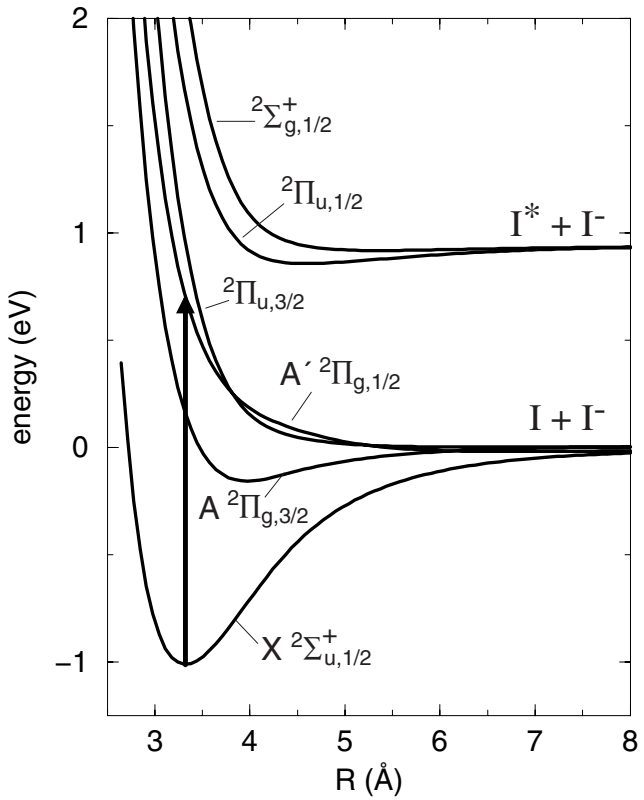

Figure 2.1: Scaled **ab initio** gas phase potential curves for I_2^-. The arrow shows the 790 nm photoexcitation to the $A'\,^2\Pi_{g,1/2}$ state.

I_2^-, obtained from an **ab initio** calculation of the isolated solute, are the eigenstates of $\hat{h}_{solute}$ and form the basis set in which the total Hamiltonian is evaluated. These states are illustrated in Fig. 2.1. The interaction Hamiltonian includes electrostatic, induction and short range interactions of the solute–solvent system which couple the electronic states of the solute.

Our treatment of the interaction between the solute and solvent charge distributions is based on the distributed multipole (DM) analysis method formulated by Stone [7, 8]. In this representation, a charge distribution is expanded as a sum of charge, dipole and quadrupole moments at multiple sites along the internuclear axis, and the electrostatic interaction between two molecular charge distributions (Q) takes

the form:

$$\hat{E}_{electrostatic} = \frac{1}{2}\sum_{t,u} Q_t^a T_{tu}^{ab} Q_u^b. \tag{2.2}$$

The indices a and b run over all the expansions sites and t and u are the components of the multipole moments (charge, x-dipole, y-dipole, z-dipole,...). All of the dependences on intermolecular distances and orientations are hidden in T_{tu}^{ab}, the interaction tensors, for which explicit formulae have been tabulated [9].

In an adaptation of the DM formalism, we treat the solute charge distribution quantum mechanically while the solvent charges are treated classically. The quantum mechanical analog of the charge density expansion is the distributed multipole **operator**, $\hat{q}$. The diagonal elements of this operator represent the charge distribution of each electronic state of the the solute. A central feature of our treatment is the incorporation of the off-diagonal elements, which represent transition charge densities; in the presence of the solvent they couple the different electronic states giving rise to polarization of the solute [8]. We end up with two types of terms:

$$\hat{H}_{electrostatic} = \frac{1}{2}\mathsf{Q}\cdot\mathsf{T}\cdot\mathsf{Q} + \hat{\mathsf{q}}\cdot\mathsf{T}\cdot\mathsf{Q}. \tag{2.3}$$

The first term is the interaction of the permanent moments of the solvent with other solvent molecules. In the second term, $\hat{q}$ is the charge density operator of the solute, and this term represents the full interaction of the solute with the permanent moments of the solvent, including polarizability of the solute.

The solute charge polarizes the charge clouds on the solvent; those induced multipoles interact both with the solute and each other. These effects are described by $\hat{H}_{induction}$. As shown in Ref. [2], the terms of this operator are similar to $\hat{H}_{electrostatic}$,

with the addition of α, the polarizability tensor of the solvent,

$$\begin{aligned}\hat{H}_{induction} &= -\frac{1}{2}\mathsf{Q}\cdot\mathsf{T}\cdot(\mathsf{T}+\alpha^{-1})^{-1}\cdot\mathsf{T}\cdot\mathsf{Q} \\ &\quad -\frac{1}{2}\hat{\mathsf{q}}\cdot\mathsf{T}\cdot(\mathsf{T}+\alpha^{-1})^{-1}\cdot\mathsf{T}\cdot\hat{\mathsf{q}} \\ &\quad -\hat{\mathsf{q}}\cdot\mathsf{T}\cdot(\mathsf{T}+\alpha^{-1})^{-1}\cdot\mathsf{T}\cdot\mathsf{Q}. \qquad (2.4)\end{aligned}$$

The first term describes the polarization of the solvent by the permanent moments of other solvent molecules. The second term describes the changes in the solvent charge distribution which are induced by the solute. The third term is a cross term describing polarization by both the solvent moments and the solute charge distribution.

The remaining short range interactions, repulsion and dispersion, are described by pairwise atom–atom potentials fit to reproduce empirical data. Since little is known about the interactions of I_2^- with the solvent molecules, the potentials are fit to the interactions of the solute fragments (I^- and I) and the solvent molecules. These potentials have been characterized by a combination of scattering data and photoelectron spectroscopy [10, 11]. Chapter 7 describes attempts at fitting model parameters for the I_2^-—OCS interaction, for which very little data is available.

2.2 Molecular Dynamics

Our nonadiabatic dynamics simulations are based on the classical path method [12, 13]. We assume the Born-Oppenheimer approximation of separability of nuclear and electronic degrees of freedom holds true, except in regions of strong coupling. The nuclear coordinates evolve classically under the influence of a single potential surface through a short timestep, δt, while the electronic coordinates are integrated quantum mechanically along this path. The timestep for the quantum integration is much smaller than the classical timestep and at each step an assessment is made as to whether the quantum degrees of freedom are in fact separable from the nuclear motion. If necessary,

the classical timestep is reduced, this occurs in regions where transitions are likely. A stochastic algorithm determines when nonadiabatic transitions will occur [14].

The effective Hamiltonian is evaluated in the basis set of the isolated solute at the current geometry. The Hamiltonian matrix is not diagonal due to coupling introduced by the solute-solvent interactions. Diagonalizing the Hamiltonian produces the adiabatic states, $\phi_i(r; R(t))$. These states are functions of all of the electronic coordinates, r, and depend parametrically on the nuclear coordinates, R(t). The total wavefunction of the system is a linear combination of these states:

$$\Psi(\mathbf{r}, \mathbf{R}, t) = \sum_i c_i(t)\phi_i(\mathbf{r}; \mathbf{R}(t)). \tag{2.5}$$

Plugging this into the time-dependent Schroedinger equations yields the following equation for the quantum amplitudes, $c_i(t)$,

$$\dot{c}_i(t) = -ic_i H_{ii} + c_i \dot{\mathbf{R}} \cdot \mathbf{d}_{ij}. \tag{2.6}$$

The change in amplitudes depends on the classical velocity and on the nonadiabatic coupling vector, $\mathbf{d}_{ij}$, the off-diagonal elements of the force matrix. The classical forces and the nonadiabatic couplings can be expressed in terms of derivatives of the Hamiltonian matrix elements, which in turn can be calculated analytically [3].

From the quantum amplitudes, we also compute the probability of making a nonadiabatic transition. This probability is compared to a random number using Tully's method of least switches to determine whether a hop is to be attempted. Each trajectory is in a single quantum state at any given time, and the distribution of states over an ensemble of many trajectories approximates the quantum probabilities given by $|c_i(t)|^2$.

To generate an ensemble of initial conditions, a cluster is first equilibrated using adiabatic dynamics on the ground state with an arbitrary initial structure and fixed total energy. A single long-time trajectory is then sampled to give the initial conditions. The solute is then promoted to an excited electronic state and the trajectories are launched

on the new potential surface. As the dynamics proceeds, the states become coupled and nonadiabatic transitions occur. Trajectories continue until some criterion, for example, a maximum bondlength, is met. The remainder of this chapter deals with interpreting the dynamics.

2.3 Analysis Tools

The benefit of running simulations is the ability to learn, directly, detailed microscopic information about the system. The challenge is to figure out what information is most useful for understanding the dynamics. The photodissociation process takes place on multiple, multidimensional potential energy surfaces. Even with only a few solvent molecules, we cannot possibly visualize all of the degrees of freedom, and even if we could, it's not clear that this picture would provide much enlightenment. Since we expect the most important features of these systems to depend on the overall solvent environment rather than the detailed molecular motions, we define a collective solvent coordinate that depends on the nuclear coordinates of all solvent molecules but condenses that information into a single quantity describing the relative solvation of the two iodine atoms. To understand the forces driving the dynamics requires knowledge of this solvent coordinate, the electronic state and the bondlength of the solute, and the distribution of the excess charge.

A quick way to get acquainted with the dynamics is to watch animations of individual trajectories. It's hard to find a substitute for the intuition that is gained from directly viewing the simulations this way. In addition to watching the nuclear configurations change, it is straightforward to monitor properties such as the electronic state populations and the solute charge distribution. Unfortunately, this process is extremely time-consuming for a large number of trajectories and does not transfer well to print media. More importantly, it is not an effective means for studying the behavior of an entire ensemble because it is too easy to be distracted by the frequently irrelevant partic-

ulars of individual trajectories. Nevertheless, when unanticipated results are observed it is often necessary to resort to this tool and some of our most significant results were initially discovered in this way. (In the long run, it would be worthwhile to create a user interface to display multiple aspects of a trajectory onscreen simultaneously, now that we know what data to look at.)

When the results of a new calculation are in, the first step is to analyze the ensemble as a whole with methods that have proven useful in previous studies. At the early stages of this project, that essentially meant comparing final product distributions to experimental values and watching individual trajectories. Since any system of interest differs from what's been done before, the next task is to identify aspects of the dynamics which are surprising or unusual and then to design new tools that characterize them well enough to allow one to quickly identify additional instances in the entire ensemble.

2.3.1 Potential Energy versus Time

The eigenvalues of the Hamiltonian matrix, which are automatically generated during the course of the simulations, are the instantaneous energies of the electronic states. A plot of the energies of all of these states (not just the one that is occupied) along a simulation trajectory can be used to reveal several aspects of the dynamics. Figure 2.2 shows such a plot for I_2^- embedded in a CO_2 cluster. For simplicity, we will not worry about which electronic state is occupied. Initially, the energetic ordering of the states is the same as in isolated I_2^-, namely, X, A, A', a, a' and B, from the lowest to the highest energy. The first few hundred femtoseconds of a trajectory are dominated by the impulsive dissociation of I_2^- as it races down a repulsive electronic state and the potential energy traces resemble a compressed version of the solute potential curves shown in Fig. 2.1. Commonly, we see evidence of kinematic caging as I_2^- recoils from the solvent cluster. In the trajectory shown, the sharp spike occuring simultaneously in

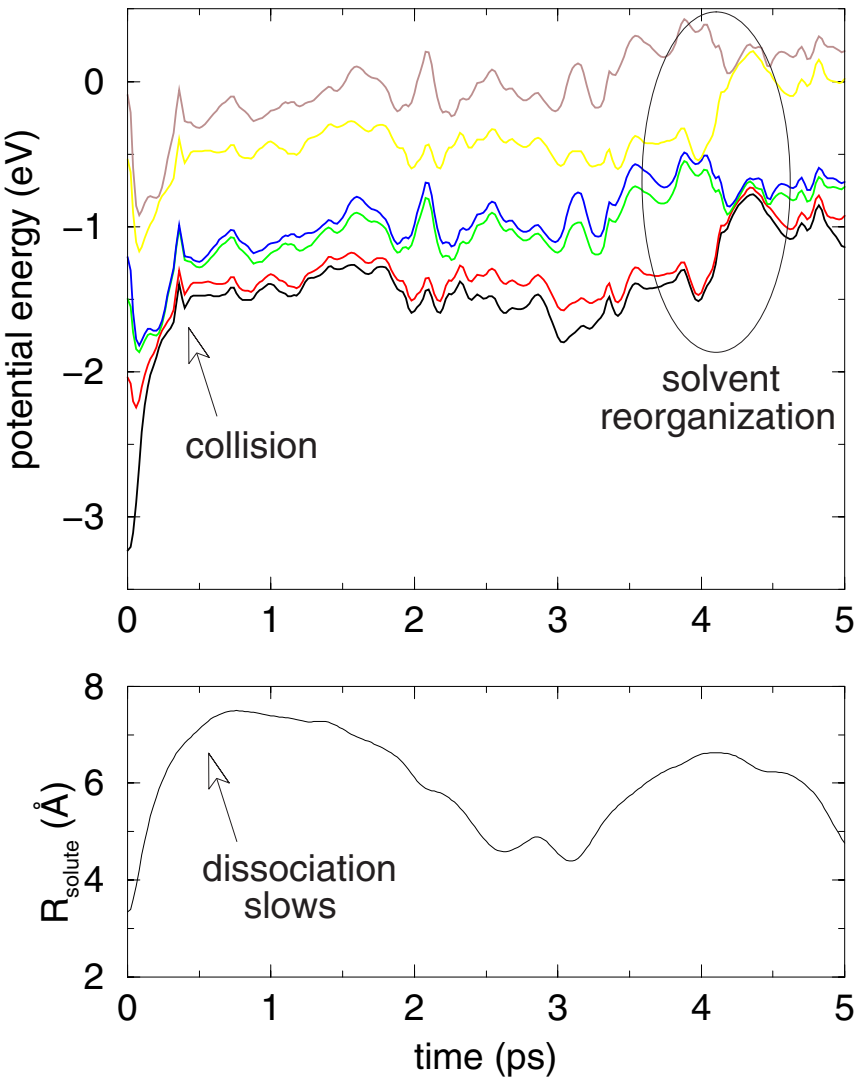

Figure 2.2: The top panel shows the potential energy versus time for the 6 electronic states of I_2^- included in our simulations. The bottom panel shows the solute bondlength versus time for the same trajectory.

all of the electronic states, just before 0.5 ps, is due to a strong collision with the solvent cage. The solute bondlength for this trajectory, plotted in the lower panel of Figure 2.2, corroborates this interpretation, as does an animation of the dynamics (not shown).

For the next several picoseconds of this trajectory, the solute bondlength varies, but generally remains large enough that the contributions to the energy from the solute potential are roughly constant. The small-scale fluctuations of the energy depend on

microscopic details of the positions of each atom in the cluster, and are not of much interest. The intriguing behavior is the changing pattern of nearly degenerate states [15]. Between 0.5 and 1.5 ps, there are essentially four energy levels, the lower two being doubly degenerate. Note that the spacing between the two upper states mimics the spacing between the two lower states, while a larger gap tends to separate the second and third levels. This classification is approximate and subjective, but is substantiated by considering the behavior of a large number of trajectories. From 1.5 to 3.5 ps the potential energy details are complicated by changes in the solute bondlength, but the underlying pattern is maintained. At about 4 ps something very interesting happens. A pattern of 3 distinct levels forms, but quickly gives way to a new pattern with two levels. This latter combination of states corresponds to the two lowest dissociative limits of I_2^-, separated by the spin-orbit splitting of iodine (0.94 eV). These dramatic changes in the spacings between electronic states are accompanied by significant changes in the solvent environment. In time, we will come to see how the optimal solvent configuration depends on the occupied electronic state and thus understand the driving forces behind these large scale reorganization events. While these plots provide initial insights into the dynamics, they are limited in their usefulness because the potential energy of the system depends on so many variables, and we need to develop another method for analyzing the dynamics.

2.3.2 The Solvent Coordinate

To visualize how the cluster configuration is changing in time, without getting bogged down in the details of each molecular motion, we introduce a collective solvent coordinate inspired by the theory of electron transfer in liquids [16–18]. The solvent coordinate, $\Delta\Phi$, is defined as the change in energy when a charge of $-e$ is moved from one iodine atom to the other, holding all nuclear coordinates fixed. When the magnitude of $\Delta\Phi$ is small, as in Fig. 2.3(a), the two iodine atoms are exposed to similar solvent

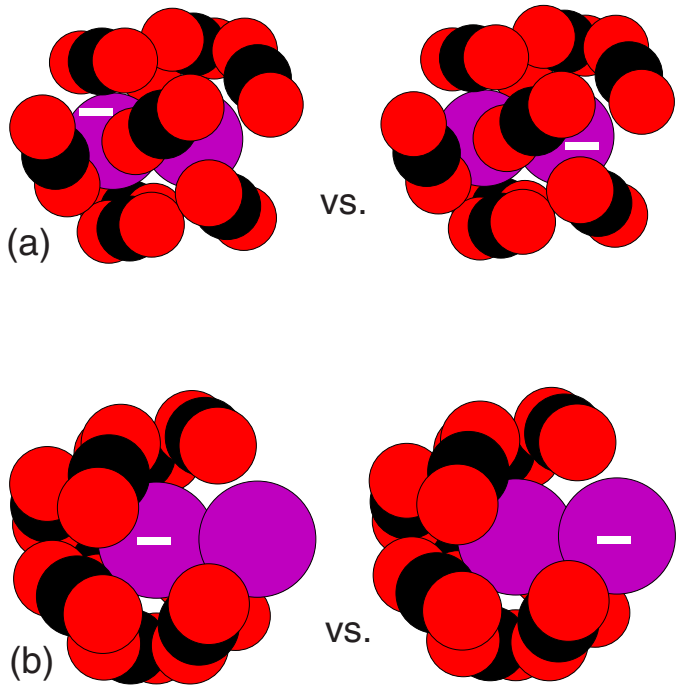

Figure 2.3: The solvent coordinate. (a) Solvent evenly distributed between iodine atoms, small $\Delta\Phi$. (b) Anisotropic solvent distribution, large $\Delta\Phi$.

environments, and when the magnitude of $\Delta\Phi$ is large, as in Fig. 2.3(b), the two iodine atoms are exposed to very different solvent environments. We refer to these two cases as symmetric and asymmetric solvation, respectively.

While $\Delta\Phi$ depends on the cluster geometry, it is a measure of the energy of that configuration, not a direct specification of the nuclear coordinates. Many different cluster configurations can have the same solvent coordinate. Also, in strongly interacting solvent clusters, such as CO_2, very small changes in the nuclear configuration can lead to large changes in the solvent coordinate, as we will see in Chapters 3 and 4.

The asymmetry of the solvent cluster, as measured by this coordinate, is a principal factor in determining the relative energy spacings between the solute electronic states and the location of strong nonadiabatic coupling regions. This is implicit in the plot of the potential energy shown above, but we will develop better tools for examining the role of the solvent coordinate below.

2.3.3 Solute Charge Flow

To study the flow of the excess solute charge, in relation to the overall solvent environment, we compare the solvent asymmetry coordinate, $\Delta\Phi$, defined above, with an analogous coordinate that specifies the location of the charge. The quantity Δq is the charge differential between the two iodine atoms,

$$\Delta q = |q_1| - |q_2|. \tag{2.7}$$

When Δq is positive, atom 1 has the bulk of the charge; when Δq is negative, atom 2 has the bulk of the charge and when Δq is zero the charge is completely delocalized. Likewise, the quantity, $\Delta\Phi$ is the difference in the solvent potential at the two iodine atoms. When $\Delta\Phi$ is positive, atom 1 is more heavily solvated, and so forth. We then consider the product, $\Delta q\Delta\Phi$, which is positive when the charge and solvent cluster are localized on the same iodine nucleus. This situation, which we are accustomed to assuming, is referred to as normal charge localization (or flow). If the product of Δq and $\Delta\Phi$ is negative, the charge has localized on the **less**-solvated iodine nucleus. In this case, which we call anomalous charge flow, it is important to note that the solvent continues to seek out the charge; it is the motion of the quantum mechanical electron which seems counterintuitive. As discussed in the next chapter, anomalous charge flow is a general characteristic of antibonding electronic states.

The fact that these two kinds of charge localization can occur is an important clue for unraveling the relationship between the solvent coordinate and the potential energy of the system, as depicted in Fig. 2.2. By constructing this measure of the charge flow, we have encapsulated an enormous amount of information about the kinds of dynamics we can expect on a particular electronic state. In the final section of this chapter, we describe a way to visualize the dynamics of many trajectories at once. Then we will be prepared to examine the actual simulations.

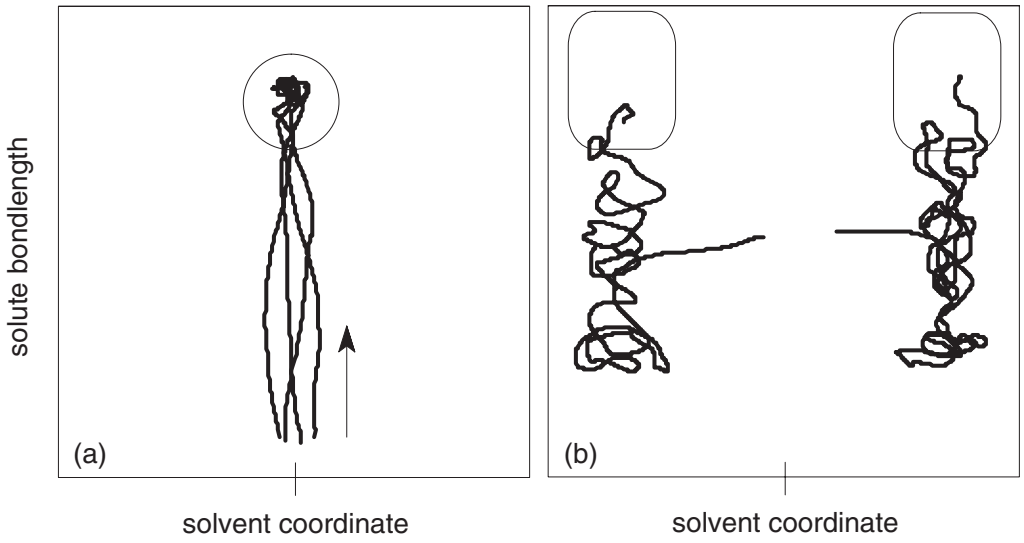

Figure 2.4: Two-dimensional map of trajectories on two different types of electronic states. (a) Initially, trajectories are straight or smooth and move collectively towards large solute bondlengths, reflecting the repulsive nature of this electronic state. (b) Trajectories on a potential surface similar to the one shown in Fig. 2.5(b). The nonadiabatic coupling regions are circled and the motion of trajectories in these regions is discussed in the text.

2.3.4 Two-dimensional Maps

We have found that the primary effect of the solvent is to produce an asymmetric environment around the solute. The Marcus solvent coordinate, $\Delta\Phi$, originally developed for the theory of electron transfer in solution, provides a convenient, overall measure of this asymmetry. One may envision the dynamics as being dominated by a two-dimensional effective Hamiltonian parametrized by the solute bondlength, R, and the solvent coordinate, $\Delta\Phi$ [19–21]. In so far as this is valid, the trajectories move on the two-dimensional potential surface associated with this Hamiltonian. In our analysis, we do not actually construct these surfaces; instead we plot the trajectories using these two coordinates and infer the shapes of the potential surfaces from the patterns that emerge. We emphasize that the dynamics is always computed from simulations that include all of the degrees of freedom present and the two-dimensional representation is used only as an analysis tool.

Plots of this variety proliferate throughout the remaining chapters and the following is a guide for inferring the shape of the potential energy surfaces from the trajectories. To indicate the electronic state of the solute, we typically use multiple linestyles or plot the population of each state on a separate graph. The potential energy curves of isolated I_2^- shown in Fig. 2.1 are a guide to the forces acting along the solute bond. These curves are most useful at short bondlengths (2–4Å), where the potential energy of the entire system depends more strongly on R than on $\Delta\Phi$. For example, Fig. 2.4(a) shows a number of trajectories starting on a repulsive electronic state at a short bondlength with a distribution of solvent coordinates near zero. Early on, the bondlength increases (repulsive state) with very little influence from the solvent. At some point, dissociation is stopped by the solvent. The trajectories then collect in a basin on the potential surface, taking on a snarled appearance. In the absence of surface hopping they would be trapped here. Introducing nonadiabatic coupling is like perforating the basin; clusters can now drop down to lower electronic states. The key point, however, is that smooth or straight sections in the trajectories reveal regions of the potential surface that are steeply sloped.

Figure 2.5(a) illustrates a case where the forces within the solute are weak, so that the bondlength is largely irrelevant and the solvent coordinate directs the dynamics. Trajectories enter this region at a variety of bondlengths with near-zero solvent coordinates and rapidly move to large solvent coordinates. The ridge in the potential energy surface that would produce this behavior is shown qualitatively. Figure 2.5(b) shows trajectories sliding down from a ridge and then becoming tangled, filling out a U-shaped region. This diffusive motion indicates the trajectories have reached a nearly flat region of the potential energy surface. In regions such as this, the dynamics reflect the competition between solvation forces which act to localize the excess charge and chemical bonding forces which act to delocalize the excess charge. With a map of an ensemble of trajectories, one can assess which force is stronger. If trajectories readily

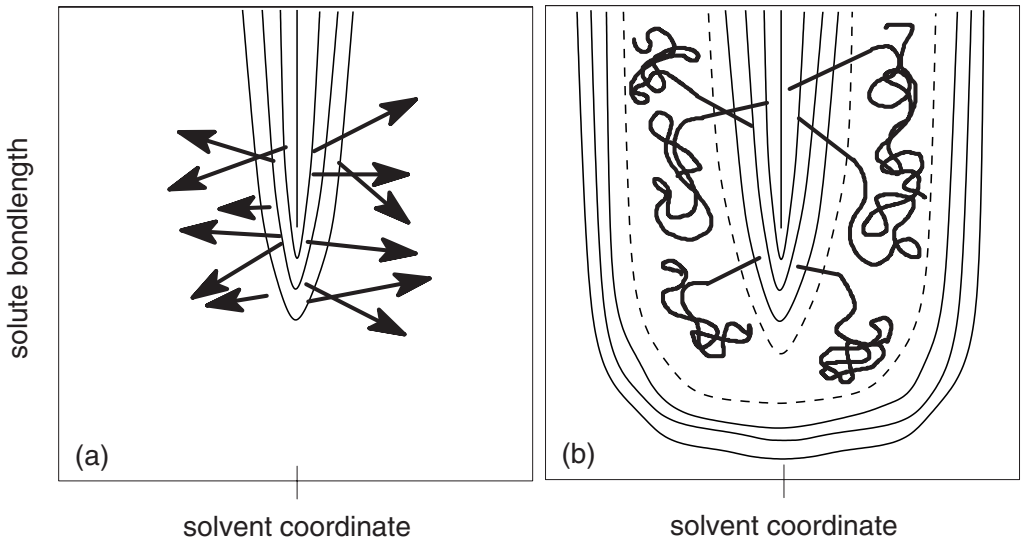

Figure 2.5: Two-dimensional map of trajectories exploring an electronic state. Heavy lines show the course of the dynamics, thin lines are attractive (dashed) and repulsive (solid) contours of the potential surface. (a) Trajectories racing down from the top of a steep ridge. (b) As the trajectories continue, more is revealed about the potential surface. Here the ridge leads to a trough.

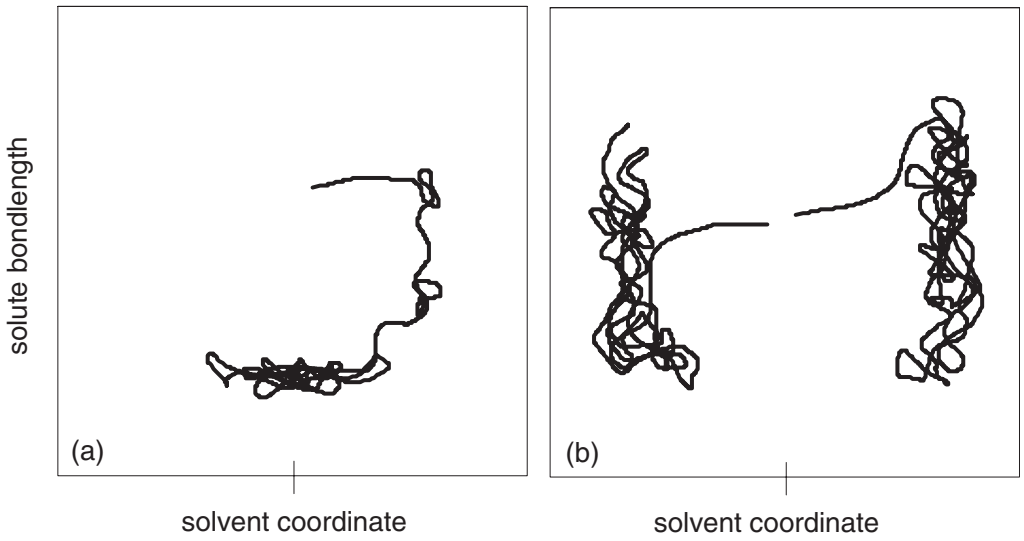

Figure 2.6: Two-dimensional map of trajectories illustrating the competition between the solute bond and solvation forces. The underlying potential surface is similar to the one shown in Fig. 2.5(b). (a) Trajectory fluctuates around zero solvent coordinate at a short bondlength, indicating a stable bond. (b) Trajectories do not cross through zero solvent coordinate, indicating that the solvent forces prevent the solute bond from forming.

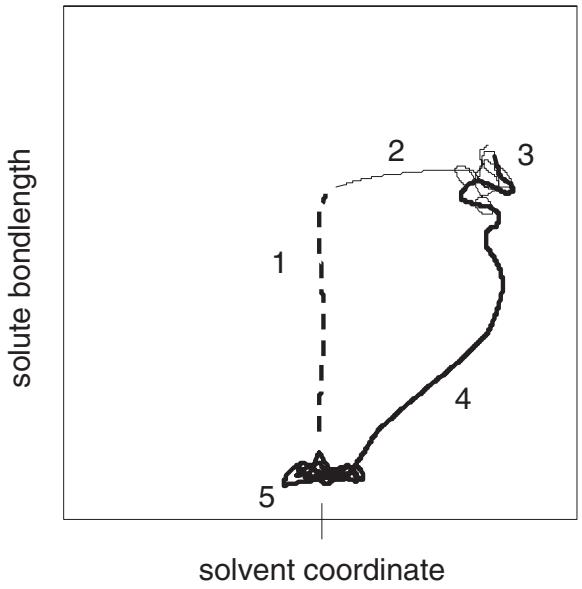

Figure 2.7: Two-dimensional map of a trajectory showing the complete dissociation and recombination process on three different electronic states, indicated by different linestyles. The trajectory proceeds from 1 to 5. The potential surfaces which we infer from these dynamics are described in the text.

cross $\Delta\Phi = 0$, as in Fig. 2.6(a), it indicates that the I_2^- bond has reformed. In contrast, a double welled map as in Fig. 2.6(b), indicates that strong solvation forces prevent recombination of the solute.

The nature of nonadiabatic coupling regions can also be inferred from these maps. Two distinct types of transition regions are shown in Fig. 2.4. In the first case, Fig. 2.4(a), the potential surface near the coupling region of the initial state is bowl-shaped and trajectories are essentially trapped here until a nonadiabatic transition occurs. In the second case, Fig. 2.4(b), the potential surface of the initial state is nearly flat. Here there are no forces restricting the trajectories to the coupling region. Commonly, repeated attempts are necessary before a hop is successful and so transitions from this second type of coupling region may be much less frequent since trajectories may wander away before a transition occurs.

Figure 2.7 shows a complete trajectory illustrating key points regarding these

plots. Sections of the trajectory are labelled 1–5 and linestyles indicate different electronic states. I. When the potential surface is steep, trajectories are straight or very smooth (1,2,4). II. Tangled trajectories indicate troughs or wells on the surface (3,5). III. Dramatic changes in the solvent coordinate coincide with transitions between states of different charge switching character (2) and when travelling on a single state between regions of strong solvation and strong bonding (4).

Once accustomed to reading data from these plots, it is easy to design a wide variety of diagnostic tools which exploit the dense concentration of information that can be presented this way. In one such application, we plot a point in the (R, $\Delta\Phi$) plane to represent the nuclear configuration of each cluster in the ensemble and then animate these points to follow the trajectory of each cluster throughout the photodissociation process. This allows us to identify times and places where substantial fractions of the ensemble arrive in unison. Locating these pile-ups in the population distribution is a preliminary step to understanding the spectroscopy of the excited clusters. Another map can be constructed by highlighting regions where the energy gap between a pair of states matches a chosen value. If we overlay the map and the animation, we can see how the population passes through an absorption window. This is just a few short steps away from actually simulating the absorption recovery signal.

Throughout the remaining chapters, additional analysis methods built from the basic elements described here are used to explore the dynamics simulations. Most notably, Chapter 3 introduces a view of the dynamics based on the Marcus theory of electron transfer and this is developed in greater detail in Chapter 4. The methods for simulating the absorption recovery signal are found in Chapter 5.

References for Chapter 2

[1] J. Faeder, The X_2^- Files: Modeling Structure and Dynamics of Solvated Molecular Ions, PhD thesis, University of Colorado, 1998.

[2] P. E. Maslen, J. Faeder, and R. Parson, Mol. Phys. **94**, 693 (1998).

[3] J. Faeder, N. Delaney, P. Maslen, and R. Parson, Chem. Phys. **239**, 525 (1998).

[4] P. E. Maslen, J. Faeder, and R. Parson, Chem. Phys. Lett. **263**, 63 (1996).

[5] A. Sanov and W. C. Lineberger, private communication.

[6] A. Sanov, J. Faeder, R. Parson, and W. C. Lineberger, Spin-orbit coupling in ICO_2 and IOCS van der waals complexes: Beyond the pseudo-diatomic approximation, 1999, in press.

[7] A. J. Stone, Chem. Phys. Lett. **83**, 233 (1981).

[8] A. J. Stone, The Theory of Intermolecular Forces, Oxford, New York, 1996.

[9] S. L. Price, A. J. Stone, and M. Alderton, Mol. Phys. **52**, 987 (1984).

[10] Y. Zhao, C. C. Arnold, and D. M. Neumark, J. Chem. Soc. Faraday Trans. **89**, 1449 (1993).

[11] Y. Zhao, I. Yourshaw, G. Reiser, C. C. Arnold, and D. M. Neumark, J. Chem. Phys. **101**, 6538 (1994).

[12] J. C. Tully, Nonadiabatic processes in molecular collisions, in Dynamics of Molecular Collisions, edited by W. H. Miller, volume Part B, Plenum, New York, 1976.

[13] S. Hammes-Schiffer, J. Phys. Chem. A **102**, 10444 (1998).

[14] J. C. Tully, J. Chem. Phys. **93**, 1061 (1990).

[15] C. Margulis and D. F. Coker, J. Chem. Phys. **110**, 5677 (1999).

[16] R. A. Marcus, Ann. Rev. Phys. Chem. **15**, 155 (1964).

[17] M. D. Newton and N. Sutin, Ann. Rev. Phys. Chem. **35**, 437 (1984).

[18] G. C. Schatz and M. A. Ratner, Quantum Mechanics in Chemistry, chapter 10, Prentice Hall, Englewood Cliffs, 1993.

[19] R. Bianco and J. T. Hynes, J. Chem. Phys. **102**, 7885 (1995).

[20] I. Benjamin, P. F. Barbara, B. J. Gertner, and J. T. Hynes, J. Phys. Chem. **99**, 7557 (1995).

[21] P. K. Walhout, J. C. Alfano, K. A. M. Thakur, and P. F. Barbara, J. Phys. Chem. **99**, 7568 (1995).

Chapter 3

Near-IR Photodissociation Dynamics of $I_2^-(CO_2)_n$

Although photodissociation and recombination of I_2^- have been extensively studied in clusters [1–6] and solution [7–11], only recently have simulations appeared that follow the entire course of this simple chemical reaction [12, 13]. The challenge of modeling these systems is twofold: first, as the anion dissociates the flow of excess charge couples strongly to the motion of the solvent molecules; second, this charge flow is highly nonclassical, depending sensitively upon the nature of the solute electronic wavefunction.

The interplay between the solute and solvent motion is an essential piece of infomation for interpreting the photodissociation dynamics of solvated ions. For example, recent studies of the phodissociation of I_2^- embedded in a cluster of argon atoms reveal that the mechanism for direct dissociation involves the ejection of the I^- ion from the solvent cluster [12, 14, 15]. The basis for this surprising result is the phenomenon called anomalous charge flow [6, 12, 16], and it can be understood in terms of a simple diatomic LCAO-MO picture. In the isolated molecule, the atomic orbitals combine into bonding and antibonding molecular orbitals, both of which are delocalized. Introducing an asymmetric solvent environment polarizes the solute charge distribution. The bonding molecular orbital polarizes so that most of the wave function amplitude localizes on the more solvated atom. Since the two molecular orbitals must remain orthogonal, the antibonding state must polarize in the opposite direction. This flow of

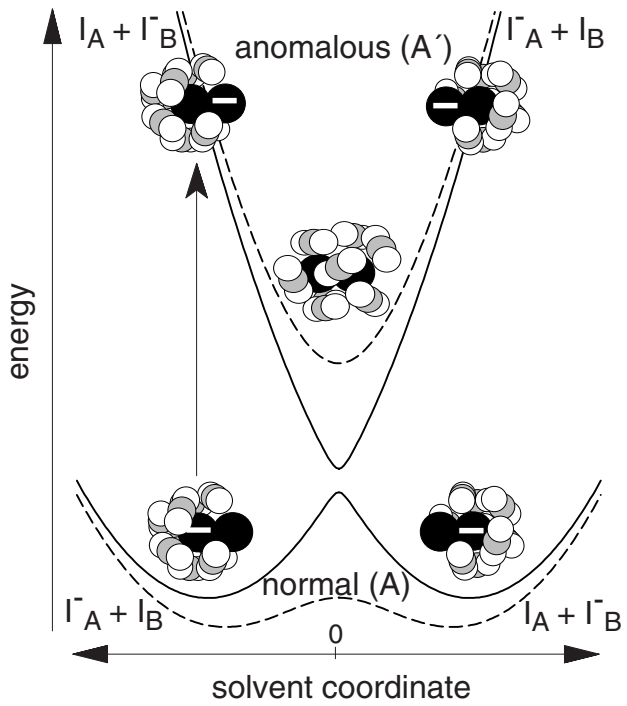

Figure 3.1: Schematic potential energy surfaces of solvated I_2^-. Dashed lines represent a cross-section at small I–I separations, where the bond coupling is strong compared to the solute-solvent interactions. The solid curves represent the weak coupling limit, which arises at longer bondlengths ($R_{\mathrm{solute}} > 5$ Å). Anomalous charge switching in the upper curves is illustrated by the cluster snapshots.

charge away from the solvent in the excited state is accompanied by a destabilization of the energy. In general, electronic states with negative polarizability are expected to display anomalous charge flow.

A complementary description of anomalous charge flow can be extracted from the theory of electron transfer in solutions [17–19] and provides a convenient framework for discussing the photodissociation dynamics in terms of a reduced number of coordinates, as described in Chapter 2. Figure 3.1 illustrates the state-dependence of charge flow for a two-state model of solvated I_2^-. The diabatic potential curves are two intersecting parabolas whose minima represent solvated iodide and neutral iodine. When the solute bondlength is near its equilibrium value, the electronic coupling is strong and the adiabatic curves are well separated energetically, as represented by the

dashed curves. As the solvent moves along the lower adiabatic curve, the charge follows the solvent from one side of the solute to the other. However, the charge moves in just the opposite way on the upper adiabatic state. A vertical excitation, as shown in the figure, changes the solute electronic state, moving the charge from I_A to I_B; however, the solvent still surrounds I_A. The solvent moves towards the charge in an effort to re-establish equilibrium. But, as the solvent coordinate crosses zero, and the solvent favors I_B, the electronic state changes character and the charge returns to I_A. The solvent must change direction once again to pursue the charge. This oscillation will persist as long as the solute remains in the excited state. The normal and anomalous charge flow states in this simplified model are reasonable analogs for the A and A' states of solvated I_2^-, respectively. The solid lines in Fig. 3.1 represent a longer solute bondlength, where the electronic coupling is weaker and transitions between states can occur when the solvent coordinate is near zero.

In the experiments we model, I_2^- is excited to the anomalous A' potential surface by a 790 nm laser pulse, as shown in Fig. 3.2. As the solute dissociates, it can undergo nonadiabatic electronic transitions to normal charge switching A and X states, where the dynamics of the charge-solvent interaction will change dramatically. We have recently developed a model Hamiltonian to compute the multiple, highly coupled potential energy surfaces that arise in these ionic systems [12]. This chapter presents our nonadiabatic molecular dynamics simulations of photodissociation and recombination in I_2^- clustered with 4-16 CO_2 molecules, an extension of our recent work on $I_2^-Ar_n$ clusters [12]. We observe for the first time the complete excited state dynamics, and identify the pathways for electronic relaxation and subsequent product formation. The CO_2 clusters behave quite differently from the previously studied argon clusters [12] because of the much stronger solute-solvent interactions.

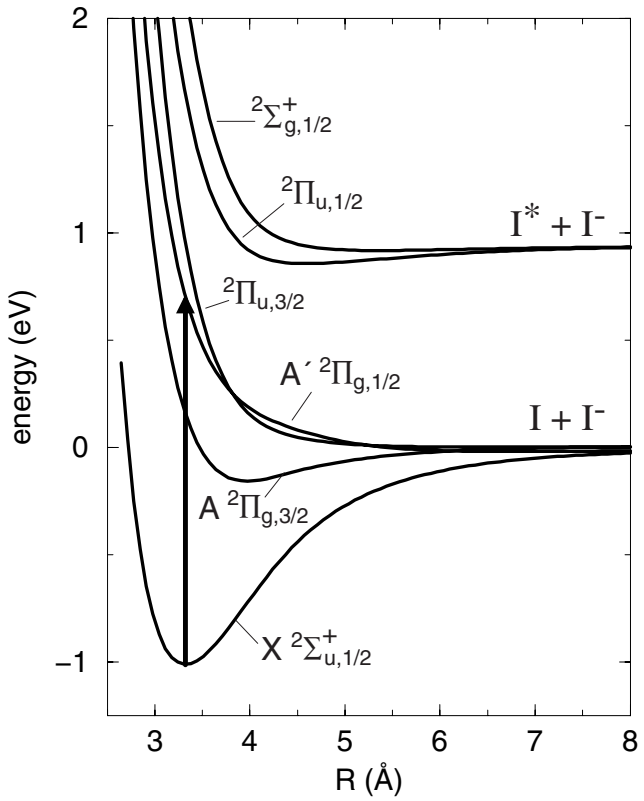

Figure 3.2: Scaled **ab initio** gas phase potential curves for I_2^-. The arrow shows the 790 nm photoexcitation to the $A'\,^2\Pi_{g,1/2}$ state modeled in the current simulations.

3.1 Methods

We determine the interaction potential between the solute I_2^- and the solvent CO_2 molecules using the model Hamiltonian described in Chapter 2. This model includes state-dependent electrostatic and induction interactions between the solute and solvent based on **ab initio** calculations of the solute wavefunctions [20] and experimental data for the solvent charge distribution [21] and polarizability [22]. State independent atom-atom Lennard-Jones potentials account for the remaining dispersion and repulsion interactions and are fit to reproduce the known I^-—CO_2 and I—CO_2 potential curves [23]. The CO_2—CO_2 interaction potential is taken from Murthy et al. [21]. The model captures the sensitive dependence of the solute charge distribution on the solute electronic state, the solute bondlength, and the positions and orientations of the solvent

molecules.

The methods for determining cluster structures, preparing initial ensembles, and computing the nonadiabatic dynamics following photodissociation have also been described previously [12]. Nuclear motion on a single potential surface is computed using the velocity version of the Verlet algorithm [24], while hopping between electronic states of the solute is computed using Tully's method [25, 26] with some minor modifications [12].

Two different ensembles, designed to emphasize different aspects of the dynamics, have been used in the simulations described here. The first type of ensemble includes 41 trajectories for each cluster size, integrated for up to 200 ps. The initial conditions were obtained by sampling a single 400 ps trajectory with an average temperature of 80 K. This temperature was chosen to lie on the upper end of the solid-liquid phase transition region in the clusters, based on our previous experience that such temperatures gave reasonable agreement with experimental results [12]. The products are determined by integrating the trajectories until the nuclear configurations meet either of two criteria: the I–I distance exceeds 20 Å, or I_2^- undergoes more than 100 oscillations in a particular potential well. The dissociation and recombination times vary from a few picoseconds to over 100 ps in some cases where I_2^- is trapped in an excited electronic state before recombining. The time scale for evaporation of CO_2 molecules from the clusters following photodissociation appears to be much longer than the 50–100 ps over which the trajectories are integrated, and thus we do not calculate the final product mass distributions, which are measured experimentally at 5–10 μs [2, 4]. The second type of ensemble consists of 200 trajectories, each of which is integrated for 10 ps. This ensemble was used to explore the short-time dynamics of electronic relaxation in clusters containing 9, 12, and 16 CO_2 molecules.

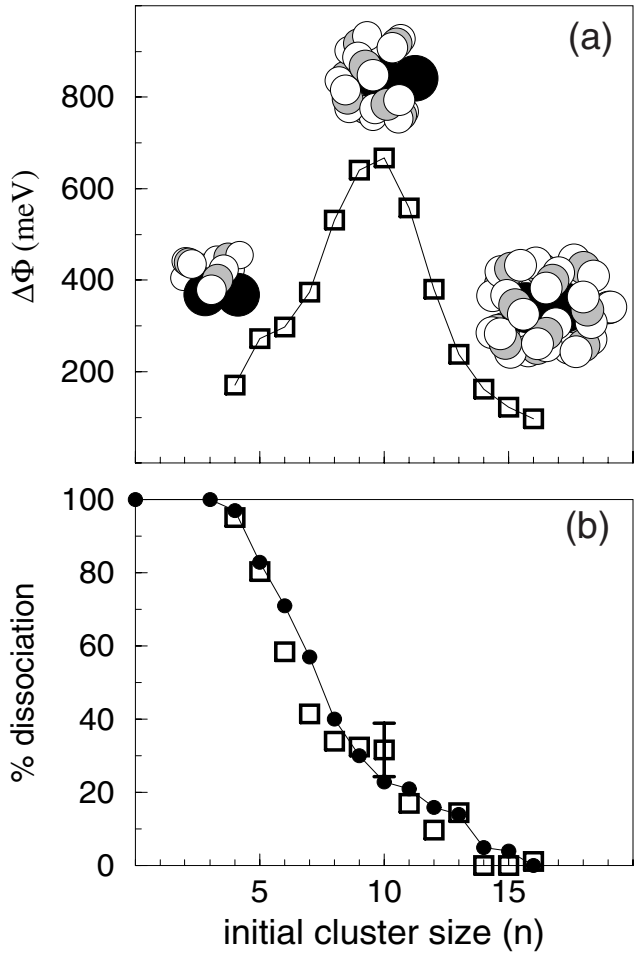

Figure 3.3: (a) Ensemble average of the magnitude of the solvent coordinate as a function of cluster size. Typical structures for $n = 5, 10, 16$ are shown. (b) Branching ratio for the products of $I_2^-(CO_2)_n$ photodissociation at 790 nm. The filled circles are the experimental data and the squares show the simulation results. The 1σ error bar shown for $n = 10$ is based on the statistical sampling and is representative of the error bars at other cluster sizes.

3.2 Results

3.2.1 Structures and Products

Figure 3.3(a) shows three cluster structures obtained from 80 K ensembles. The average binding energy per CO_2 at 80 K is fairly constant at about 200 meV for $10 \leq n \leq 18$, while for smaller cluster sizes it dips to about 190 meV. These values are consistent with the upper bound of 250 meV estimated from experiment that includes

the kinetic energy released upon evaporation [2]. The clusters develop a pronounced asymmetry in the range $7 \leq n \leq 13$, which is illustrated by the middle structure at $n = 10$. More symmetric solvent configurations are shown at $n = 5$, where the solvent tends to clump about the waist of I_2^-, and $n = 16$, the size at which the first solvation shell is thought to close in the experiment [2]. The structures and energetics we observe in our 80 K ensembles are in good agreement with earlier studies using optimized geometries [6, 27, 28].

To quantify the degree of solvent asymmetry, we define a solvent coordinate, $\Delta\Phi$, as the change in energy when a charge of $-e$ is moved from I_A to I_B for a fixed nuclear configuration. The average magnitude of $\Delta\Phi$ in the 80 K ensembles peaks at $n = 10$ and is a factor of 5 smaller for $n = 16$, as shown in Fig. 3.3(a). Large values of $\Delta\Phi$ exert a strong force to localize the charge on the favored atom, so that in the most asymmetric configurations, 60% of the excess charge in ground state I_2^- resides on the favored end of the molecule. Large initial solvent asymmetries also strongly influence the dynamics following photodissociation, as we discuss below.

Figure 3.3(b) compares the product branching ratios calculated from the model with the experimental results of Vorsa et al. [4, 29]. The 1σ error bar shown results from sampling a relatively small number of trajectories— 41 for each cluster size. The discrepancies between simulation and experiment are within the uncertainties for all but a few cluster sizes, and thus the model accurately reproduces the rapid onset of caging with increasing cluster size observed in the experiments [2, 4]. Also in agreement with experiment are the results that all of the dissociated products arise from ejection of neutral I atoms leaving behind solvated I^-, while all of the recombined products are based on I_2^- in its ground electronic state. In contrast, for argon clusters, experiment [4] and simulation [12, 13] find additional product channels corresponding to ejection of I^- ions and to recombination of I_2^- in the A state.

3.2.2 Dynamics

In Fig. 3.4 we plot the trajectories for $n = 9$ and 16 in two dimensions: the solute bondlength and $\Delta\Phi$. The three panels shown for each cluster size partition the trajectories based on electronic state. All trajectories begin in the A' state, shown in the top panel, at $R_{\rm solute} = 3.3$ Å. Upon reaching the coupling regions marked with ovals, trajectories make transitions to the lower-lying A and X states, shown on the left and right respectively. Transitions between these two lower states can also occur in the regions outlined with rectangles. For simplicity, we do not show the dynamics on the ${}^2\Pi_{u,3/2}$ state; it is accessible from the A' state and exhibits anomalous charge switching.

A main feature of the dynamics on the A' state is the narrow range of solvent coordinates observed in the coupling regions. One might expect that as $R_{\rm solute}$ increases the charge and solvent would tend to localize on a single iodine atom. But the A' surface has anomalous character; so that, as depicted in Fig. 3.1, solvent asymmetry creates charge flow toward the less solvated atom, which in turn pulls the solvent back towards more symmetric configurations. Anomalous charge switching thus creates a steep valley on the A' potential surface, funnelling trajectories into symmetric solvent configurations. The $n = 16$ trajectories begin with a fairly narrow range of solvent asymmetries that tightens somewhat upon dissociation. The funnel shape is more striking for $n = 9$, where there is a much broader range of initial solvent coordinates. For large initial $\Delta\Phi$, the charge jumps to the escaping atom which slows down and pulls solvent molecules away from the other atom until the solvent configuration becomes nearly symmetric.

Anomalous charge switching also prevents dissociation on the A' state, because the attraction of the CO_2 to I^- is so strong that the negative ion cannot escape. The A' funnel thus has a well in the dissociation coordinate that traps the trajectories in a region where the $R_{\rm solute}$ is about 5–7 Å. The maximal extension of the solute bond in

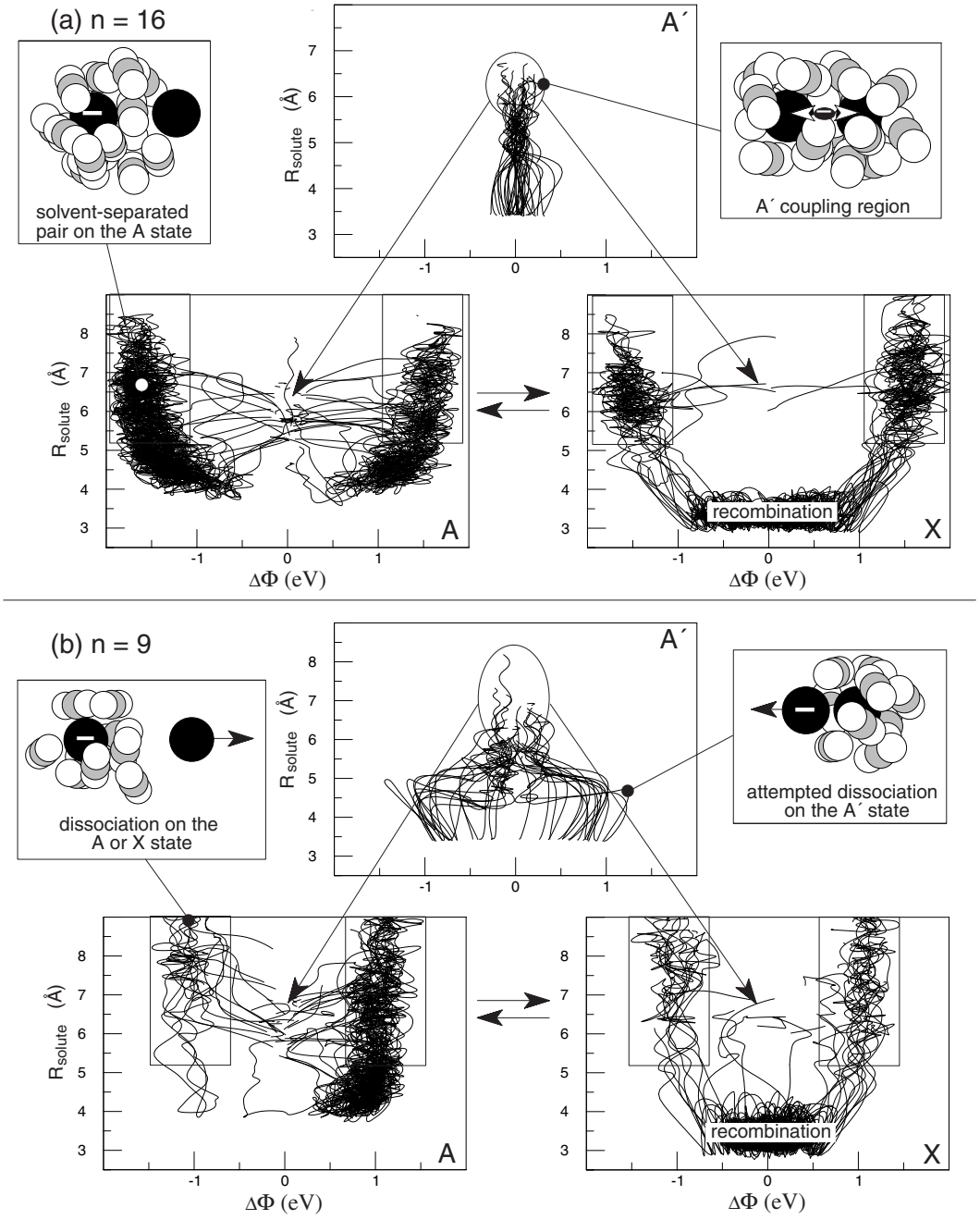

Figure 3.4: Dynamics of an ensemble of 41 trajectories projected onto the solute bondlength and the solvent coordinate for $n = 16$ (a) and $n = 9$ (b). Trajectories begin in the A' state at $R_{\rm solute}$=3.3 Å and undergo transitions to the lower states in the regions indicated with ovals. $A \leftrightarrow X$ coupling regions are marked with rectangles. The apparent favoring of the right side of the A state in (b) is due to the few trajectories that remain trapped for a long time.

the A' state is somewhat larger on average for $n = 9$ than $n = 16$, but dissociation cannot occur in either case or for any of the cluster sizes studied. In contrast, much larger separations and even I^- ejection were observed in simulations of comparable cluster sizes in $I_2^- Ar_n$ [12, 13].

Following the concerted dynamics in the A' state, electronic relaxation to the X and A states generally takes place less than one picosecond after photoexcitation. The effect of returning to a normal charge switching state is dramatic: charge localizes completely onto one solute atom and the solvent races to the ion, increasing the magnitude of $\Delta\Phi$ to 1 eV or more within 200-500 fs. Meanwhile, R_{solute} hardly changes. The disparity in response time of the solvent and the solute often results in a solvent-separated pair with CO_2 molecules tightly clustered to I^- and the I atom residing on the surface. These pairs, which were not observed in simulations of $I_2^- Ar_n$ clusters [12, 13], eventually either dissociate, via thermal evaporation of I, or recombine on the X state.

Trajectories are often trapped for extended periods in the A state prior to recombination or dissociation, as shown in Fig. 3.4. A state trapping is observed rarely in small clusters, but is common in cluster sizes $n \geq 7$. Both the frequency and length of trapping increase with cluster size. Residence times of 5–25 ps are typical, but product formation can require as long as 50–100 ps. We also observe transient recombination of I_2^-. That is, some trajectories pass within $R_{\mathrm{solute}} = 4$ Å the equilibrium bondlength, on the A state. However, the excited state I_2^- bond is weak compared to the $I^- \cdot CO_2$ solvation energy and the bond is broken before appreciable vibrational relaxation can occur. Nevertheless, both of these metastable cluster configurations contribute to the long lifetimes on the A state.

Formation of recombined products following trapping on the A state requires a coordinated sequence of events. The A state and the X state differ by the alignment of the empty p orbital on iodine. For $R_{\mathrm{solute}} > 5$ Å the alignment of that orbital is readily altered by collisions with solvent molecules [12, 30], causing electronic transitions back

and forth between these two states. To get recombination on the ground state, the solute bondlength must increase for the orbital to be realigned; simultaneously, neutral iodine must break into the first solvation shell, displacing CO_2.

On the ground state, the covalent bond is roughly an order of magnitude stronger than on the A state and is comparable in size to the total solute-solvent interaction. Once a trajectory reaches 5–6 Å on the X state, the strong bond force draws I_2^- back together; the solute rapidly recombines and the magnitude of the solvent coordinate never exceeds 0.5 eV thereafter. Trajectories that hop from the A' state to the X state at short bondlengths recombine directly in roughly 1–3 ps, without forming the solvent-separated pair.

There are two pathways for I_2^- dissociation. During trapping on the A state, neutral iodine is the most weakly bound species in the cluster and therefore readily evaporates. This is the dominant dissociation mechanism for $n \geq 9$. In the smaller clusters, dissociation is generally more direct, with R_{solute} increasing monotonically following the transition from the A' state. Direct dissociation arises because there are fewer solvent molecules to hold the solute atoms together.

3.2.3 Timescales

Figure 3.5 shows the ensemble-averaged populations in each electronic state as a function of time as determined from the 200 trajectory/10 ps ensembles. The two repulsive curves are very close in energy and are strongly coupled to each other, so we have added their populations together and referred to the sum as the A' population. Also, we have removed from the average those trajectories that dissociate within 10 ps. Trajectories reach the X state by two pathways: roughly 25% hop directly from A' to X, while the remainder hop first to the A state. No trajectories dissociate directly on the A' state. The figure shows that electronic relaxation is characterized by more than one time scale; for example, in the case of $n = 16$, trajectories leave the A' state in 1-2

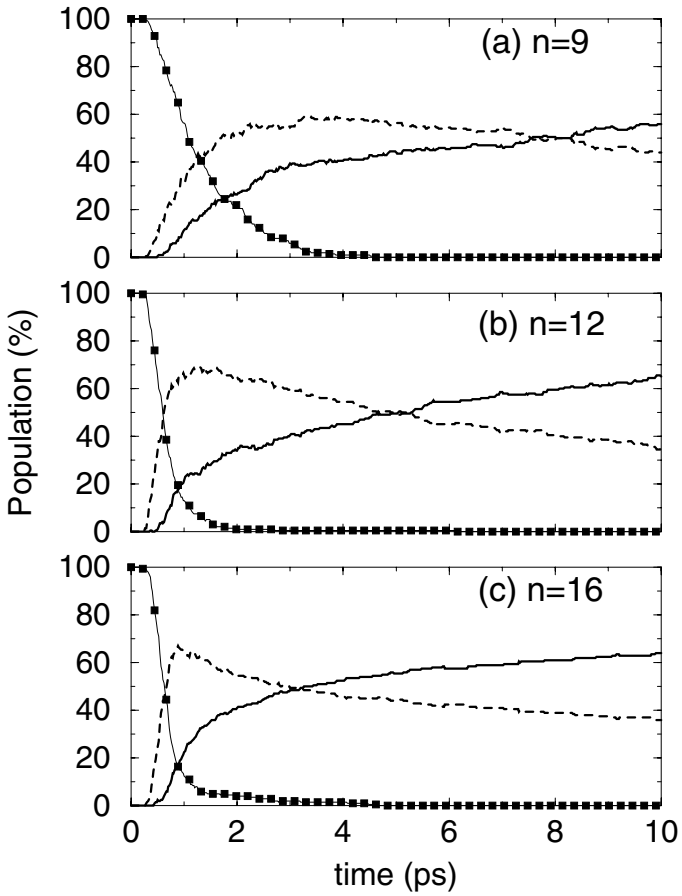

Figure 3.5: Ensemble average of the population of each solute electronic state vs. time for $I_2^-(CO_2)_n$. The A' state curve is marked with squares, dotted and solid lines correspond to the A and X states, respectively.

ps and the X state population rises to 50% by about 3 ps, after which there is a very slow relaxation from A to X. Eventually all of the A state molecules either relax or dissociate. As noted above, the I_2^- binding energy on the A state is only 100 meV, about half the binding energy of a single CO_2 molecule with I^-. The solvent thus tends to push apart the I_2^- bond and localize the excess charge. The resulting "solvent-separated pair", in which an I^- ion is weakly bound to several CO_2 molecules and one I atom, is shown in Fig. 3.6(b).

As the geometry of the hot cluster fluctuates, it passes through regions of strong coupling to the X state, where recombination can occur; alternatively, the solute may

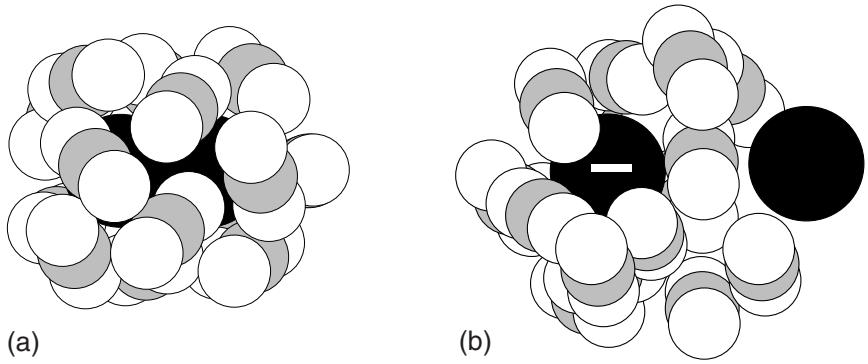

Figure 3.6: Typical configurations for $I_2^-(CO_2)_{16}$. (a) At equilibrium on the X state. (b) A solvent-separated pair on the A state.

completely dissociate via evaporation of the neutral iodine. The decay of these metastable clusters accounts for the slow transfer of population from the A to the X state. We define an overall recombination time by

$$\tau = \int_0^\infty f(t)dt, \tag{3.1}$$

where $f(t)$ is the fraction of trajectories that have not recombined at time t, including only those trajectories which ultimately recombine. From our 41 trajectory/200 ps ensembles we calculate τ to be 12.8, 10.1, and 17.1 ps for $n = 9$, 12, and 16, respectively. This value is dominated by the slow A to X relaxation and strongly influenced by the few trajectories that have very long recombination times, upwards of 50 ps in some cases; for most purposes it is more informative to inspect Fig. 3.5 directly.

3.3 Discussion

Perhaps the most surprising feature of this system is the remarkably high caging efficiency: simulation and experiment both show significant recombination for clusters having as few as 5 CO_2 molecules, less than one third of a solvent shell. Related to this is our observation that dissociation never takes place on the initially excited A' state. We explain these results in terms of the polarization of the charge distribution

on the solute by the solvent. In the electronic ground state, and in excited states that are primarily bonding in character, an asymmetric solvent environment causes the solute charge to flow towards the more favorably solvated I atom. In antibonding excited states, however, the charge moves in the opposite direction. This counterintuitive behavior, anomalous charge switching, may be understood in terms of a simple diatomic LCAO-MO picture. In the isolated molecule the atomic orbitals combine into bonding and antibonding molecular orbitals, both of which are delocalized. An asymmetric solvent environment polarizes the solute charge distribution to an extent that depends on the strength of the solute-solvent interaction relative to the bonding interaction. The bonding molecular orbital becomes distorted so that most of the wave function amplitude resides on the more solvated atom, and since the ground and excited states must remain orthogonal, the antibonding MO must polarize in the opposite direction. Thus charge flows towards the solvent in the ground state, and away from the solvent in the excited state. In other words, in an antibonding state the component of the molecular polarizability tensor parallel to the internuclear axis is negative.

In general, the magnitude and direction of charge flow depends on the details of the solute electronic structure, which in the halogens is affected by strong spin-orbit coupling. From our electronic structure calculations we find that the X and A states show normal charge flow, while the A' state shows anomalous charge flow at most internuclear distances. (In the immediate vicinity of the Franck-Condon region, charge flow on the A' state is normal, but trajectories leave this region too quickly for this to influence their dynamics.) Dissociation in the A' state thus requires ejection of an ion from the cluster. The nascent ion is held back by the electrostatic and polarization interactions with the neutral cluster that it is trying to escape, and in CO_2 clusters these forces are strong enough to suppress the direct dissociation pathway even in very small clusters. This contrasts with the more weakly bound Ar clusters, in which direct dissociation on the A' state is observed in the simulations, providing a likely expla-

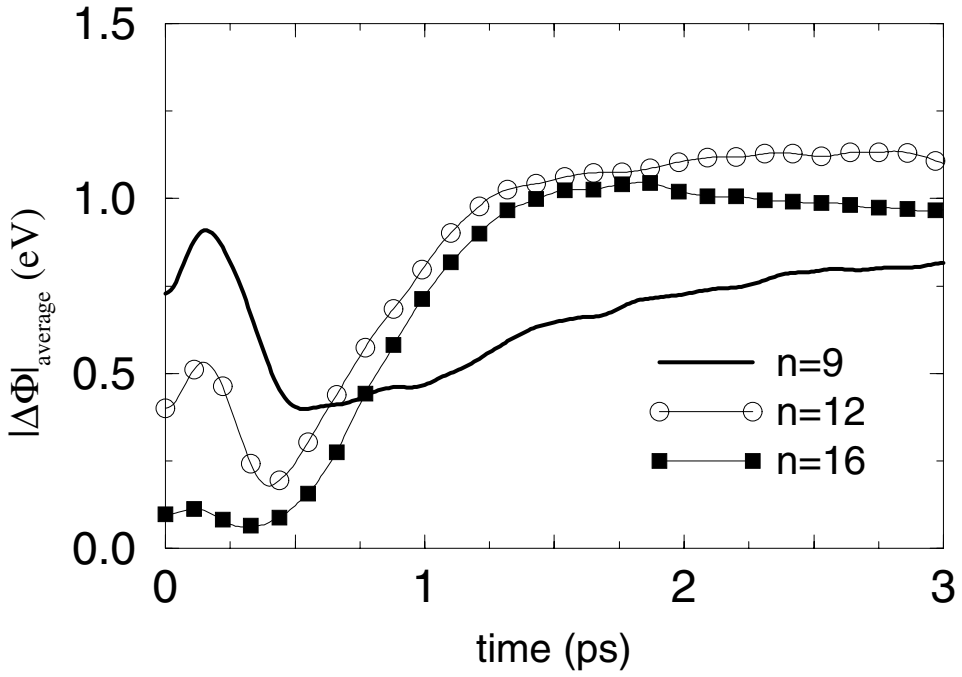

Figure 3.7: Ensemble average of the magnitude of the solvent coordinate vs. time for $n = 9$, 12, and 16. The rise at 500 fs is evidence of solvent rearrangement following electronic relaxation.

nation for the experimentally observed bimodal mass distribution in the dissociation products [12].

The contrast between anomalous charge flow on the A' state and normal charge flow on the A and X states also plays a key role in the electronic relaxation at short times. Figure 3.7 shows the ensemble average of $|\Delta\Phi|$ during the first 2 ps after excitation. As the equilibrium geometries in Fig. 3.3(a) illustrate, $I_2^-(CO_2)_9$ starts out from a much more asymmetric solvent geometry than $I_2^-(CO_2)_{16}$. The initial rise in the solvent asymmetry at about 200 fs arises from solute, not solvent, motion: the iodine atom that was initially less solvated moves away from the cluster of solvent molecules, so that $\Delta\Phi$ increases. After this, however, the escaping charge draws the solvent towards a more symmetric configuration, as illustrated by the sample trajectory shown in Fig. 3.8. This is characteristic of anomalous-state solvent dynamics—because the charge and the solvent move in opposition to each other, the energy minimum occurs

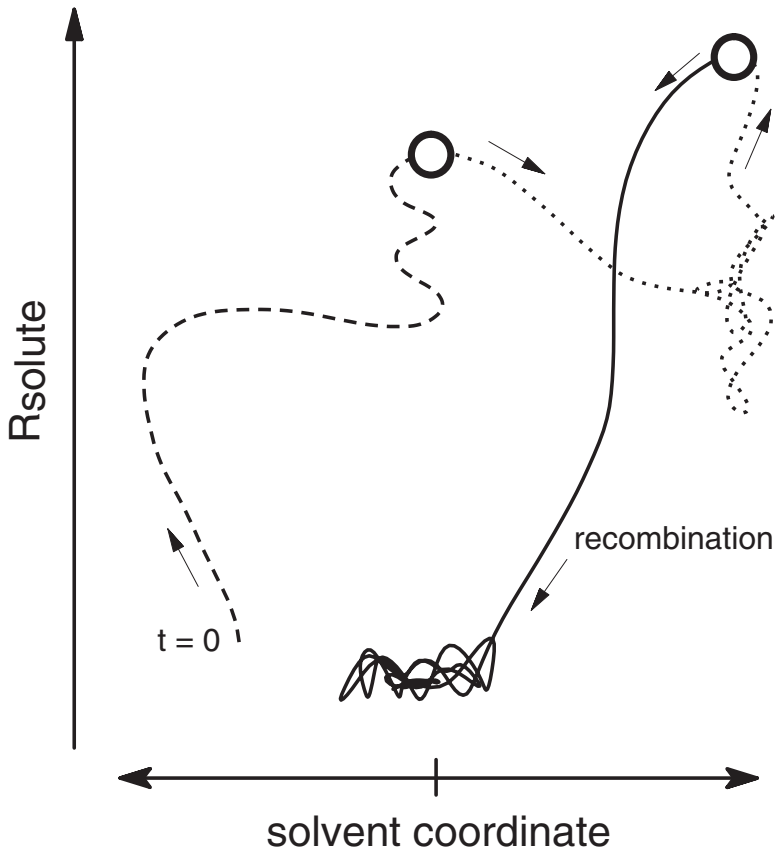

Figure 3.8: Schematic diagram of recombination following photodissociation from an asymmetric cluster configuration. Dashed line: initial dissociation on the A' state; dotted line: temporary trapping on the A state; sold line: recombination on the X state. Circles mark the location of surface hopping events.

at $\Delta\Phi = 0$. Nonadiabatic coupling to the A and X states becomes important at bond lengths of 5–7 Å and small values of $\Delta\Phi$, as shown by the central dark circle in Fig. 3.8. Because the nonadiabatic coupling is confined to symmetric solvent geometries, trajectories beginning from initially symmetric solvent configurations undergo nonadiabatic transitions to the A and X states at earlier times than those starting from asymmetric configurations. As shown in Fig. 3.5, the decay rate of the A' state population following photoexcitation increases as the cluster size is increased from 9 to 16 because the initial configurations become more symmetric.

The transition from anomalous charge switching on the A' state to normal charge

switching on the A or X states leads to a rapid increase in solvent asymmetry following the initial hop. At these longer bond lengths, the charge tends to localize on a single iodine atom, and because the solvent and the charge flow now act in concert, the solvent rearranges to stabilize the atomic ion, forming the solvent-separated pair mentioned earlier. The ion-solvent interactions are substantially larger than the A state potential well, so even though I_2^- separations characteristic of bound A-state I_2^- in the gas phase are observed, trajectories trapped in the A state always undergo transitions to the X state on a picosecond time scale. (In contrast, metastable $I_2^-Ar_n$ clusters in the A state have experimental lifetimes exceeding several microseconds [4].) Transitions from the A to X state require reorientation of the p orbital hole on the iodine atom and generally occur at somewhat longer bond lengths of 7–9 Å, where the solute electronic coupling is weak. The time scale on which these transitions occur appears to be governed by essentially diffusive motion along the I_2^- bond coordinate, as shown in Fig. 3.8. Hops to the X state may be followed by diffusive motion at long bond lengths, and hops back to the A state are possible. However, once the solute bond length is significantly less than 6 Å on the X state, the strong bonding interactions in the ground state lead to rapid recombination and vibrational relaxation of I_2^-, as Fig. 3.8 illustrates.

A major goal of these simulations has been to provide an interpretation of the picosecond pump-probe absorption experiments of Lineberger and co-workers [3, 5]. It is difficult to obtain a detailed picture of the photodissociation dynamics from these experiments alone because the absorption spectrum of I_2^- away from the equilibrium geometry is not known, and because the solvent may strongly affect the spectrum at these geometries. Simulation of the transient absorption spectrum from the trajectories is required to make a direct comparison between the simulations and the experiments (see Chapter 5); however, it is possible to discuss the general features evident in both. The experiments suggest a time scale of about 20 ps for the overall process of electronic and vibrational relaxation in $I_2^-(CO_2)_9$, decreasing to about 10 ps for $n = 16$ [3, 5].

The time scales generally agree with the time scales for electronic relaxation observed in the simulations, 10–20 ps, although the total relaxation time seems to be longer in the simulations at $n = 16$ than in $n = 9$. Both our simulations and previous theoretical investigations of I_2^- vibrational relaxation in the ground electronic state [6, 11] have found that the time scale for vibrational relaxation is very fast (1–2 ps) in comparison to the electronic relaxation times found here. Furthermore, our simulations indicate that the rate of vibrational relaxation—even near the bottom of the potential well—does not vary substantially with cluster size in CO_2 clusters. It is thus likely, as Papanikolas et al. [6] have conjectured, that the time scale for electronic relaxation is the major contributor to the overall probe absorption recovery signal.

A key finding of the Lineberger experiments was the appearance of a "bump" centered at around 2 ps in the absorption recovery for $n \geq 14$ [3]. This bump, which has also been observed by Barbara and co-workers in both polar and nonpolar solutions [9, 10, 31, 32], has been attributed to absorption from the inner turning point on A state following coherent recoil off the solvent cage. In the present simulations, motion along the I_2^- bond coordinate following electronic relaxation to the A state is diffusive, and a coherent return to short bond lengths in the excited state seems unlikely. As we have seen, the localization of charge on a single atom and the subsequent rearrangement of the solvent tends to keep the solute bond length large at short times. It is possible that the absorption bump arises from recoil in a small fraction of the ensemble that then absorbs strongly, but the simulations suggest another possibility. More than a quarter of the trajectories hop directly from the A' state to the X state and recombine within 1–3 ps. While the experiments of Barbara and co-workers in solution appear to rule out the possibility that the transient feature arises from absorption at the bottom of the ground state well, the simulations show that strong absorption is possible at bond lengths of about 4–5 Å near the top of the ground state well. As we will see in Chapter 5, the passage of a substantial fraction of the directly recombining trajectories through this

region gives rise to an observable transient absorption.

3.4 Conclusions

In summary, photoexcitation of I_2^- with a 790 nm photon places the solute on the A' electronic surface, which like the anomalous curves in Fig. 3.1, funnels the trajectories into highly symmetric solvent configurations as I_2^- dissociates. Following electronic relaxation, the A and X surfaces, like the normal charge switching curves in Fig. 3.1, pull the trajectories towards highly asymmetric solvent configurations. The electronic coupling on the A state is small, and the strong solute-solvent interactions destabilize the weak I_2^- bond, allowing formation of long-lived solvent-separated pairs. Eventually, trajectories in the A state either dissociate or hop to the X state, where the much larger electronic coupling creates a strong pull towards permanent recombination, which occurs rapidly if $R_{\mathrm{solute}} \leq 5$–6 Å. The strong ground state I_2^- bond also leads to direct recombination within a few picoseconds for a significant fraction of trajectories.

The results presented here show that the model is capable of reproducing the experimental product distributions, and illustrate how the electronic properties of the excited states and their interactions with the solvent drive the dynamics of photodissociation in clusters. These simulations also emphasize that the isolated I_2^- potential curves can be misleading when interpreting the dynamics of photodissociation and recombination in CO_2 clusters. When CO_2 is present, for example, the A' state is not dissociative, and I_2^- cannot recombine permanently in the A state. Previous analysis of pump-probe experiments in these clusters [3, 5] has used the isolated curves to locate the Franck-Condon regions for probe absorption. Our results suggest that coupling to the solvent will shift these regions significantly, leading to new interpretations of the experimental signals and the dynamics (see Chapter 5). Finally, while it is the large solvent asymmetry of the cluster environment that produces the interesting dynamics we report here, we anticipate that these effects may be an amplification of phenom-

ena which occur in the liquid phase as a result of solvent fluctuations. This possibility warrants further study.

References for Chapter 3

[1] L. Perera and F. G. Amar, J. Chem. Phys. **90**, 7354 (1989).

[2] J. Papanikolas, J. Gord, N. Levinger, D. Ray, V. Vorsa, and W. C. Lineberger, J. Phys. Chem. **95**, 8028 (1991).

[3] J. Papanikolas, V. Vorsa, M. Nadal, P. Campagnola, H. Buchenau, and W. C. Lineberger, J. Chem. Phys. **99**, 8733 (1993).

[4] V. Vorsa, P. J. Campagnola, S. Nandi, M. Larsson, and W. C. Lineberger, J. Chem. Phys. **105**, 2298 (1996).

[5] V. Vorsa, S. Nandi, P. J. Campagnola, M. Larsson, and W. C. Lineberger, J. Chem. Phys. **106**, 1402 (1997).

[6] J. M. Papanikolas, P. E. Maslen, and R. Parson, J. Chem. Phys. **102**, 2452 (1995).

[7] U. Banin, A. Waldman, and S. Ruhman, J. Chem. Phys. **96**, 2416 (1992).

[8] I. Benjamin, U. Banin, and S. Ruhman, J. Chem. Phys. **98**, 8337 (1993).

[9] D. A. V. Kliner, J. C. Alfano, and P. F. Barbara, J. Chem. Phys. **98**, 5375 (1993).

[10] P. K. Walhout, J. C. Alfano, K. A. M. Thakur, and P. F. Barbara, J. Phys. Chem. **99**, 7568 (1995).

[11] I. Benjamin, P. F. Barbara, B. J. Gertner, and J. T. Hynes, J. Phys. Chem. **99**, 7557 (1995).

[12] J. Faeder, N. Delaney, P. Maslen, and R. Parson, Chem. Phys. Lett. **270**, 196 (1997).

[13] V. S. Batista and D. F. Coker, J. Chem. Phys. **106**, 7102 (1997).

[14] B. J. Greenblatt, M. T. Zanni, and D. M. Neumark, Science **276**, 1675 (1997).

[15] B. J. Greenblatt, M. T. Zanni, and D. M. Neumark, Faraday Discuss. **108**, 101 (1997).

[16] P. E. Maslen, J. M. Papanikolas, J. Faeder, R. Parson, and S. V. ONeil, J. Chem. Phys. **101**, 5731 (1994).

[17] R. A. Marcus, Ann. Rev. Phys. Chem. **15**, 155 (1964).

[18] M. D. Newton and N. Sutin, Ann. Rev. Phys. Chem. **35**, 437 (1984).

[19] G. C. Schatz and M. A. Ratner, Quantum Mechanics in Chemistry, chapter 10, Prentice Hall, Englewood Cliffs, 1993.

[20] P. E. Maslen, J. Faeder, and R. Parson, Chem. Phys. Lett. **263**, 63 (1996).

[21] C. S. Murthy, S. F. O'Shea, and I. R. McDonald, Mol. Phys. **50**, 531 (1983).

[22] C. G. Gray and K. E. Gubbins, Theory of Molecular Fluids, volume 1, Clarendon, Oxford, 1984.

[23] Y. Zhao, C. C. Arnold, and D. M. Neumark, J. Chem. Soc. Faraday Trans. **89**, 1449 (1993).

[24] H. C. Andersen, J. Comput. Phys. **52**, 24 (1982).

[25] J. C. Tully, J. Chem. Phys. **93**, 1061 (1990).

[26] S. Hammes-Schiffer and J. C. Tully, J. Chem. Phys. **101**, 4657 (1994).

[27] J. M. Papanikolas, I_2^- Photodissociation and Cage Recombination Dynamics in Size-Selected $I_2^-(CO_2)_n$ Clusters, PhD thesis, University of Colorado, 1994.

[28] F. G. Amar and L. Perera, Z. Phys. D **20**, 173 (1991).

[29] V. Vorsa, Photodissociation Dynamics of Mass-Selected Anions and Anionic Clusters, PhD thesis, University of Colorado, 1996.

[30] A. I. Krylov, R. B. Gerber, and R. D. Coalson, J. Chem. Phys. **105**, 4626 (1996).

[31] A. E. Johnson, N. E. Levinger, and P. F. Barbara, J. Phys. Chem. **96**, 7841 (1992).

[32] J. Alfano, Y. Kimura, P. K. Walhout, and P. F. Barbara, Chem. Phys. **175**, 147 (1993).

Chapter 4

Simulation of UV Photodissociation of $I_2^-(CO_2)_n$: Spin-orbit Quenching via Solvent Mediated Electron Transfer

In the decade that has passed since the pioneering experiments of Lineberger and co-workers [1, 2], dihalide ions have become favorite models for studying the effects of strong solvent-solute forces on elementary chemical reactions. In particular, I_2^- has been studied in a wide variety of environments, including gas phase clusters [3–12], liquid solutions [13–21], and gas-surface collisions [22–25], and these experiments have stimulated a variety of theoretical studies [26–47]. These solvated molecular ions differ considerably from their neutral counterparts, since the interaction between the ion and the surrounding solvent, which can be as strong as the chemical bonding forces within the solute, depends sensitively on the solute charge distribution. The electronic structure of the solvated ion is subject to strong perturbations that depend on the coordinates of the solvent molecules. Therefore, the dynamics take place on multidimensional potential energy surfaces that cannot be represented in terms of pairwise interactions at even the lowest level of approximation. We are thus confronted by two sorts of challenges: to develop an accurate method for simulating dynamics on these surfaces, and to devise a conceptual picture with which to interpret the results of these simulations and to predict the results of proposed future experiments.

Within the past two years the technical challenge has been met through the development of effective Hamiltonian descriptions of the electronic structure of the interact-

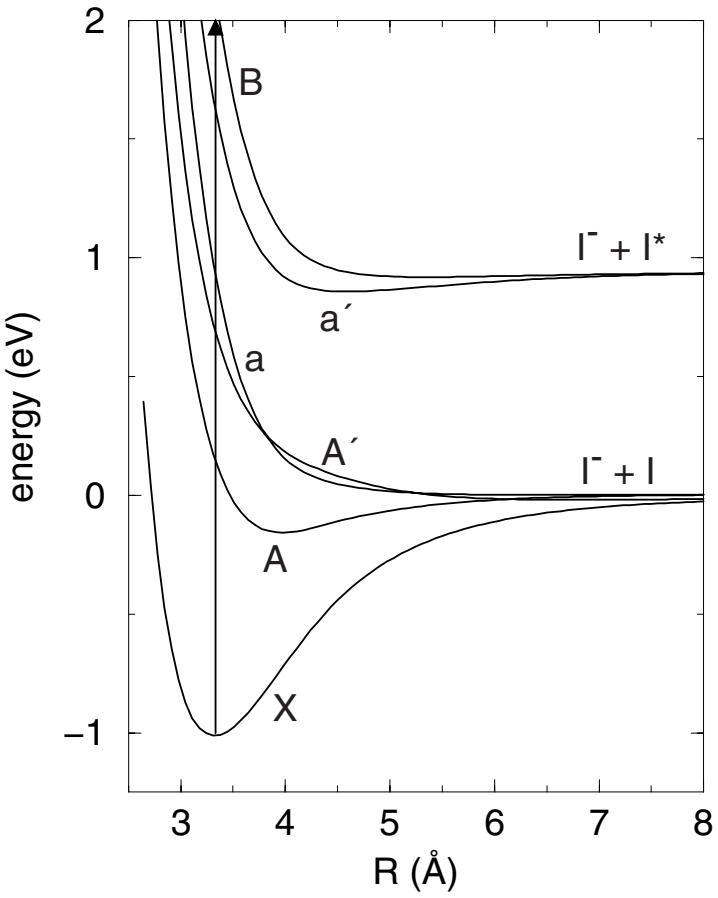

Figure 4.1: Scaled **ab initio** gas phase potential curves for I_2^-. The arrow shows the 395 nm photoexcitation to the $B\ ^2\Sigma^+_{g,1/2}$ state modeled in the current simulations.

ing solute-solvent system [41–46]. Nonadiabatic molecular dynamics simulations computed with these Hamiltonians have successfully reproduced the results of both time-independent and time-dependent experiments. The results of these simulations demonstrate that physical pictures based on the isolated molecule potential curves can be highly misleading. For example, the gas phase photodissociation of I_2^- at 790 nm takes place directly on the repulsive A' state (Fig. 4.1); however, both simulations [43, 46] and experiment [11] show that in a cluster of CO_2 molecules this channel is closed and that dissociation only occurs via nonadiabatic transitions to the lower A and X states.

In recent papers [43, 45] we have attempted to meet the conceptual challenge by

developing a pictorial representation inspired by the theory of electron transfer reactions in solution [48–50]. The underlying idea is that crucial aspects of the dynamics are determined by the competition between solvation forces, which tend to localize the solute charge distribution on a single atom, and chemical bonding forces, which prefer a delocalized molecular charge distribution. This motivates us to interpret the solvent dynamics in terms of a collective "solvent coordinate," defined in terms of the electrostatic potential that the solvent exerts at the two solute atoms. This coordinate describes the energetic asymmetry of the local solvent environment; the competition between solvation and chemical bonding can be illustrated by plotting the simulation trajectories as a function of the solute bondlength and of this solvent asymmetry coordinate. The clear and simple patterns displayed when the dynamics are presented this way help untangle the dynamics of solvent-induced nonadiabatic transitions.

In this chapter we present the results of the simulation of the photodissociation of I_2^- following excitation at 395 nm, which brings the solute to states that correlate, in the isolated molecule, to a spin-orbit excited iodine atom (I^*) and an I^- ion, and extend the conceptual framework outlined above to aid in interpreting these dynamics. We describe an efficient mechanism for quenching the spin-orbit excited states when the molecule is embedded in a cluster. This mechanism, first suggested during our earlier study of I_2^- in a uniform electric field [36], involves charge transfer from a nascent solvated I^- ion to the I^* atom, yielding I^- and solvated I in its spin-orbit ground state. The 0.94 eV energy gap between I and I^* is compensated by the difference between the ion and neutral solvation energies. The molecular dynamics simulations demonstrate that spin-orbit quenching is indeed efficient, and analysis of the simulations using the electron-transfer picture confirms the proposed mechanism. In a recent paper, Sanov et al. provide convincing experimental evidence for the process as well [51]. Both simulation and experiment find that the time scale for electronic relaxation is a few picoseconds, orders of magnitude faster than observed for the collisional quenching of

I^* by CO_2 [52] or the electronic relaxation of I^* pairs in liquids and in solid matrices [53, 54].

The chapter is organized as follows. Section 4.1 gives a brief overview of the simulation methods; a complete discussion may be found in references [44] and [45]. The products of the trajectory simulations are described in Sec. 4.2. Section 4.3 focuses on the dynamics we observe in a range of cluster sizes around half a solvation shell ($n = 6$–13), highlighting the onset of spin-orbit relaxation. Section 4.3.1 describes the effects of solvation on the electronic states of I_2^-, and forms the framework for our discussion of the dynamics. In Appendix B, these ideas are illustrated in more detail using a simple one-electron Hamiltonian analogous to those used in the theory of electron transfer. Details of the initial photofragmentation process are presented in Sec. 4.3.2, and support for the proposed solvent-mediated relaxation of I^* is given in Sec. 4.3.3. The dynamics are summarized in Sec. 4.3.4 and Sec. 4.4 concludes the chapter.

4.1 Methods

The simulations described here use the same effective Hamiltonian model as our earlier studies of photodissociation dynamics at 790 nm [43, 45]. While in the earlier studies the electronic states that correlate to spin-orbit excited iodine were not populated, they were included in the basis states of the Hamiltonian, so no significant changes are required to apply the model to UV photodissociation. The interaction between the solute I_2^- and the solvent CO_2 molecules is described by an operator that includes state-dependent electrostatic and induction interactions between the solute and solvent based on **ab initio** calculations of the solute wave functions [55] and experimental data for the solvent charge distribution [56] and polarizability [57]. The one electron density matrix derived from the solute wave functions is expanded in distributed multipole operators [58]; diagonal elements of the distributed multipoles describe the solute charge density in various electronic states, while off-diagonal elements describe

transition charge densities that allow for polarization of the solute charge density by the solvent. State-independent atom-atom Lennard-Jones potentials account for the remaining dispersion and repulsion interactions; these are fit to reproduce the known I^-—CO_2 and I—CO_2 potential curves [59]. The CO_2—CO_2 interaction potential is taken from Murthy et al. [56]. This model captures the sensitive dependence of the solute charge distribution on the solute electronic state, the solute bondlength, and the positions and orientations of the solvent molecules.

At each time step the matrix of the effective Hamiltonian, which depends parametrically upon the coordinates of all the solute and solvent nuclei, is constructed and diagonalized, yielding the energies, forces, and nonadiabatic transition matrix elements required to proceed to the next step; distributed multipole analysis allows us to derive compact analytical expressions for these quantities [45]. Nuclear motion on a single potential surface is computed using the velocity version of the Verlet algorithm [60], while hopping between surfaces is computed using Tully's method [61, 62] with some minor modifications to account for nuclear decoherence [42, 45]. Since the trajectories are integrated in the adiabatic representation, phenomena such as charge transfer do not necessarily involve a transition between states, but can instead take place adiabatically as a trajectory moves through an avoided crossing region.

For each cluster size studied, 100 trajectories were computed from starting configurations obtained by sampling a single 1 ns trajectory with an average temperature of 80 K. This temperature was chosen to lie on the upper end of the solid-liquid phase transition region in the clusters, based on our previous experience that such temperatures gave reasonable agreement with experimental results [42] (the experimental cluster temperatures are known only very approximately [63]). The products are determined by integrating the trajectories until the nuclear configuration meets either of two criteria: the I–I distance exceeds 40 Bohr, or I_2^- undergoes more than 25 oscillations in a particular potential well. The dissociation and recombination times vary from a

couple of picoseconds to over 100 ps in some cases where I_2^- is temporarily trapped in an excited electronic state. The time scale for evaporation of CO_2 molecules from the clusters following photodissociation appears to be much longer than the 2–100 ps over which the trajectories are integrated, and thus our mass distributions are expected to be shifted to larger mass with respect to the experimental results, which are measured at 5–10 μs [3, 64].

4.2 Photofragmentation Product Distributions

The fragments resulting from photodissociation of $I_2^-(CO_2)_n$ at 395 nm can be grouped into three product channels, two of which correspond to a dissociated solute (I^- + I) and one to a recombined solute (I_2^-). The two dissociative channels differ in the average number of CO_2 molecules left surrounding the I^- fragment. This difference is energetically consistent with the amount of CO_2 evaporation that is expected to follow internal conversion of the iodine spin-orbit energy into solvent motion [51], and our simulations allow us to confirm that the heavy I^--based fragments result from dissociation on the a' excited spin-orbit state (see state labels, Fig. 4.1), whereas both the light I^--based fragments and the recombined fragments require relaxation to the lower spin-orbit states of I_2^-. The relative intensity of each product channel as a function of the initial cluster size is shown in Fig. 4.2.

Figure 4.3 shows the mass distribution of products from simulated photodissociation of $I_2^-(CO_2)_n$ for selected cluster sizes at 395 nm. We expect our distributions to be shifted to larger mass relative to the experimental distributions since the trajectories are terminated before solvent evaporation is complete. For cluster sizes $n \leq 7$ we see a single mode of I^--based products centered at about $k = n-3$, corresponding to dissociation to solvated I^- + I^*. At $n = 8$, there is essentially still a single mode of dissociative products, however, 2% of the trajectories undergo spin-orbit relaxation before dissociating. For $n = 9$, about 35% of the trajectories are spin-orbit quenched, and there is a

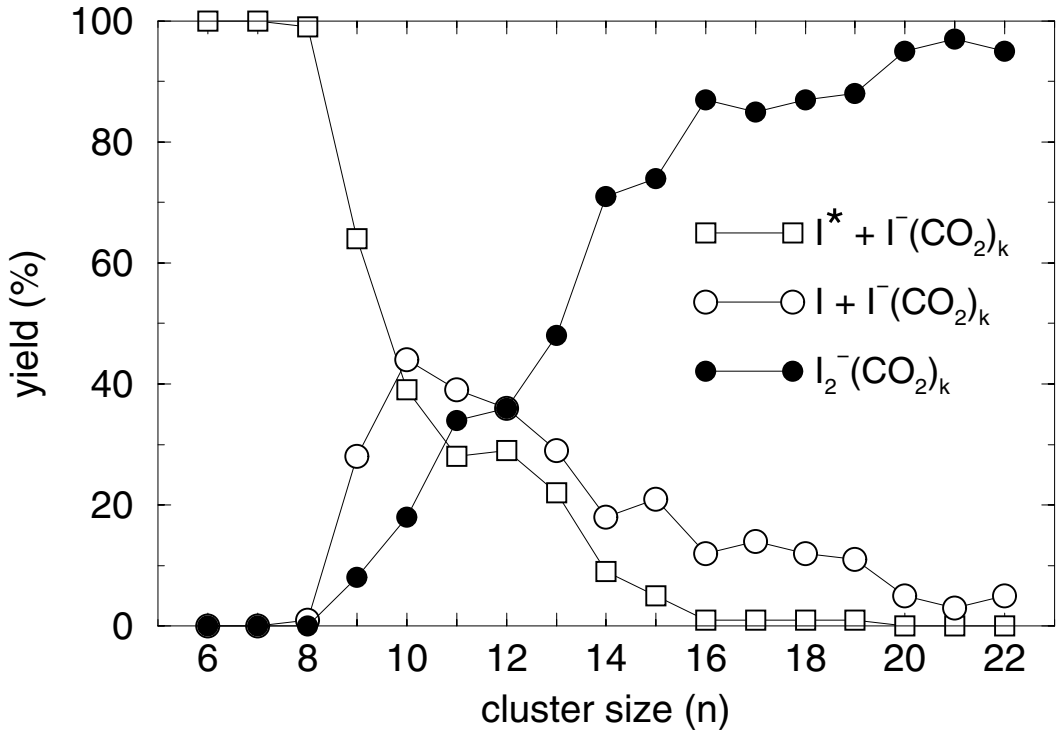

Figure 4.2: Branching ratios for the products of $I_2^-(CO_2)_n$ photodissociation at 395 nm. $1\sigma = \pm 5\%$

distinct second peak in the mass distribution of I^--based products corresponding to the loss of 3–4 additional CO_2 molecules. Also, we begin to see recombined I_2^- products. This sharp onset of spin-orbit relaxation is discussed in Sec. 4.3. By $n = 11$ the three product channels are roughly equal in intensity, and as the cluster size increases ground state recombination becomes the dominant product. By $n = 20$, dissociation to I^- + I^* is no longer observed, but dissociation on the lower spin-orbit states is not completely quenched at $n = 22$, the largest cluster size studied.

These trends are in broad agreement with the experimental observations of Sanov et al., although there are significant differences in detail. In particular, we do not see the finely structured dependence of the caging fraction on cluster size that is reported experimentally. Nor do we see the recombination channel opening at smaller cluster sizes than dissociation from the lower spin-orbit states. Finally, the simulations overes-

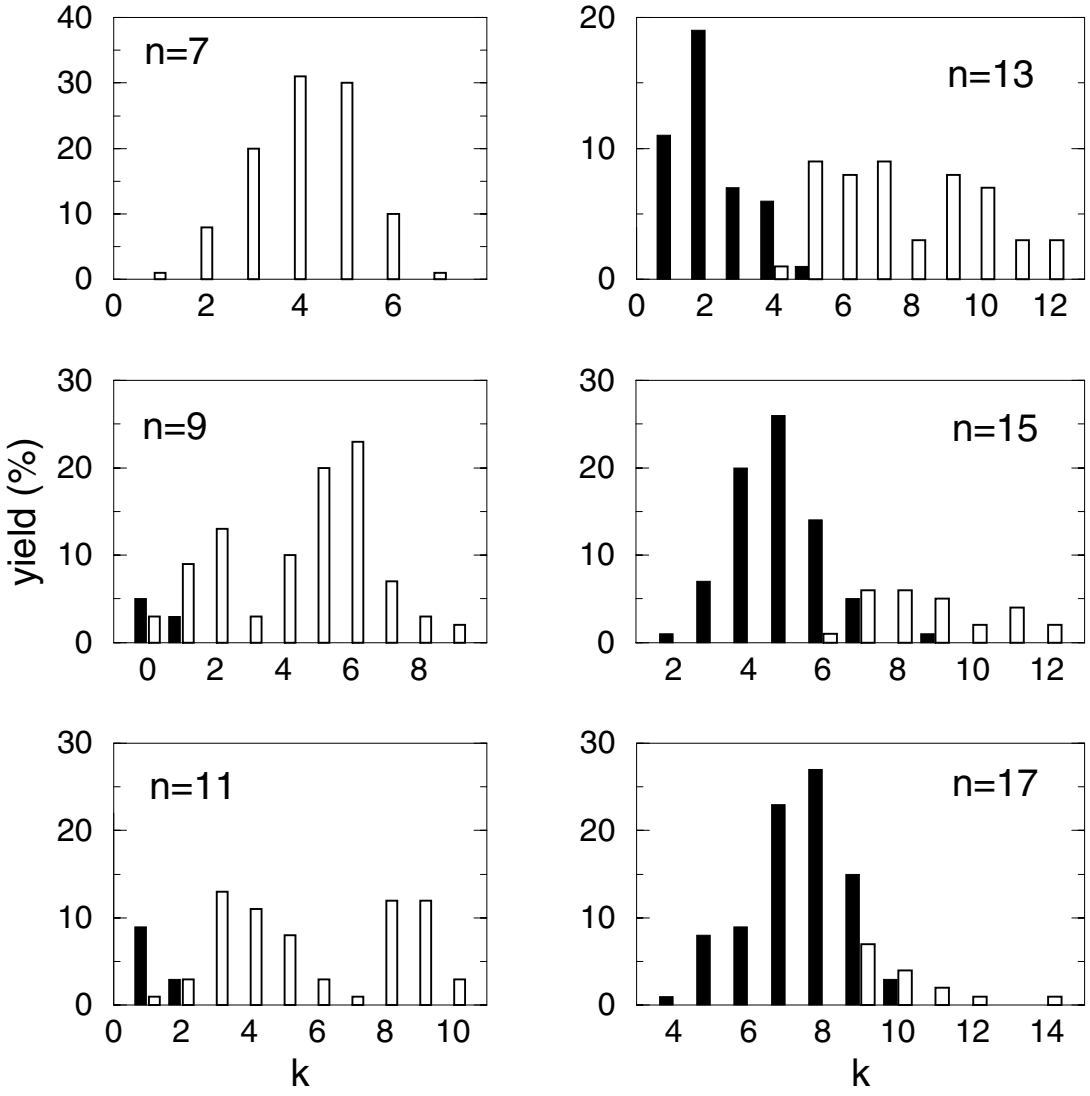

Figure 4.3: Simulated mass distribution of products for selected cluster sizes. Open bars represent I^--based products, filled bars represent I_2^--based products. The high mass dissociative fragments are produced in conjunction with I^*, while the low mass fragments are accompanied by I in its ground spin-orbit state.

timate the caging fraction for intermediate and large cluster sizes. These discrepancies contrast with our earlier simulation of 790 nm photodissociation [43], where quantitative agreement with experimental branching ratios was achieved, and suggest that UV photodissociation provides a more sensitive test of the simulation model. Nevertheless, the simulations and experiments deliver the same overall message: spin-orbit quench-

ing, which is completely absent in the isolated molecule and in the smaller clusters, suddenly becomes efficient in clusters having more than 7–8 CO_2 molecules.

4.3 Dynamics

4.3.1 Qualitative picture of solvent-mediated electronic relaxation

The photofragmentation process is driven by the interaction between the solvent molecules and the changing charge distribution of I_2^- in its various electronic states. Since the electronic structure of the solute is strongly perturbed by the solvent, it is often misleading to interpret the dynamics in terms of the potential curves of isolated I_2^- alone [43]. In the present case, the most interesting features of the relaxation dynamics take place at solute bondlengths of 5–10 Å, where the potential energy curves of isolated I_2^-, shown in Fig. 4.1, are nearly flat. Under these circumstances the dynamics are dominated by motions within the solvent. A similar situation arises in the theory of electron transfer in solutions [48–50], where the "reaction coordinate" consists of solvent reorganization, and in previous work we have used a schematic picture inspired by the classical Marcus theory [48] to interpret the photofragmentation process following excitation at 790 nm. Here we extend this picture to include the states that correlate to spin-orbit excited iodine. With this model to guide the analysis of our simulations, we demonstrate that the mechanism for spin-orbit relaxation of I_2^- inside the cluster is a form of solvent-induced charge transfer. In Appendix B, we examine these ideas in more depth using a simple one-electron model Hamiltonian. We emphasize that these simple models are only used to interpret the simulation results, not to calculate them. As described in Section 4.1, the simulations use an effective Hamiltonian that explicitly includes all of the solvent molecules and an accurate representation of the solute charge distribution based on a distributed multipole analysis of the **ab initio** wave functions.

Figure 4.4 displays the electronic energy levels of I_2^- at large internuclear dis-

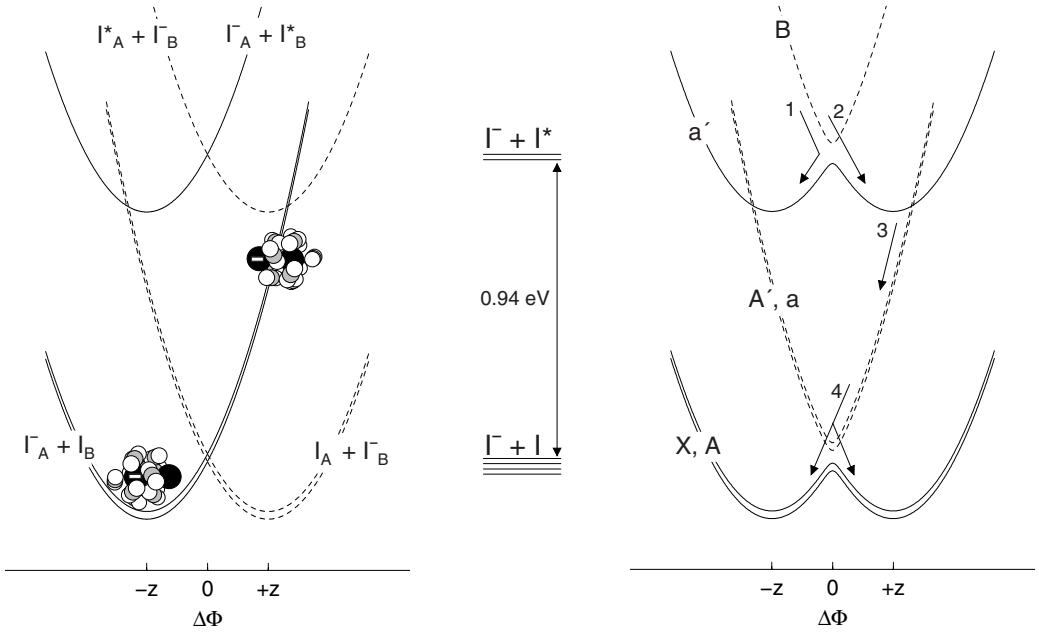

Figure 4.4: Solvation effects on the solute potential energy at intermediate to large solute bondlengths. Center: energy levels of isolated I^- + I in its two lowest electronic states. Left hand panel: diabatic energy vs. solvent coordinate, $\Delta\Phi$. Right hand panel: adiabatic states associated with molecular state labels of I_2^-. States B, A' and a exhibit anomalous charge flow. Arrows depict relaxation pathways observed in trajectories.

tances where both the spin-orbit energy and the ion solvation energy exceed the chemical bonding interaction between I and I^-. The center panel shows the energy levels of the isolated solute. The two upper states correlate to I^- + I^*, while the four lower states represent I^- + I; these levels are separated by the atomic spin-orbit splitting of 0.94 eV. The remaining panels in the figure show how these energy levels are influenced by the solvent. For this purpose we introduce a collective coordinate that describes the asymmetry of the local environment around the solute. The "solvent coordinate" is defined as the electrostatic potential difference between the two I atoms, i.e., the difference in energy when a charge of $-e$ is moved from I_A to I_B holding all nuclear coordinates fixed. The magnitude of the solvent coordinate, $\Delta\Phi$, is small when the solvent molecules are nearly equally shared between the two iodine nuclei (a "symmetric" cluster) and large

when one nucleus is preferentially solvated (an "asymmetric" cluster).

In the left hand panel we adopt a diabatic picture in which the $I\cdots I^-$ resonance coupling is neglected. The energy of the solute-solvent system is minimized when the ion charge is localized on a single atom and the solvent surrounds that atom. Since the charge may reside on either iodine atom, this leads to two equivalent minima when the energy is plotted against the solvent coordinate; these minima are located in the figure at $\Delta\Phi = \pm z$. Associated with each minimum is a diabatic potential curve which, to a first approximation, depends quadratically on the solvent asymmetry coordinate; motion along this "Marcus Parabola" entails reorganizing the solvent cluster while holding the electronic charge distribution fixed. For example, the minimum at $-z$ corresponds to solvated I_A^- + I_B, and as the system moves along the diabatic curve towards larger values of $\Delta\Phi$ the cluster becomes more symmetric, which raises the electronic energy since the solvent molecules are on average further away from the solute charge. When the solvent coordinate has reached a value of $+z$, the solvent has moved all the way from I_A^- to I_B, incurring a large energetic penalty, and at sufficiently large solvent coordinates the solvation energy exceeds the spin-orbit splitting energy so that the diabatic states of ground state iodine cross those associated with I^*. At zero solvent coordinate the symmetrically equivalent pairs of diabatic states intersect and the degeneracy pattern of isolated I_2^- is recovered. The actual solvent motions involved in this problem are different from those invoked in the usual Marcus picture. In classical Marcus theory solvent reorganization is brought about by reorientation of the dipolar solvent molecules, whereas here the solvent cage moves from one side of the solute to the other. Thus the solvent coordinate can be very large in these systems even though our solvent molecules have no permanent dipole moments.

In the right hand panel we restore the electronic coupling to a value corresponding to a solute bondlength of 7–10 Å. The crossings at zero solvent coordinate become avoided crossings, and we can attach the molecular state labels of I_2^- to the resulting

curves [65]. A comparison to the diabatic curves in the left hand panel illustrates the two types of charge flow that we have identified in these systems. At the point $-z$ on the A or X state the charge is localized on I_A and the solvent favors this end of the diatom. Moving towards a solvent coordinate of $+z$ along the lower adiabatic curve, the solute charge and the solvent environment reorganize in concert, crossing a barrier at $\Delta\Phi = 0$ and resulting in I_A + solvated I_B^-; we have called this "normal charge flow." In contrast, a vertical excitation from the system at point $-z$ on the A or X state to the antibonding A' or a state corresponds to shifting the balance of charge from I_A to I_B while the solvent remains near I_A. As the solvent migrates away from I_A, towards the excess charge, the solute electronic energy rapidly decreases. However, after crossing zero solvent coordinate, the electronic character of the state changes to I_A^- + I_B, and the solvent is once again on the uncharged end of the solute. Thus during adiabatic motion on the upper curve the solute charge and the solvent environment move in opposition to each other; we have called this "anomalous charge flow" [36, 37, 42, 43, 45]. The same dichotomy applies to the two states of the upper spin-orbit manifold: charge flow is normal on the a' state and anomalous on the B state [36]. This illustration of the origin of normal and anomalous charge flow states is complementary to the explanation we gave in Ref. [45], Sec. 5. In a simple diatomic LCAO-MO picture of I_2^- the atomic orbitals of I^- and I combine to produce delocalized bonding and antibonding molecular orbitals. An asymmetric solvent environment polarizes the solute charge distribution in the bonding state so that the excess charge resides mostly on the more solvated atom. Since the ground and excited states must remain orthogonal, the charge localizes on the less solvated atom in the antibonding state. In general, states that are predominantly bonding in character exhibit normal charge flow, while states that are predominantly antibonding in character exhibit anomalous charge flow. The validity of this description for charge flow in these systems is demonstrated by the good agreement between the experimental and simulated photodissociation products of $I_2^-Ar_n$ clusters [42]. The

key distinction between states with normal and anomalous charge flow is the location of the energy minimum along the solvent coordinate. States showing anomalous charge flow funnel the system towards symmetric cluster configurations, while states showing normal charge flow favor an asymmetric cluster environment.

With the aid of Fig. 4.4, we can identify the types of electronic transitions and the relaxation pathways observed in our system. An excitation of 395 nm takes the system to the B state, and transitions to the a' state occur when the solvent coordinate is nearly zero. A simple diabatic passage through this region corresponds to solvent transfer, in which the solvent cage moves from one side of the solute to the other while the electronic charge distribution is unchanged. This is indicated by arrow 2 on Fig. 4.4. If, however, the excess charge is transferred from one iodine atom to the other as the system moves through the coupling region, the solvent returns to the side on which it began, as illustrated by arrow 1. In this respect, the short-time dynamics on the B state following UV excitation resemble those observed on the A' state following visible excitation [45, 46]. Once on the a' state, however, the system may hop to the A' or a state at the points of intersection with the a' curve, arrow 3. This charge transfer differs from transitions seen in our 790 nm simulations, in that it occurs only from highly asymmetric solvent configurations. Following this charge transfer to the lower spin-orbit states, reorganization and evaporation of solvent molecules dissipate the excess potential energy and return the system to the coupling region between the a/A' and A/X states, where both solvent and charge transfer transitions take place, shown by arrow 4. Sections 4.3.2 and 4.3.3 describe the results of our nonadiabatic dynamics simulations within this framework.

4.3.2 Early Times: Spin-Orbit Excited States

Before photoexcitation, the solute is at equilibrium in its ground (X) electronic state, where the I_2^- bond is stable relative to the solute-solvent interactions of roughly

200 meV per CO_2 molecule. Clusters in the size range $n = 6$–13, on which we focus this discussion, contain approximately half a solvation shell of CO_2 molecules, which group together about one end of I_2^-, producing an asymmetric solvent environment [27, 37, 43, 46].

At $t = 0$, the solute is promoted to the repulsive B state. The excess charge flows rapidly to the less solvated iodine atom, and the solvent responds to this change in the solute polarization on a time scale of a few hundred femtoseconds. The I_2^- bondlength increases to 5 Å in roughly 150 fs, before translational motion of the solvent molecules begins. As R_{solute} increases, the charge becomes fully localized on the less solvated iodine and moves further away from the solvent. The Coulombic attraction between I^- and the CO_2 cluster slows and ultimately prevents dissociation on the B state [66]. The CO_2 molecules continue to move towards the charge, though, making the solvent environment more symmetric. By this point the solute bondlength is sufficiently extended that the a' and B electronic states become degenerate as the solvent coordinate approaches and passes through zero, and nonadiabatic transitions begin to take place. Figure 4.5 shows the population of the B and a' electronic states versus time for selected cluster sizes. For all cluster sizes studied, trajectories begin hopping to the a' state at about 200 fs, and most have made the transition by 500 fs. Once on the a' state, the solvent can catch I^- and dissociation can proceed. For clusters with seven or fewer CO_2 molecules, R_{solute} increases monotonically following transition to the a' state, producing solvated I^- and I^*; we refer to this as direct dissociation. The average times required to reach an I^*–I^- separation of 40 Bohr (≈20 Å) are 1.9 and 3.7 ps for $n = 6$ and 7, respectively.

Although direct dissociation accounts for some of the products in larger cluster sizes, other mechanisms become possible with increased solvation. For $n = 8$, where a single product mode is observed in the mass distribution, two types of trajectories are observed. The products with five or more CO_2 molecules are formed by direct

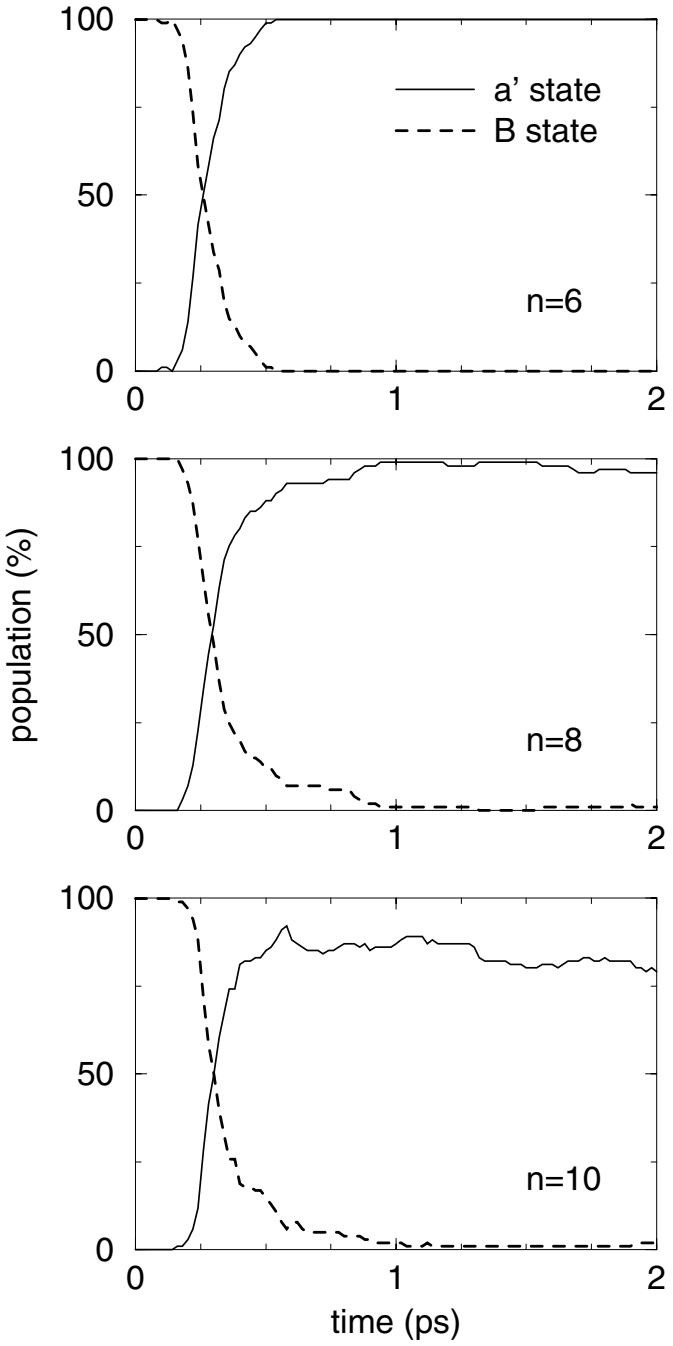

Figure 4.5: B and a' electronic state populations vs time n = 6,8, and 10. The tail in the B state population is evident in cluster sizes $n = 8, 9, 10$ and to a lesser degree $n = 11$. A similar lengthening of the time for electronic relaxation from the A' state was observed in our simulations of photodisociation at 790 nm and was attributed to the time required for solvent rearrangement to occur in asymmetric clusters.

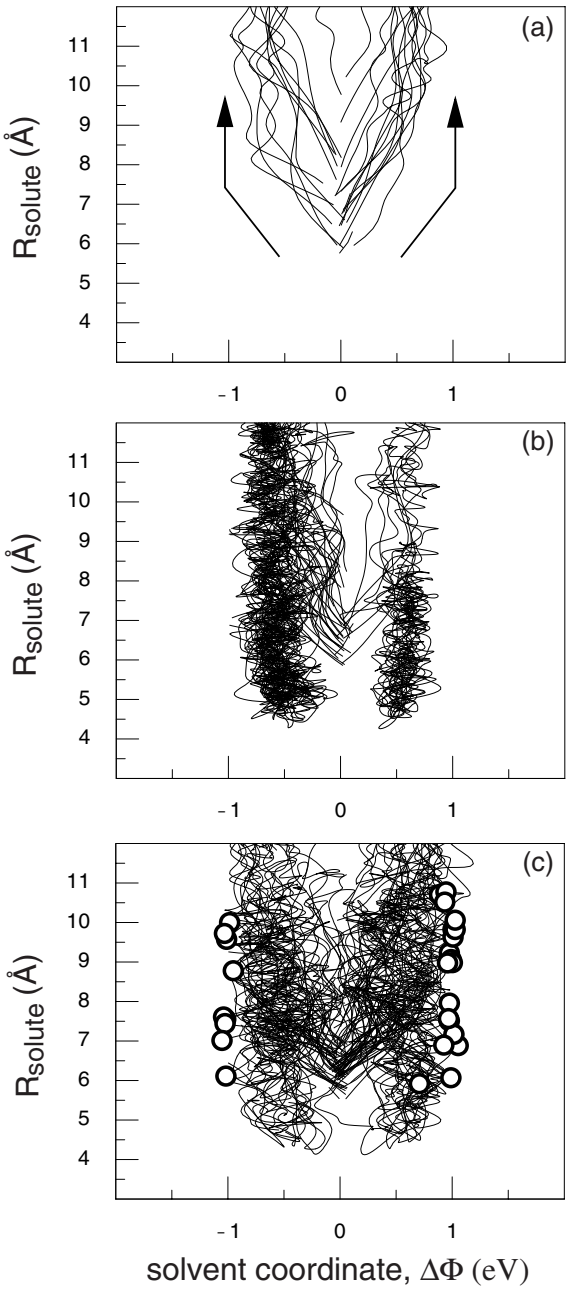

Figure 4.6: Motion on the a' state for selected trajectories with $n = 8$ (a,b) and $n = 9$ (c). (a) Trajectories producing heavy fragments (6 or 7 solvent molecules remain) dissociate directly on the a' state. (b) Trajectories producing fragments with 4 solvent molecules predominantly undergo transient trapping on the a' state before dissociating. (c) Trajectories that relax to the lower spin-orbit states. The transitions, marked by the circles, occur near $\Delta\Phi = \pm 1$ eV, just beyond the solvent coordinates accessed in $n = 8$ trajectories.

dissociation on a time scale of about 5 ps, while the trajectories leading to products with four or fewer solvent molecules require about 19 ps. The origin of this difference in timescale is illustrated in Fig. 4.6, which maps out the motion of the trajectories on the a' state as a function of R_{solute}, the I_2^- bondlength, and $\Delta\Phi$, the solvent coordinate. All trajectories enter the a' state at $\Delta\Phi \approx 0$. The trajectories producing heavy fragments dissociate promptly on the a' state, Fig. 4.6(a), while trajectories with lighter products are characterized by diffusive motion on the a' state, which delays dissociation until I^* escapes via thermal evaporation, Fig. 4.6(b). A similar trapping event occurs on the A state following 790 nm excitation of I_2^- in CO_2 clusters [43, 45, 67].

For $n = 9$, the I^- + I^* products that retain 6–9 solvent molecules form in 1–5 ps. Most of the remaining trajectories are trapped for some period of time on the a' state, but, the additional CO_2 molecule allows many trajectories to reach large values of the solvent coordinate where relaxation to the lower spin-orbit manifold takes place. Figure 4.6(c) shows the location of transitions from the a' to the a and A' states. Of the trajectories that relax to the lower manifold, most dissociate to I^- + I in an average time of 19 ps, with three or fewer CO_2 molecules bound to the final I^- product, while others recombine as discussed below. Trajectories trapped in the a' state that do not undergo nonadiabatic transitions dissociate to $I^-(CO_2)_{4,5}$ + I^* in about 15 ps.

For the intermediate cluster sizes $n = 9$–12, another distinction between the rapidly dissociating and trapped trajectories becomes apparent in the early-time dynamics. As discussed in the previous section and illustrated in Fig. 4.4(c), there are two ways to make a nonadiabatic transition from the B state to the a' state: charge transfer and solvent transfer. Either the excess charge can transfer from the unsolvated to the solvated iodine atom, or the solvent can migrate to the charged iodine; these pathways are depicted by arrows 1 and 2, in Fig. 4.4(c), respectively. For trajectories that begin with a near-zero solvent coordinate it can be difficult to separate the charge and solvent motions, but for clusters with about half a solvent shell the distinction is clear. Fig-

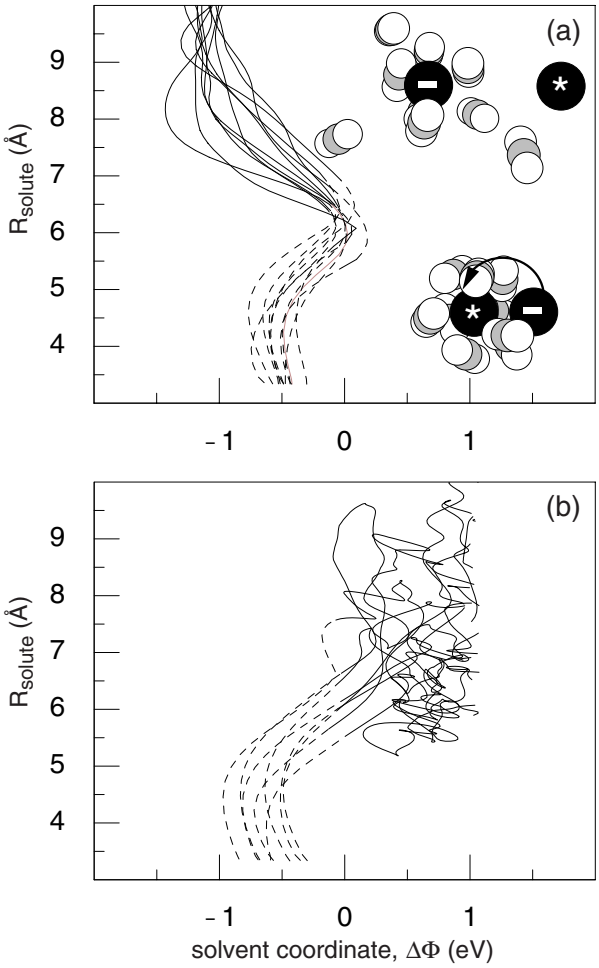

Figure 4.7: Motion on the B and a' states for selected trajectories with $n = 11$. Trajectories begin at $R_{solute} = 3.3$ Å on the B state (dashed lines) and transfer to the a' state (solid lines) near $\Delta\Phi = 0$, $R_{solute} = 5$–8 Å. (a) Charge transfer followed by direct dissociation, producing heavy I^- fragments. (b) Solvent transfer followed by transient trapping on the a' state.

ure 4.7 traces the paths of several trajectories in the $n = 11$ ensemble from excitation through the $B \rightarrow a'$ transition and the subsequent motion on the a' state. For ease of illustration, the trajectories shown all begin as solvated I^*_A + I^-_B but the overall picture is symmetric under reflection through $\Delta\Phi = 0$. As the solute dissociates on the B state, the attempted motion of I^-_B away from the solvent cluster slows the dissociation, providing time for the solvent to reorganize enough to bring about coupling between

Table 4.1: Correlation of $B \rightarrow a'$ transition type with final products. The percentage of trajectories, normalized within each product channel, that undergo charge transfer (CT) or solvent transfer (ST).

n	$I^- + I^*$ % CT	$I^- + I$ % ST	I_2^- % ST
10	68	95	100
11	90	75	88
12	89	91	78

the B and a' states. In trajectories that undergo charge transfer, shown in Fig. 4.7(a), the charge hops, forming solvated I_A^- and I_B^* escapes. Figure 4.7(b) shows trajectories crossing $\Delta\Phi = 0$ as the transfer of CO_2 molecules yields I_A^* + solvated I_B^-, trapped on the a' state. Table 4.1 shows that for intermediate cluster sizes, charge transfer from B to a' primarily results in fast dissociation on the upper spin-orbit states, while solvent transfer usually precedes spin-orbit relaxation. The following section further details the role of solvent motion in inducing relaxation to the lower spin-orbit manifold.

4.3.3 Later Times: Spin-Orbit Relaxation and Recombination

When the I_2^- solute is in its a' electronic state, asymmetric cluster configurations are favored. Figure 4.4(c) shows that increasing solvation destabilizes the a and A' electronic states, which cross the a' state at a large value of the solvent coordinate. This crossing occurs when the asymmetric solvent environment compensates for the energy gap between these electronic states in bare I_2^-, which at $R_{\mathrm{solute}} > 5$ Å is essentially the spin-orbit splitting of iodine atom, 0.94 eV. This type of mechanism was suggested, in a more speculative context, in an earlier study of the electronic structure of I_2^- in a uniform electric field [36]; there it was referred to as "field-induced resonance." In our trajectories, transitions to the lower spin-orbit manifold occur at solvent coordinates greater than 0.75 eV. Since $n = 9$ is the smallest cluster size for which such values are commonly reached on the a' state (see Fig. 4.6), this marks the onset of appreciable

spin-orbit relaxation in our simulations.

Figure 4.4 also demonstrates that a transition from the a' state to either the a or A' state involves transferring an electron between the two iodine atoms. Since electron transfer requires nonzero overlap of the wave functions on the two iodine atoms and therefore cannot occur over an arbitrarily large distance, spin-orbit relaxation is not seen in the most rapidly dissociating clusters. Trajectories that reach solvent coordinates of about 1 eV before R_{solute} exceeds about 10 Å have an opportunity to relax. If R_{solute} is larger, the a' state simply becomes lower in energy than the a and A' states, no transition occurs, and I_2^- dissociates to I^- + I^*.

If the charge transfer transition does occur, the solvent suddenly finds itself far out of equilibrium with the solute charge distribution, having acquired about 1 eV of excess potential energy. Since much of this is immediately converted to kinetic energy, the cluster virtually explodes. Some trajectories dissociate directly on the a and A' anomalous charge switching states, an event not observed in 790 nm excitation except in the smallest clusters. However, the majority of trajectories make transitions to the A and X states from the A' or a state minumum at $\Delta\Phi = 0$. These transitions occur by either charge or solvent transfer, and the two are difficult to distinguish, because the solvent coordinate remains small. If the escaping solvent molecules remove enough energy, the I_2^- bond can reform on the X state and undergo vibrational relaxation. Although we have not analyzed the final vibrational relaxation completely, we find it to be much slower than observed in 790 nm dissociation, as far fewer solvent molecules remain to dissipate energy.

Figure 4.8 shows the potential energy of the cluster in each electronic state as a trajectory progresses. To conserve space, a trajectory with faster than average relaxation dynamics is shown. States of the same charge switching character run roughly parallel to each other, since they respond similarly to changes in the solvent environment. At 250 fs this trajectory makes a $B \rightarrow a'$ transition. As the cluster reorganizes to

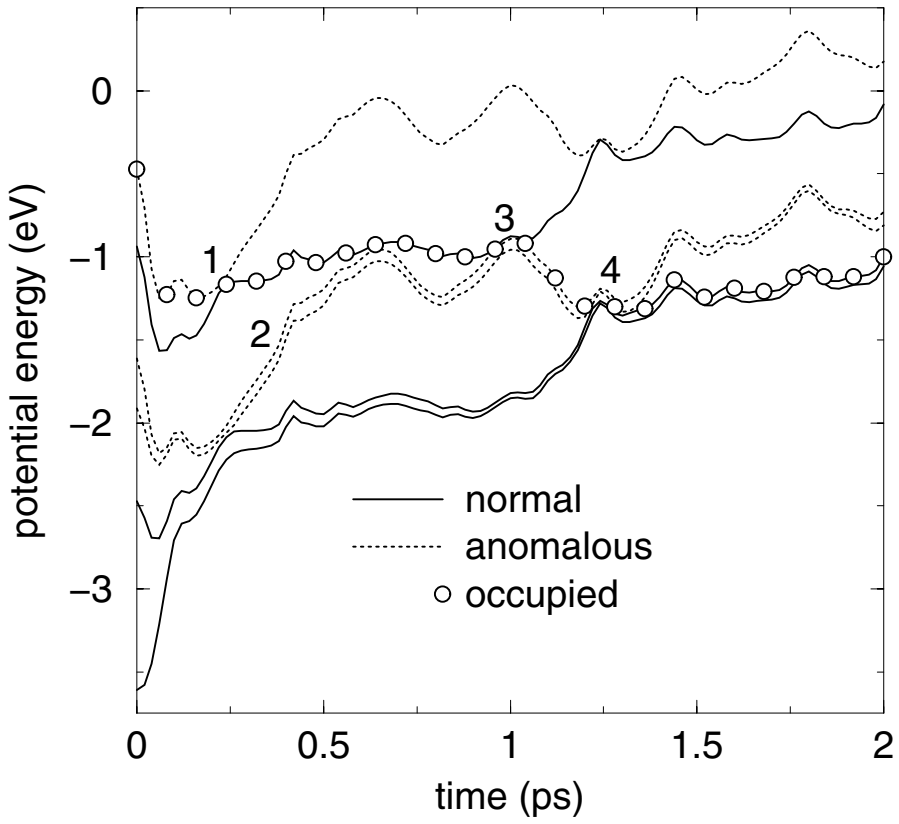

Figure 4.8: Cluster potential energy of each electronic state vs time for a single trajectory. Initially, the states are, in order of increasing energy, X, A, A', a, a', B. 1. Transition from state B to state a'. 2. Solvent reorganization, increasing cluster asymmetry, is implied by the destabilization of anomalous charge flow states. 3. Spin-orbit relaxation via charge transfer transition from state a' to state a followed by solvent reorganization. 4. Transition from state a to state A. For this trajectory, I_2^- ultimately dissociates on the A state (not shown).

a larger solvent coordinate on the a' state between 250 and 500 fs, the anomalous charge flow states are **destabilized**. At 1 ps the trajectory undergoes charge transfer to the a state, followed by a rapid reorganization of the solvent, which stabilizes the anomalous charge switching states and brings the four states of the lower spin-orbit manifold into resonance. There the trajectory hops to the A state at 1.25 ps and I_2^- dissociates.

Figure 4.9(a) displays the ensemble average of the magnitude of the solvent coordinate as a function of time for $I_2^-(CO_2)_{13}$. The ensemble is divided according to the three types of final products. Figure 4.9(b) and (c) shows the electronic state popula-

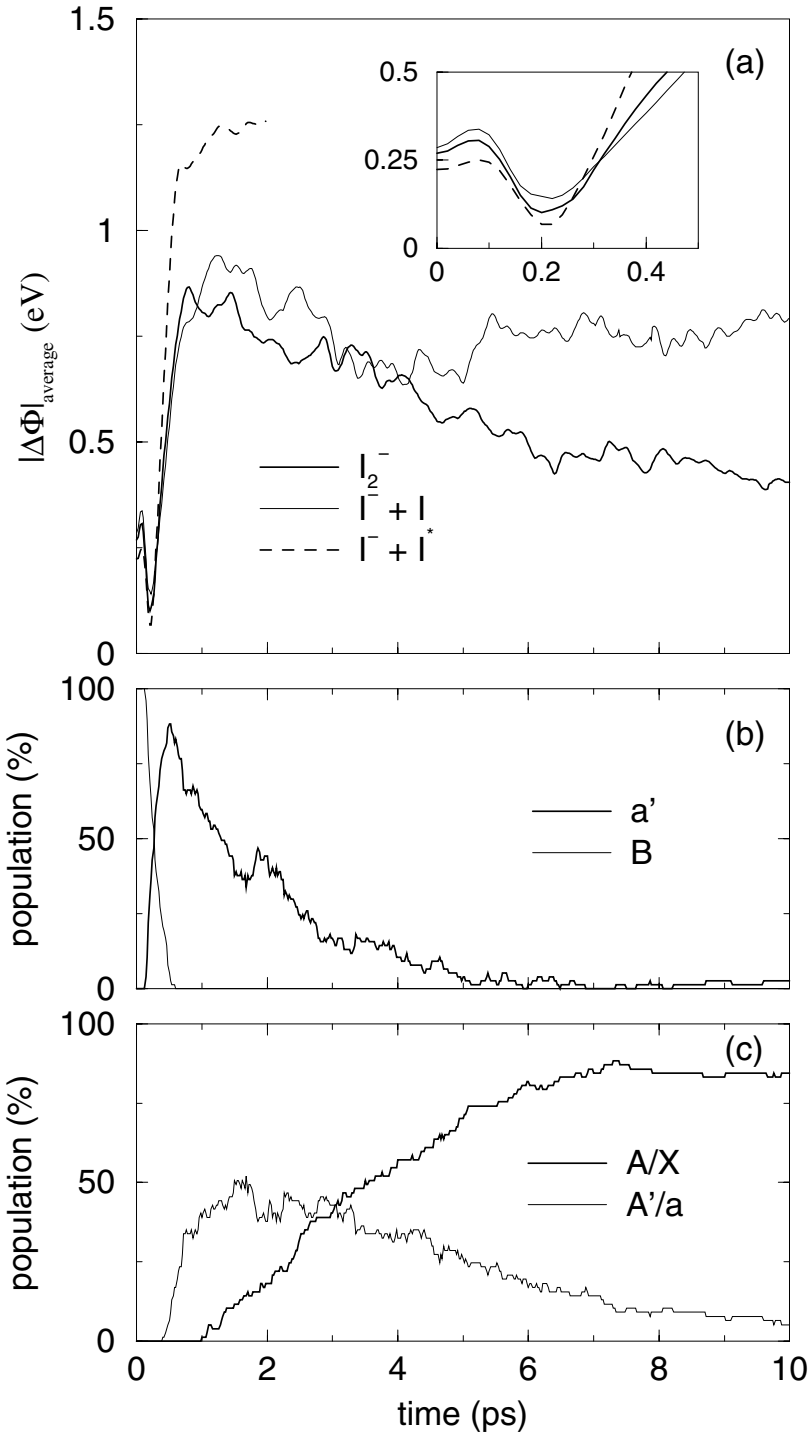

Figure 4.9: Properties of the $n = 13$ ensemble. (a) Average magnitude of the solvent coordinate vs time, sorted by product channel. (b) and (c) Electronic state populations vs time for trajectories that undergo spin-orbit relaxation. See Section 4.3.3 for further details.

tions vs. time for the same ensemble, with the trajectories that dissociate on the a' state omitted. Figure 4.9(b) shows the populations of the B and a' states, and Fig. 4.9(c) shows the population of states in the ground spin-orbit manifold grouped by charge flow character. Following excitation to the B state, all trajectories experience a slight increase in the solvent coordinate due to the increase in the I_2^- bondlength. However, immediately afterwards the solvent coordinate decreases sharply as anticipated for the anomalous B state [inset, Fig. 4.9(a)]. The sharp rise at 200 fs coincides with hopping to the a' state, where large solvent coordinates are favored. From this point the I^- + I^* products dissociate directly with the solvent coordinate increasing with R_{solute} until it reaches a maximum value. Meanwhile, between 0.5 and 3 ps the remaining trajectories begin making transitions to the a and A' states, and $|\Delta\Phi|_{\mathrm{av}}$ decreases. After 1 ps, transitions to the A and X states begin, and on these states asymmetric solvent configurations are favored. Rather than increasing, $|\Delta\Phi|_{\mathrm{av}}$ levels off, reflecting the fact that much of the solvent has evaporated from the cluster. After 5 ps the two spin-orbit relaxed products differ: the dissociative products maintain a steady value of the solvent coordinate, while the solvent coordinate of the recombined products decreases. I_2^- vibrationally relaxes on the X state by evaporating CO_2 molecules from the cluster, and for $n = 13$ all of the solvent is gone by 20 ps, forcing $\Delta\Phi$ to zero.

4.3.4 Summary

In Fig. 4.10 we revisit our qualitative picture of the potential energy of solvated I_2^- and include snapshots of trajectories to summarize the key features of the photodissociation dynamics. Within 200 fs after excitation to the B state, the I_2^- bondlength is large enough that the energy curves in this schematic diagram apply. The electronic character of state B, which localizes the charge on the unsolvated iodine atom, prevents further dissociation. Solvent reorganization towards a symmetric cluster configuration brings about transitions to the a' state. Trajectories that undergo charge transfer pre-

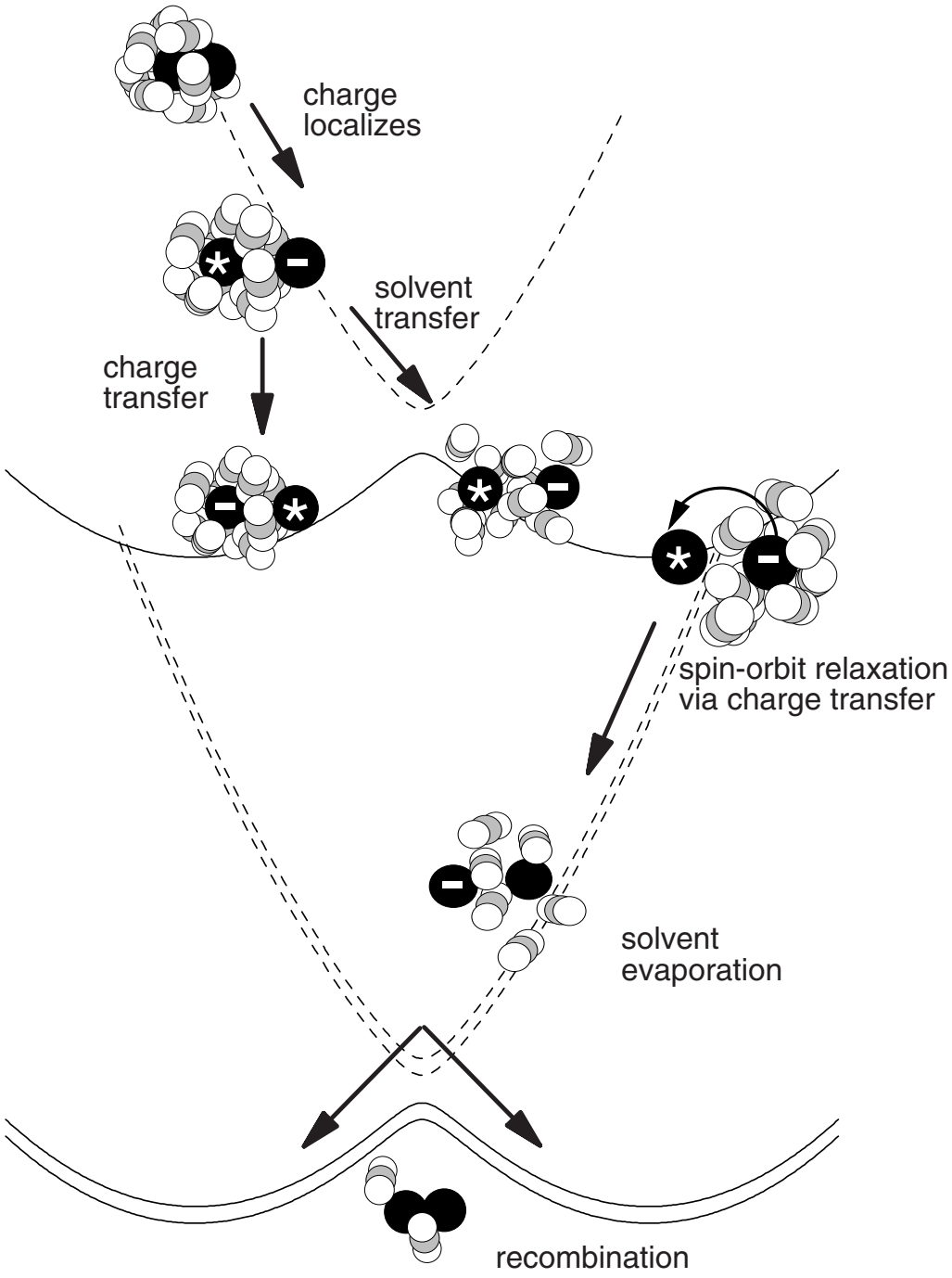

Figure 4.10: A summary of the dynamics following 395 nm photoexcitation. The schematic potential energy curves are those of Fig. 4.4, right hand panel.

dominantly dissociate to solvated I^- + I^* products within 1–5 ps, while trajectories that undergo solvent transfer become trapped temporarily on the a' state. Small clusters

remain trapped until I_2^- dissociates by evaporation of I^*. For clusters with nine or more CO_2 molecules, however, the asymmetry of the solvent distribution about I_2^- can be large enough to overcome the atomic iodine spin-orbit splitting energy that separates the a' state from the a and A' states. In these systems, we see a strong correlation between solvent transfer during the B to a' transition and subsequent return to the lower spin-orbit manifold. It appears that the early partitioning of energy into solvent motion enhances the likelihood that clusters will reach the large $|\Delta\Phi|$ required to make a nonadiabatic transition to the lower spin-orbit states before the solute bondlength becomes too large for the charge transfer that accompanies that transition to occur.

From the a' state, charge transfer to the a or A' state brings about immediate reorganization of the cluster as the spin-orbit excitation energy is converted into solvent motion. In fact, much of the solvent boils off at this point, and it is even possible for dissociation of I_2^- to occur on these anomalous states. As the solvent coordinate returns to zero during this process of energy dissipation, transitions to the A and X states occur, typically within a few hundred femtoseconds of the transition out of the a' state. From this point, trajectories may continue to dissociate, or they may recombine on the X state of I_2^-.

4.4 Conclusions

The results of these simulations demonstrate that our effective Hamiltonian model adequately describes the overall trends in the experimental product branching ratio and the mass distribution of photofragments. While the quantitative agreement between theory and experiment is not as good as in our previous simulations of 790 nm dissociation [43], the principal new feature seen in UV photodissociation — the onset of extensive spin-orbit quenching in the larger clusters — is well reproduced. In fact, the first indications that spin-orbit quenching could be efficient in these clusters came from the simulations, which preceded the experiments by several months. While the

time scales for these processes have not yet been determined experimentally in the CO_2 clusters, the recombination time in OCS clusters is estimated to be on the order of tens of picoseconds [51], consistent with our results.

Our results reinforce the lessons we have learned from previous work. A proper interpretation of the experiments and simulations requires an understanding of the interplay between the solute charge distribution and the solvent environment. These interactions depend strongly on the various electronic states of the solute as well as on the dissociation coordinate, R_{solute}, and thus interpretations based solely on the isolated solute potential curves can be misleading. Just as we found for 790 nm excitation to the A' state, the anomalous charge flow character of the B state prevents dissociation when strong solute-solvent interactions are present. A nonadiabatic transition to a state exhibiting normal charge flow is necessary for dissociation to continue. Strong interactions with the solvent also affect dynamics on normal charge flow states by creating a competition between solvation and chemical bonding, as evidenced by the trapping of trajectories on the a' state. This too parallels behavior observed in the near-IR studies, but there is one important distinction between transient trapping on the a' and A states. To leave the A state, the solute bondlength must increase well beyond the equilibrium value, but on the a' state I_2^- can electronically relax via solvent-mediated charge transfer, providing that the solvation energy is greater than the spin-orbit splitting. This relaxation occurs at the shorter solute bondlengths characteristic of the trapped clusters, and the requisite solvent coordinate is readily attained in clusters with more than half a solvation shell of CO_2. Therefore, both electronic relaxation (spin-orbit quenching) and thermal evaporation of neutral iodine deplete the number of clusters trapped on the a' state. The two processes occur on comparable timescales in our simulations, however, electronic relaxation becomes more efficient as cluster size increases.

Analysis of the simulation trajectories using an extension of the electron-transfer picture described in our earlier work strongly suggests that the observed electronic re-

laxation occurs via charge transfer from solvated I^- to I^*, this process being made resonant, and thereby efficient, by reorganization of the solvent following the initial UV excitation. The charge transfer event converts electronic energy into solvent potential energy, which is dissipated by further solvent rearrangment and evaporation. As a result, the spin-orbit excitation energy is efficiently quenched within the cluster. This mechanism provides an appealing explanation for the sharp onset of spin-orbit quenching with increasing cluster size observed in both simulations and experiments.

References for Chapter 4

[1] M. Alexander, N. Levinger, M. Johnson, D. Ray, and W. C. Lineberger, J. Chem. Phys. **88**, 6200 (1988).

[2] D. Ray, N. Levinger, J. Papanikolas, and W. C. Lineberger, J. Chem. Phys. **91**, 6533 (1989).

[3] J. Papanikolas, J. Gord, N. Levinger, D. Ray, V. Vorsa, and W. C. Lineberger, J. Phys. Chem. **95**, 8028 (1991).

[4] J. Papanikolas, V. Vorsa, M. Nadal, P. Campagnola, J. Gord, and W. C. Lineberger, J. Chem. Phys. **97**, 7002 (1992).

[5] J. Papanikolas, V. Vorsa, M. Nadal, P. Campagnola, H. Buchenau, and W. C. Lineberger, J. Chem. Phys. **99**, 8733 (1993).

[6] V. Vorsa, S. Nandi, P. J. Campagnola, M. Larsson, and W. C. Lineberger, J. Chem. Phys. **106**, 1402 (1997).

[7] S. Nandi, A. Sanov, N. Delaney, J. Faeder, R. Parson, and W. C. Lineberger, J. Phys. Chem. A **102**, 8827 (1998).

[8] B. J. Greenblatt, M. T. Zanni, and D. M. Neumark, Chem. Phys. Lett. **258**, 523 (1996).

[9] B. J. Greenblatt, M. T. Zanni, and D. M. Neumark, Science **276**, 1675 (1997).

[10] M. T. Zanni, T. R. Taylor, B. J. Greenblatt, B. Soep, and D. M. Neumark, J. Chem. Phys. **107**, 7613 (1997).

[11] B. J. Greenblatt, M. T. Zanni, and D. M. Neumark, Faraday Discuss. **108**, 101 (1997).

[12] K. R. Asmis, T. R. Taylor, C. S. Xu, and D. M. Neumark, J. Chem. Phys. **109** (1998).

[13] A. E. Johnson, N. E. Levinger, and P. F. Barbara, J. Phys. Chem. **96**, 7841 (1992).

[14] J. Alfano, Y. Kimura, P. K. Walhout, and P. F. Barbara, Chem. Phys. **175**, 147 (1993).

[15] D. A. V. Kliner, J. C. Alfano, and P. F. Barbara, J. Chem. Phys. **98**, 5375 (1993).

[16] P. K. Walhout, J. C. Alfano, K. A. M. Thakur, and P. F. Barbara, J. Phys. Chem. **99**, 7568 (1995).

[17] U. Banin, A. Waldman, and S. Ruhman, J. Chem. Phys. **96**, 2416 (1992).

[18] U. Banin and S. Ruhman, J. Chem. Phys. **98**, 4391 (1993).

[19] U. Banin and S. Ruhman, J. Chem. Phys. **99**, 9318 (1993).

[20] U. Banin, R. Kosloff, and S. Ruhman, Chem. Phys. **183**, 289 (1994).

[21] E. Gershgoren, U. Banin, and S. Ruhman, J. Phys. Chem. A **102**, 9 (1998).

[22] H. Yasumatsu, S. Koizumi, A. Terasaki, and T. Kondow, J. Chem. Phys. **105**, 9509 (1996).

[23] H. Yasumatsu, A. Terasaki, and T. Kondow, J. Chem. Phys. **106**, 3806 (1997).

[24] H. Yasumatsu, U. Kalmbach, S. Koizumi, A. Terasaki, and T. Kondow, Z. Phys. D **40**, 51 (1997).

[25] H. Yasumatsu, S. Koizumi, A. Terasaki, and T. Kondow, J. Phys. Chem. A **102** (1998), in press.

[26] L. Perera and F. G. Amar, J. Chem. Phys. **90**, 7354 (1989).

[27] F. G. Amar and L. Perera, Z. Phys. D **20**, 173 (1991).

[28] I. Benjamin and R. M. Whitnell, Chem. Phys. Lett. **204**, 45 (1993).

[29] I. Benjamin, U. Banin, and S. Ruhman, J. Chem. Phys. **98**, 8337 (1993).

[30] U. Banin, A. Bartana, S. Ruhman, and R. Kosloff, J. Chem. Phys. **101**, 8461 (1994).

[31] G. Ashkenazi, U. Banin, A. Bartana, R. Kosloff, and S. Ruhman, Adv. Chem. Phys. **100**, 317 (1997).

[32] B. J. Gertner, K. Ando, R. Bianco, and J. T. Hynes, Chem. Phys. **183**, 309 (1994).

[33] R. Bianco and J. T. Hynes, J. Chem. Phys. **102**, 7864 (1995).

[34] R. Bianco and J. T. Hynes, J. Chem. Phys. **102**, 7885 (1995).

[35] I. Benjamin, P. F. Barbara, B. J. Gertner, and J. T. Hynes, J. Phys. Chem. **99**, 7557 (1995).

[36] P. E. Maslen, J. M. Papanikolas, J. Faeder, R. Parson, and S. V. ONeil, J. Chem. Phys. **101**, 5731 (1994).

[37] J. M. Papanikolas, P. E. Maslen, and R. Parson, J. Chem. Phys. **102**, 2452 (1995).

[38] B. M. Ladanyi and R. Parson, J. Chem. Phys. **107**, 9326 (1997).

[39] J. G. Dojahn, E. C. M. Chen, and W. E. Wentworth, J. Phys. Chem. **100**, 9649 (1996).

[40] E. C. M. Chen, J. G. Dojahn, and W. E. Wentworth, J. Phys. Chem. A **101**, 3088 (1997).

[41] V. S. Batista and D. F. Coker, J. Chem. Phys. **106**, 7102 (1997).

[42] J. Faeder, N. Delaney, P. Maslen, and R. Parson, Chem. Phys. Lett. **270**, 196 (1997).

[43] N. Delaney, J. Faeder, P. E. Maslen, and R. Parson, J. Phys. Chem. A **101**, 8147 (1997).

[44] P. E. Maslen, J. Faeder, and R. Parson, Mol. Phys. **94**, 693 (1998).

[45] J. Faeder, N. Delaney, P. Maslen, and R. Parson, Chem. Phys. **239**, 525 (1998).

[46] C. Margulis and D. F. Coker, J. Chem. Phys. **110**, 5677 (1999).

[47] J. Faeder and R. Parson, J. Chem. Phys. **108**, 3909 (1998).

[48] R. A. Marcus, Ann. Rev. Phys. Chem. **15**, 155 (1964).

[49] M. D. Newton and N. Sutin, Ann. Rev. Phys. Chem. **35**, 437 (1984).

[50] G. C. Schatz and M. A. Ratner, Quantum Mechanics in Chemistry, chapter 10, Prentice Hall, Englewood Cliffs, 1993.

[51] A. Sanov, T. Sanford, S. Nandi, and W. C. Lineberger, J. Chem. Phys. **111**, 663 (1999).

[52] D. Husain and R. J. Donovan, Electronically excited halogen atoms, in Advances in Photochemistry, edited by J. N. Pitts, Jr, G. S. Hammond, and W. A. Noyes, Jr, volume 8, pp. 1–75, Wiley-Interscience, New York, 1971.

[53] A. V. Benderskii, R. Zadoyan, and V. A. Apkarian, J. Chem. Phys. **107**, 8437 (1997).

[54] R. Zadoyan, M. Sterling, M. Ovchinnikov, and V. A. Apkarian, J. Chem. Phys. **107**, 8446 (1997).

[55] P. E. Maslen, J. Faeder, and R. Parson, Chem. Phys. Lett. **263**, 63 (1996).

[56] C. S. Murthy, S. F. O'Shea, and I. R. McDonald, Mol. Phys. **50**, 531 (1983).

[57] C. G. Gray and K. E. Gubbins, Theory of Molecular Fluids, volume 1, Clarendon, Oxford, 1984.

[58] A. J. Stone, The Theory of Intermolecular Forces, Oxford, New York, 1996.

[59] Y. Zhao, C. C. Arnold, and D. M. Neumark, J. Chem. Soc. Faraday Trans. **89**, 1449 (1993).

[60] H. C. Andersen, J. Comput. Phys. **52**, 24 (1982).

[61] J. C. Tully, J. Chem. Phys. **93**, 1061 (1990).

[62] S. Hammes-Schiffer and J. C. Tully, J. Chem. Phys. **101**, 4657 (1994).

[63] J. M. Papanikolas, I_2^- Photodissociation and Cage Recombination Dynamics in Size-Selected $I_2^-(CO_2)_n$ Clusters, PhD thesis, University of Colorado, 1994.

[64] V. Vorsa, P. J. Campagnola, S. Nandi, M. Larsson, and W. C. Lineberger, J. Chem. Phys. **105**, 2298 (1996).

[65] These are not, strictly speaking, true adiabatic curves because they cross at large solvent coordinate. In the true adiabats these crossings would be avoided. The curves in Fig. 4 correspond instead to an intermediate representation which exactly diagonalizes the electronic Hamiltonian only at $\Delta\Phi = 0$. This is more convenient that the true adiabatic representation, which diagonalizes the electronic Hamiltonian for all $\Delta\Phi$, because the curves can be labelled with the molecular state labels of isolated I_2^-.

[66] It is possible, but rarely observed in the simulations ($< 1\%$ of trajectories), for direct dissociation on the B state to occur, producing a light I^- fragment and solvated I^*, analogous to the A' state, low mass dissociative products reported for $I_2^-Ar_n$ clusters [6].

[67] B. J. Greenblatt, M. T. Zanni, and D. M. Neumark, private communication.

Chapter 5

Photodissociation and recombination of solvated I_2^-: What causes the transient absorption peak?

Seven years ago, Lineberger and co-workers observed evidence of coherent nuclear motion in the photodissociation and recombination of I_2^- clustered with CO_2 [1–3]. In their experiment, a 720 nm pulse excites the I_2^- chromophore to its repulsive A' state (Fig. 5.1). Dissociation of the chromophore makes the cluster transparent, allowing recombination to be monitored with a subsequent 720 nm probe pulse. Assuming that the excited clusters dispose of their excess energy by evaporation, the mass spectrum of the ionic photofragments enables one to identify those clusters which have absorbed both pulses. By measuring the intensity of this two-photon product channel as a function of time delay between pump and probe, Lineberger and co-workers determined the overall time scale for dissociation, recombination, and vibrational relaxation of the solvated ion. The most striking result of these experiments was a transient peak in the absorption recovery at about 2 ps after excitation, which was attributed to the coherent passage of recombining chromophores through a region of the potential surface characterized by strong absorption. A similar feature has been seen in the dissociation and recombination of I_2^- in liquid solutions [4, 5].

These experiments have stimulated an intensive program of research into the dynamics of I_2^- photodissociation and recombination. Pump-probe experiments have now been carried out on a variety of clusters [6, 7] as well as liquid solutions [4, 5, 8, 9].

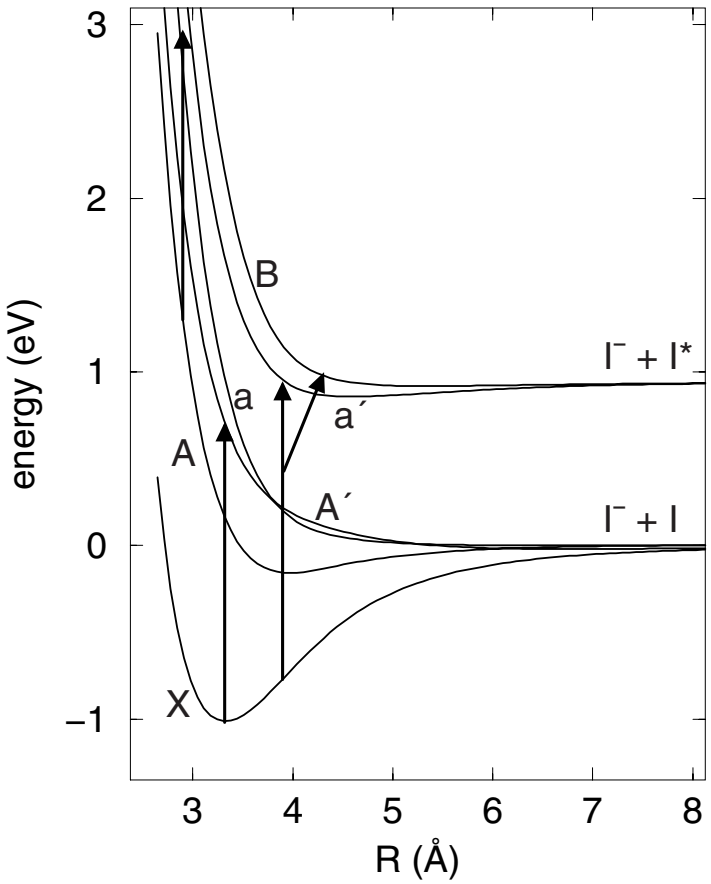

Figure 5.1: Scaled **ab initio** gas phase potential curves for I_2^-. Arrows mark the 720 nm pump absorption ($X \rightarrow A'$), our assignment of the transient absorption peak at 2 ps ($X \rightarrow a', B$) and a previous assignment for the same ($A \rightarrow a$).

Measurements of the absorption recovery in particular mass channels [10] have yielded information about the dynamics of the solvent cage during the recombination process. Femtosecond time-resolved photoelectron spectra (FPES) [11, 12] have provided complementary insights into the mechanisms of recombination and relaxation in these systems. Finally, nonadiabatic molecular dynamics simulations have successfully reproduced the experimental product distributions [13–16], time-resolved photoelectron spectra [17], and the overall absorption recovery [18], and have led to a detailed molecular picture of the dynamics.

A crucial element is missing from the picture, however: the mechanism that gives

rise to the 2 ps transient peak in the absorption recovery has never been conclusively identified. Lineberger and co-workers originally ascribed it to absorption from the inner wall of the weakly bound A state to the higher-lying a state (Fig. 5.1). This assignment is consistent with the polarization dependence of the signal, which shows that the associated transition moment is parallel to the internuclear axis, and with the solution-phase experiments, which found that the transient disappeared when the system was probed with UV radiation [5]. The FPES experiments [12] and the simulations [15, 16, 18] did find significant A-state recombination, but in the simulations the A-state dynamics was observed to be diffusive rather than coherent, and the trajectories did not appear to find regions where the $A \rightarrow a$ transition might be resonant with the probe. Instead, the simulations found that a significant fraction of the ensemble recombined in the **ground** state on this time scale. This suggests that the transient might be due to ground-state absorption, but this could not be demonstrated directly since the simulation statistics were not sufficient to resolve the finer structures in the absorption recovery [18].

In this Chapter we present new simulation results which, we believe, settle this issue. By using a much larger number of trajectories than earlier studies, we are able to resolve the 2 ps transient in the absorption recovery and to show that it is due to transitions from the ground state to the **spin-orbit excited** B and a' states of I_2^-. The absorption occurs at large internuclear distances ($R > 3.7$ Å), as the fragments first recombine, not at the inner turning point. This possibility was considered by Papanikolas et al. [2, 3], but tentatively ruled out because it requires that the spin-orbit energy be efficiently converted into thermal energy of the cluster in order to yield the observed two-photon fragments. The subsequent experimental [7, 19] and theoretical [20] demonstration that spin-orbit quenching is actually extremely efficient in these systems, occurring on a time scale of a few ps, removes this objection. Our new assignment is consistent with the parallel probe transition moment observed in the clusters, and with the absence of a 2 ps transient in the UV probe absorption. Analysis of the simulations

using an electron-transfer perspective described in previous work [15, 16, 20] shows that solvent-induced perturbations of the solute electronic structure play a crucial role in determining the regions of strong absorption. We also report on the simulated absorption recovery of $I_2^-Ar_{20}$ which shows a prominent transient feature not observed in the experiments [6]. To investigate this apparent discrepency we consider the UV photodissociation of $I_2^-Ar_n$ clusters. Ultimately, we are forced to reevaluate key assumptions made in interpreting the experiments.

5.1 Methods

The simulations are based on the effective Hamiltonian discussed in Chapter 2. The interaction between the I_2^- solute and the rigid CO_2 solvent molecules is represented by an operator that includes state-dependent electrostatic and induction interactions based on **ab initio** calculations of the solute electronic structure [21] and experimental data for the solvent charge distribution and polarizability. The one-electron density matrix derived from the solute wave functions is expanded in distributed multipole operators [22]. Diagonal elements of these operators describe the solute charge density in various electronic states, while off-diagonal elements describe transition charge densities that allow the solvent to polarize the solute charge density. In the present application these distributed transition moments are also used to assemble the transition dipole matrix elements that determine the optical absorption intensities. State-independent atom-atom Lennard-Jones potentials, fit to reproduce known I^-–CO_2 and I–CO_2 potential curves [23], account for the dispersion and repulsion interactions between solute and solvent, while the CO_2–CO_2 interaction potential is taken from Murthy et al. [24]. The overall model captures the sensitive dependence of the solute charge distribution on the solute electronic state, the solute bond length, and the positions and orientations of the solvent molecules. At each trajectory time step the Hamiltonian matrix, which depends parametrically upon the coordinates of all the solute and solvent nuclei, is

constructed and diagonalized, yielding the energies, forces, and nonadiabatic transition probabilities required to proceed to the next step. Nuclear motion on a single adiabatic potential surface is computed using the velocity version of the Verlet algorithm [25, 26], while hopping between surfaces is computed using a modified version [16] of Tully's MDQT method [27, 28].

The absorption recovery signal is calculated using the quasiclassical prescription of Coker and coworkers [18, 29]. Along each trajectory, a contribution to the probe absorption is recorded when the energy gap between the occupied state and a higher-lying state falls within a Gaussian window around the probe frequency; these contributions are weighted by the square of the transition dipole moment connecting these states. This signal is given by

$$S(t) \sim \frac{1}{N} \sum_{k=1}^{N} \sum_{f} |\mu_{fj_k}[\mathbf{R}_k(t)]|^2 \times \exp[-\frac{\{\Delta E_{fj_k}[\mathbf{R}_k(t)] - h\nu_{\mathrm{probe}}\}^2}{2\sigma_E^2}]. \qquad (5.1)$$

In this expression, N is the number of trajectories, $\mu_{fj_k}[\mathbf{R}_k(t)]$ is the transition dipole matrix element between states i and f at the current nuclear configuration, $\mathbf{R}_k(t)$, and $\Delta E_{fj_k}[\mathbf{R}_k(t)]$ is the energy gap between the initial and final states. This signal is convoluted with a Gaussian pulse in time to model the finite duration of the pump pulse. The final expression for the absorption recovery signal is

$$I(t) \approx \int_{-\infty}^{\infty} dt' \exp[-\frac{\{t - t'\}^2}{2\sigma_t^2}] S(t'). \qquad (5.2)$$

In the results reported here the time width $\sigma_t = 150$ fs, consistent with the experimental value of ≈120 fs [2], and the energy width $\sigma_E = 0.005$ a.u.. While this is larger than the value $\sigma_E = 0.001$ a.u., derived from the spectral bandwidth in the femtosecond experiments of Papanikolas et al., we find that varying σ_E from 0.0001 a.u. to 0.005 a.u. has only minor effects on the essential spectral features. The larger value effectively smooths the simulated absorption signal.

Simulating the pump-probe signal required much larger trajectory ensembles

than our earlier study of the final product distributions [15], because only a small portion of the ensemble contributes to the absorption signal in a particular time window. For each cluster size studied, 250 trajectories were computed from starting configurations obtained by sampling a single 2.5 ns trajectory with an average temperature of 80 K. The dissociation and recombination times vary from a few picoseconds to over 75 ps in some cases where I_2^- is temporarily trapped in an excited electronic state. Since we are primarily interested in short time dynamics most of the simulations were terminated at 20 ps, although we did run one ensemble of 100 trajectories out to 100 ps in order to establish the asymptotic behavior. To compensate for the smaller size of this ensemble, the time width, σ_t, was increased to 300 fs.

5.2 Results and Discussion

5.2.1 $I_2^-(CO_2)_{16}$

In Fig. 5.2 we compare our simulated absorption recovery signal with the experiments of Papanikolas et al. [2, 30]. The simulation clearly reproduces the transient absorption feature at 2 ps. We have found the transient in two separate 250-trajectory simulations of $I_2^-(CO_2)_{16}$ photodissociated at 720 nm, in a simulation using a lower pump frequency (790 nm), and in simulations of I_2^- clustered with 10, 12, and 14 CO_2 molecules. The intensity of the 2 ps bump relative to the overall absorption recovery is lower in the simulation than in the experiment, but this is hard to interpret since the measured two-photon product signal depends on photofragment branching ratios as well as the transition moments for probe absorption; for now we make only qualitative comparisons.

While the short-time dynamics is well reproduced, Fig. 5.2(a) shows that at longer times the absorption recovery is significantly slower in the simulations than in the experiment. Margulis and Coker found a similar discrepancy in their simula-

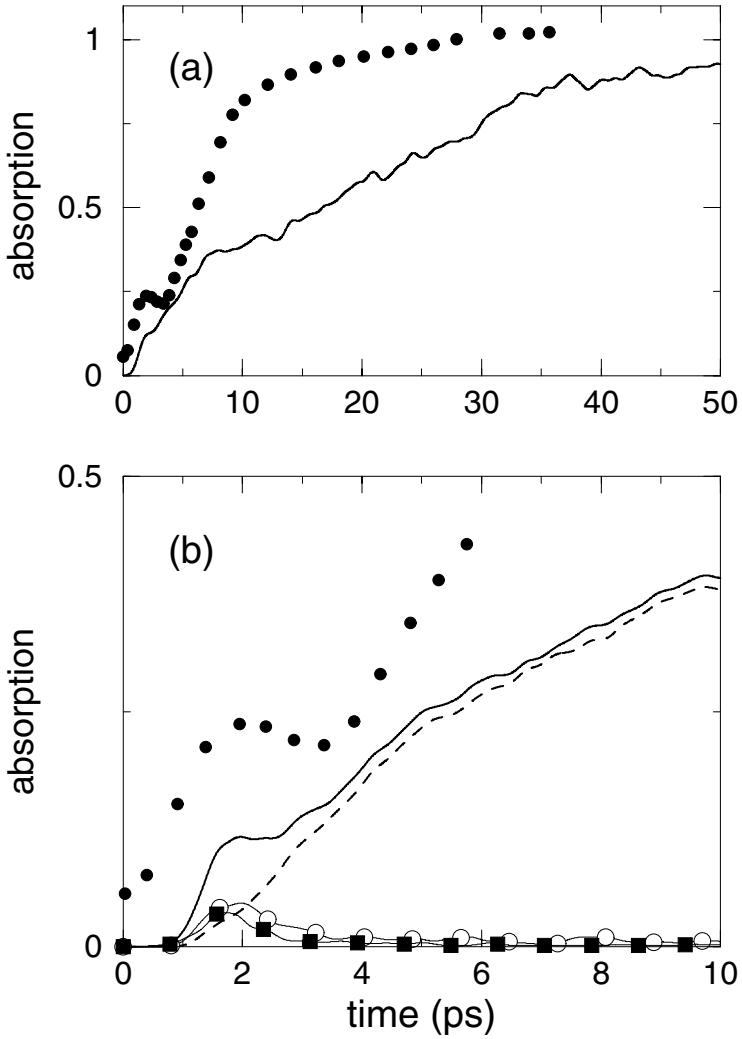

Figure 5.2: Aborption recovery of $I_2^-CO_{16}$ (a) Comparison of experimental (dots) and simulated (line) signals. Simulated signal is from 100-trajectory ensemble and reaches it's asymptotic value between 60 and 80 ps. (b) Solid line is the total simulated signal from a 250-trajectory ensemble, dots are the experimental data. Dashed line is the contribution from the $X \rightarrow A'$ transition. The transient feature at 2 ps is due to $X \rightarrow a'$ and $X \rightarrow B$ transitions, shown respectively by the open circles and filled squares.

tion [18], and attributed it to trajectories that become trapped in the intermediate A state for long times before relaxing to the ground state. A-state trapping was also seen in our own previous study [16], in which we calculated the time-dependent state populations but not the absorption recovery. While the FPES experiments of Neumark and coworkers provide evidence that A-state recombination does indeed occur [12], the associated

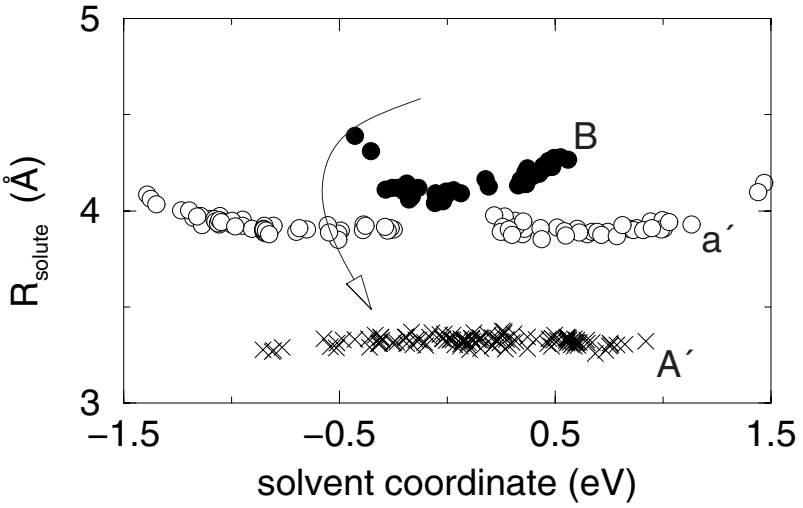

Figure 5.3: Location of strong, 720 nm absorption regions in the (R, $\Delta\Phi$) plane. Transitions originate on the X state and end on the A' (x's), a' (open circles), and B (filled circles) states. Arrow represents simplified pathway for trajectories recombining on the X state.

spectral features disappear in a few ps, implying that both simulations underestimate the rate of $A \rightarrow X$ electronic quenching. Since the two simulation models are constructed in very different ways, we infer that the disagreement with experiment is due to some physical approximation common to both, such as the neglect of intramolecular CO_2 vibrations, rather than to incidental details of the potentials.

In Fig. 5.2(b) we decompose the total absorption according to the initial and final states involved in the transitions. While the overall rise is dominated by absorption from the ground state to the A' excited state (i.e. the same transition that initially dissociated the molecule), the 2 ps transient is entirely due to transitions from the ground state to the a' and B excited states, which correlate to spin-orbit excited iodine (I^*). Although the A state is populated, transitions originating on this state make a negligible contribution to the signal, because trajectories on the A state never find regions where such transitions would be resonant with the 720 nm probe, as will be discussed below.

To further elucidate the origin of the 2 ps peak, we map the trajectories using two coordinates: R, the solute bondlength, and $\Delta\Phi$, a collective solvent coordinate defined

as the change in energy when a unit charge is moved from one I atom to the other holding all nuclear coordinates fixed. The magnitude of $\Delta\Phi$ is small for symmetric solvent configurations around the solute, and large for asymmetric configurations in which one I atom is preferentially solvated. We monitor R and $\Delta\Phi$ along the simulation trajectories and record those points for which the contribution of the trajectory to the probe absorption exceeds a threshold value. The resulting plot, Fig. 5.3, displays the solute and solvent configurations that give rise to the various components of the probe absorption. The $X \rightarrow A'$ transitions occur primarily near the equilibrium bond distance, confirming the previously accepted conclusion that the overall absorption recovery is due to recombination followed by vibrational relaxation on the ground state [2, 4]. The transitions to the spin-orbit excited a' and B states occur at larger internuclear distances, as I_2^- recombines.

The markedly different shapes of the high intensity regions mapped out by the $X \rightarrow a'$ and $X \rightarrow B$ transitions reflect the strong dependence of the corresponding state energies on the solvent coordinate [7, 15, 16, 20]. Since the X and a' states both have ungerade symmetry in the isolated molecule, the $X \rightarrow a'$ transition is forbidden at $\Delta\Phi = 0$ but becomes allowed in highly asymmetric solvent environments. The $X \rightarrow B$ transition, in contrast, is strongest in symmetric environments. The X and a' states are stabilized by solvent asymmetry, so that at fixed R the energy gap between these states depends weakly on $\Delta\Phi$. In contrast, the B state is destabilized in an asymmetric cluster, so that the energy of this state increases with $\Delta\Phi$. Since the X and B state energies move in opposite directions as $\Delta\Phi$ increases away from zero, the energy gap between these states depends strongly on $\Delta\Phi$ at fixed R, so that it is necessary to vary both R and $\Delta\Phi$ in order to keep the gap constant. This leads to the highly curved profile mapped out by the $X \rightarrow B$ transition.

Prior to this study, the 2 ps feature had been attributed to absorption from the inner turning point on the A state to the a state. The semi-empirical potential curves

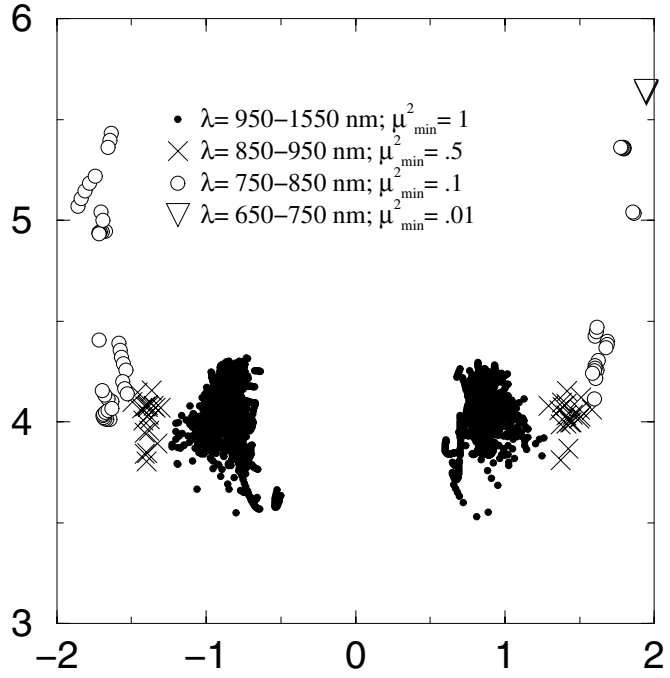

Figure 5.4: Map of $A \rightarrow a$ transitions centered at wavelengths from 700–1500 nm. Note that transition intensity is diminished at the smaller wavelengths.

available for I_2^- at that time [31] indicated that the transition would be resonant with 720 nm at a solute bondlength just slightly smaller than the equilibrium bondlength for the A state. However, more recent **ab initio** calculations from our group [21] and experiments by Neumark and co-workers [32] have produced more accurate I_2^- gas phase potentials. On the calculated surfaces shown in Fig. 5.1, the $A \rightarrow a$ energy gap is 1.72 eV at $R_{\mathrm{solute}} \approx 2.9$ Å. This point is so far up the A state repulsive wall that it is higher in energy than the asymptote of the upper spin-orbit manifold. Furthermore, simulations of the photodissociation dynamics show that motion on the A state is diffusive rather than coherent and so we do not expect the A state population to give rise to a distinct peak in the probe absorption.

As noted repeatedly in this study, the gas phase curves, alone, cannot be used to rule out a mechanism, since the solvent configuration profoundly alters the I_2^- potentials. In this particular case, the effect of solvent asymmetry is dramatic because the A

and a states exhibit opposite charge flow character. In the vicinity of the A state well ($R_{\mathrm{solute}} \approx 4$ Å), the energy gap between the A and a states varies from about 350 meV at zero solvent coordinate to 1.55 eV at $|\Delta\Phi| = 1.75$ eV. This is illustrated in Fig. 5.4, which plots the points at which trajectories on the A state pass through regions which are above a threshold absorption strength to the a state, analogous to Fig. 5.3. A range of probe wavelengths, from 700 nm (1.77 eV) to 1500 nm (0.83 eV), are shown. The only transitions comparable in strength to the $X \rightarrow A'$ (pump) transition are at wavelengths greater than 1000 nm. For shorter wavelengths, a lower threshold value of μ^2 is used to uncover where these resonances occur. Transitions with $\lambda = 700 \pm 50$ nm are at least two orders of magnitude lower in intensity than the $X \rightarrow A'$ transitions and occur only at the most extreme solvent coordinates accessed in the simulations ($|\Delta\Phi| \geq 2$ eV). In principle, there is a horseshoe shaped region of resonance with 720 nm, however, these areas of the potential curves are not energetically accessible.

5.2.2 Cluster-Size Dependence

Figure 5.5(a) shows the total simulated 720 nm absorption recovery signals for $I_2^-(CO_2)_{n=10,12,14,16}$. As in the experiment, intermediate cluster sizes show multiple relaxation timescales, and for $n \geq 13$ a shoulder in the absorption signal develops into a transient peak at about 2 ps. Figure 5.5(b) shows the same signal separated into contributions from the $X \rightarrow A'$ and $X \rightarrow (a',B)$ transitions. For $n = 14$ and 16, the transient peak, due to $X \rightarrow (a',B)$ transitions, is mostly localized at 2 ps, where the contributions from the $X \rightarrow A'$ transition are very small. For the smaller cluster sizes, the transient peak is spread out over a longer time period and overlaps with contributions from the $X \rightarrow A'$ transition. The net result is a less distinct transient feature, however the integrated intensity of the transient peak from $n = 10$ is more than twice that from $n = 16$, see Table 5.1.

A factor affecting the intensity of the transient peak is the amount of time the

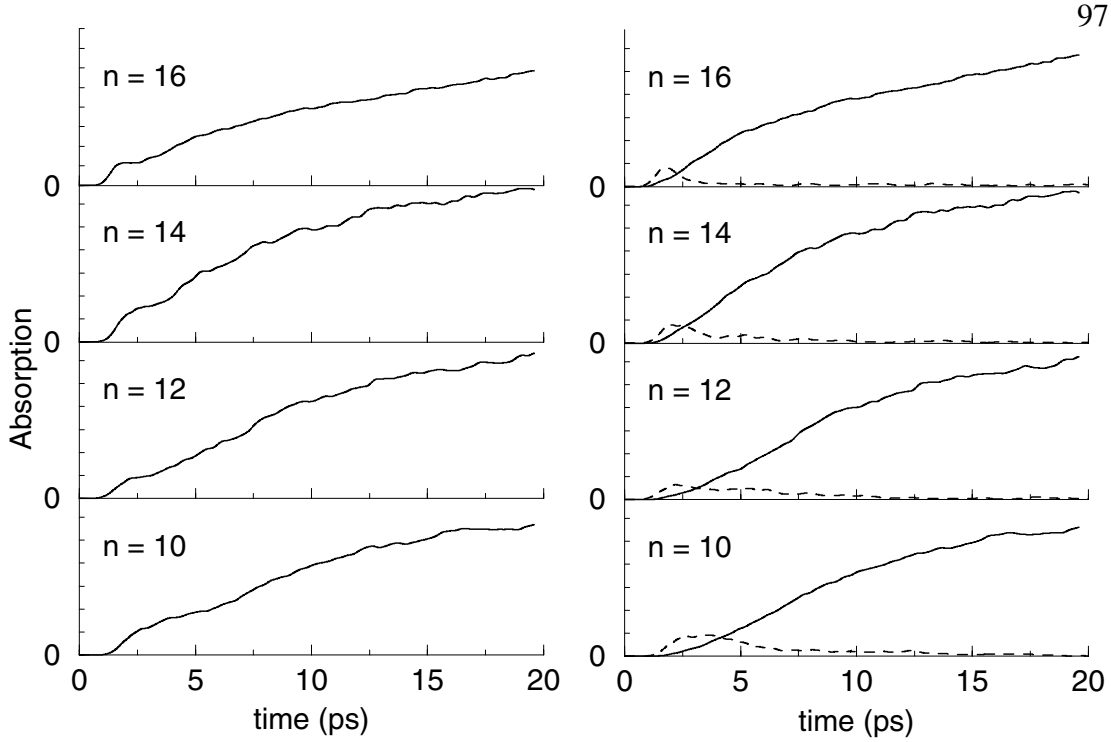

Figure 5.5: Simulated absorption recovery signals for $I_2^-(CO_2)_n$ clusters. (a) Total signal. (b) Decomposed by final spin-orbit state, solid line: A', dashed line: a' and B.

clusters spend in the absorption window. Since the transitions to the spin-orbit excited states take place only at solute bondlengths greater than 3.75Å, the rate of vibrational relaxation on the ground electronic state, which is dependent on the cluster size, will in part determine the prominence of the transient peak. The average solute bondlength versus time for cluster sizes $n = 10$ and 16 is shown in Fig. 5.6. Since we wish to focus on the vibrational relaxation process, we subtract off the time required for electronic relaxation by resetting the time origin for each trajectory such that $t_0 = t_{recombination}$. At $t = 0$ on this plot, each trajectory has just passed through the absorption window. Trajectories from the $n = 10$ ensemble return to this region at least two additional times, while trajectories from the $n = 16$ ensemble relax below the threshold bondlength sooner.

The strength of the transition dipole also depends on the solvent coordinate as

Table 5.1: Integrated intensity of transient peak vs. n

n	Intensity
10	2.1
12	1.7
14	1.3
16	1

shown in Fig. 5.3. We find that the larger the cluster, the more rapidly the solvent asymmetry decreases following recombination. For trajectories in the $n = 16$ ensemble, the solvent coordinate is nearly zero after the first compression of the I_2^- bond. At this small value of $\Delta\Phi$, only the $X \rightarrow B$ transition has appreciable strength and the threshold value for the solute bondlength is greater than 4Å. Therefore, as the cluster size increases from $n = 10$ to 16, I_2^- spends less time in the regions that contribute to the transient absorption peak.

In summary, the integrated intensity of the transient feature in the simulated pump-probe spectrum is actually greater in $I_2^-(CO_2)_{10}$ than in $I_2^-(CO_2)_{16}$, but the transient appears more **distinct** in the larger clusters, in agreement with the experiments. The prominence of the transient peak in the larger clusters is due to a component of the ensemble which passes through the absorption window within a narrow time window prior to the accumulation of population in the bottom of the I_2^- vibrational well.

5.2.3 $I_2^-Ar_{20}$

If slightly slower vibrational relaxation increases the intensity of the transient absorption feature, as observed for $I_2^-(CO_2)_{10}$ relative to $I_2^-(CO_2)_{16}$, shouldn't the effect be even more prominent in a system with a vibrational relaxation timescale that is orders of magnitude longer than the electronic relaxation timescale? $I_2^-Ar_{20}$ clusters are an ideal system for testing this suggestion. Experiments [6, 11, 12] and simulations [17] have demonstrated that while relaxation to and recombination on the ground electronic

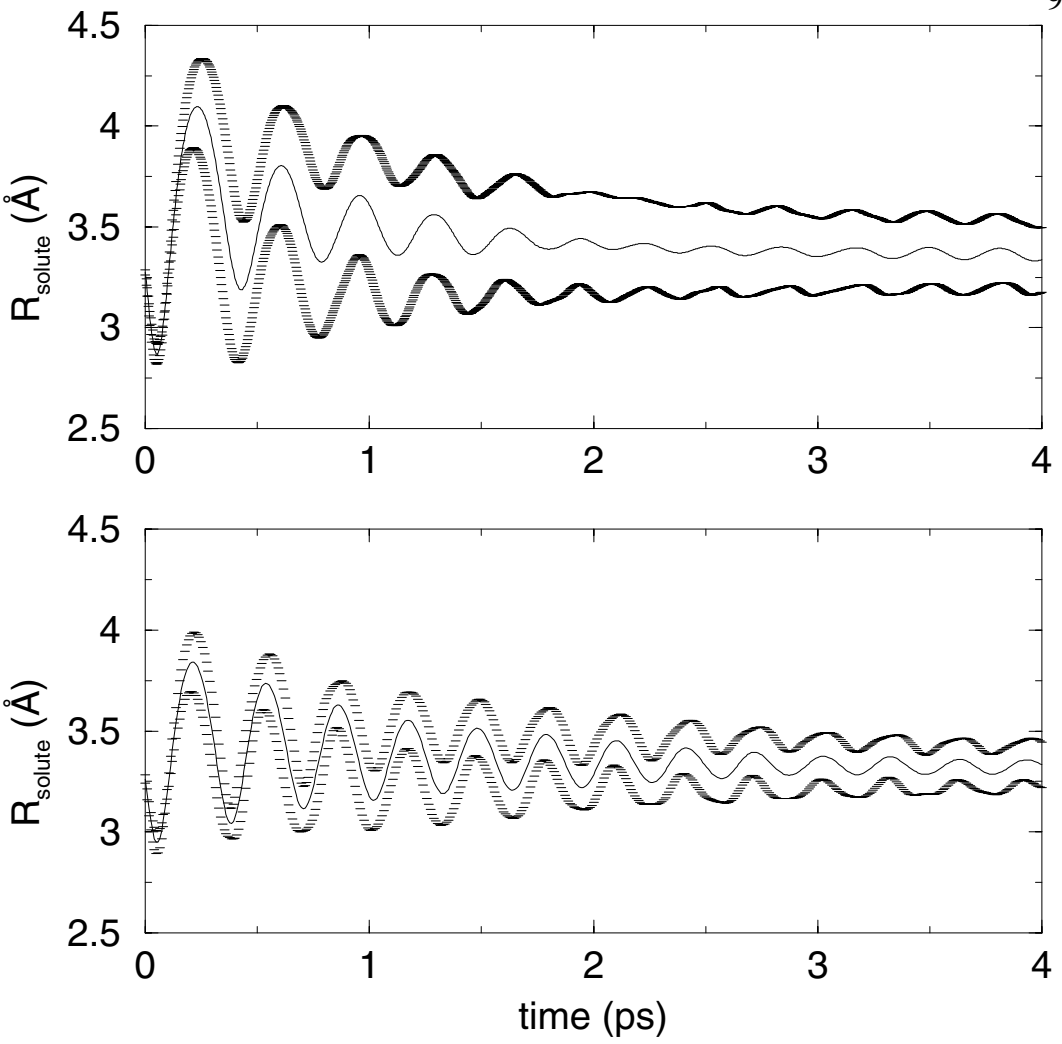

Figure 5.6: Ensemble average of the solute bondlength after recombination for $I_2^-(CO_2)_n$ (a) $n = 10$ and (b) $n = 16$.

state occurs within 5-10 ps after excitation, complete vibrational relaxation requires upwards of 200 ps.

Figure 5.7 shows the calculated absorption recovery for $I_2^-Ar_{20}$ with the pump and probe wavelength of 790 nm. The total signal (heavy solid line) is characterized by an intense peak at about 7 ps and a long time tail which levels off beyond 200 ps. Virtually all of the 790 nm spectrum arises from transitions originating on the X state of I_2^-. The signal corresponding to the $X \rightarrow A'$ (pump) transition, shown by the (dashed) line, rises monotonically from 3–200 ps. The peak at early time, including the

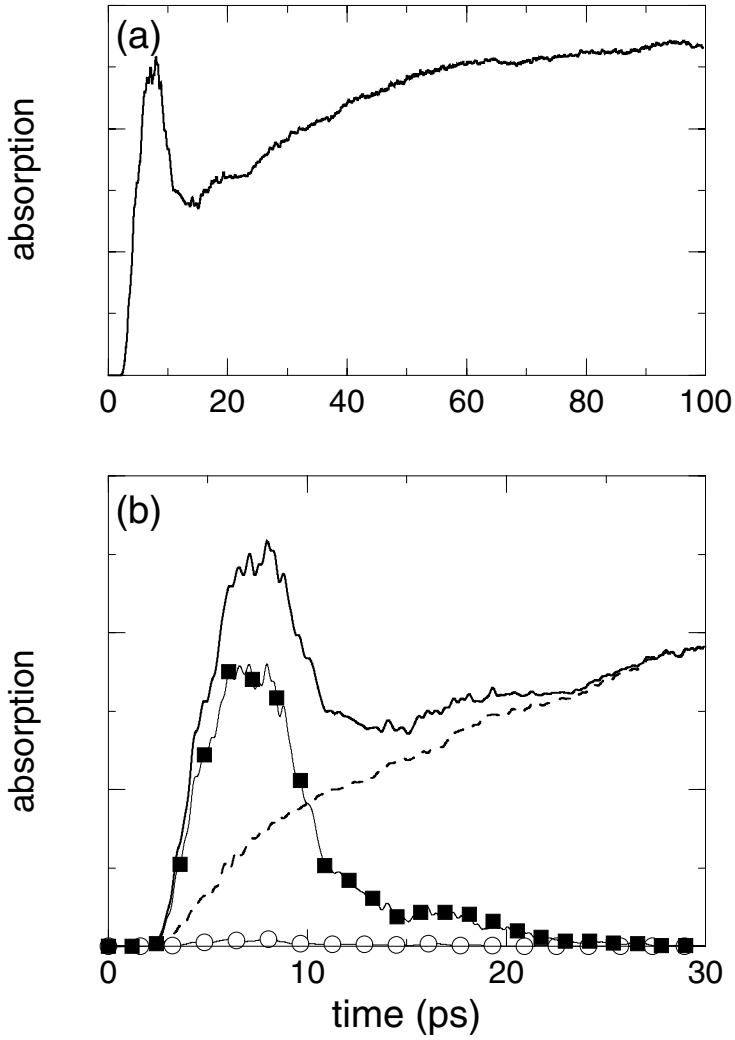

Figure 5.7: Aborption recovery of $I_2^- Ar_{20}$ (a) Total simulated signal. (b) Solid line is the total simulated signal from a 250-trajectory ensemble, dots are the experimental data. Dashed line is the contribution from the $X \rightarrow A'$ transition. The transient feature at 2 ps is due to $X \rightarrow a'$ and $X \rightarrow B$ transitions, shown respectively by the open circles and filled squares.

shoulder which extends to 25 ps, is due to the $X \rightarrow B$ transition. There is a very small contribution from the $X \rightarrow a'$ transition from 5–10 ps.

Figure 5.8 plots the regions of greatest transition strength at 790 nm visited by the trajectories as a function of the solute bondlength and the solvent coordinate. The $X \rightarrow B$ transition is resonant with 790 nm at $R_{\mathrm{solute}} = 4.2$–$4.3$ Å. As described

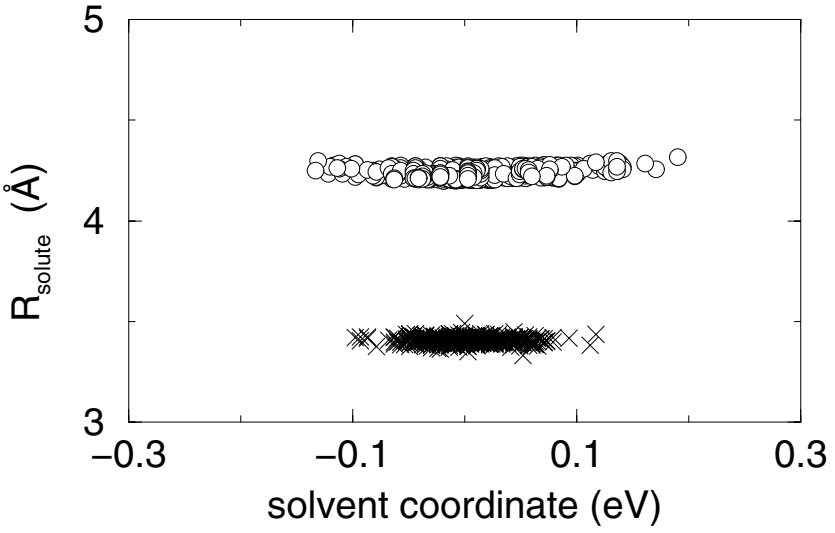

Figure 5.8: Location of strong, 790 nm absorption regions in the (R, $\Delta\Phi$) plane. Transitions originate on the X state and end on the A' (x's) and B (filled circles) states. Arrow represents simplified pathway for trajectories recombining on the X state.

in Section 5.2.1, the intensity of this transition is strongest as $|\Delta\Phi|$ nears zero. The solvent coordinate is restricted to much smaller magnitudes in argon relative to CO_2 and therefore trajectories do not pass through the Franck-Condon regions for strong $X \rightarrow a'$ transitions located at large solvent coordinates for $R_{\mathrm{solute}} \leq 4$ Å.

The experimental absorption recovery signal measured by Vorsa et al. is a smoothly rising curve, similar to the contribution from the $X \rightarrow A'$ transition of our simulated signal. The complete lack of evidence for transient absorption in the experimental signal appears to be in direct conflict with the simulated spectrum, but before drawing this conclusion, we must reconsider what was actually observed in the experiments. The pump-probe signal is not a direct absorption measurement, but rather an action spectrum. That is, a secondary effect of absorption is measured and used to infer the absorption signal. In the present case, it is the mass distribution of photodissociation and recombination products that is observed directly. To generate the absorption recovery signal at a given time delay, the mass spectrum is measured and all of the products

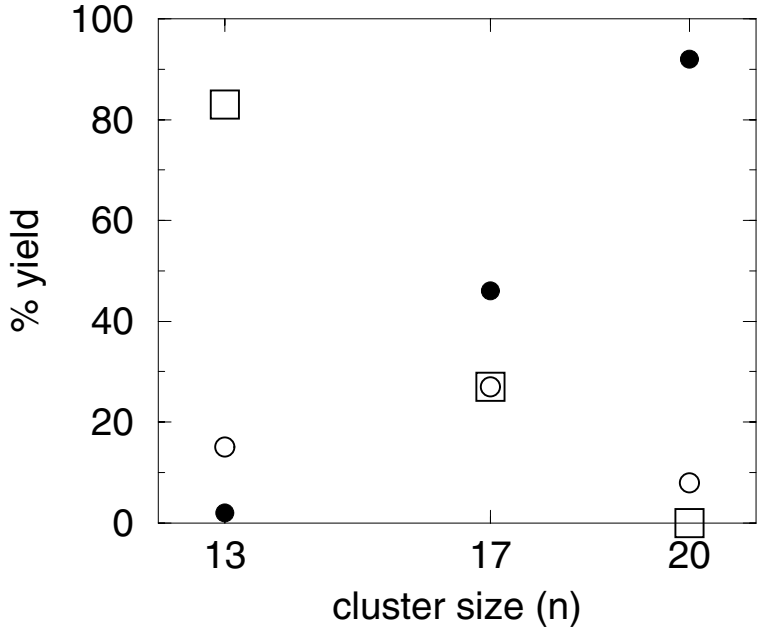

Figure 5.9: UV photodissociation products. Squares: dissociation on the B state. Open circles: dissociation on the a' state. Filled circles: metastable recombination on the a' state.

corresponding to two-photon absorption are added together. The signal is normalized to the number of two-photon products detected at an effectively infinite time delay. However, this method requires **a priori** knowledge of what constitutes a two-photon product and that the one- and two-photon product channels are mass-separable. Our simulations of the absorption recovery indicate that the transient absorption is due to the $X \rightarrow(a',B)$ transition. We must ask, "What are the final products if the second pulse promotes I_2^- to the spin-orbit excited states?"

To address this question, we have simulated the photodissociation of $I_2^-Ar_n$ clusters at 395 nm. This ultraviolet pulse excites I_2^- to the B electronic state. Three product channels are observed: dissociation on the B state, dissociation on the a' state, and metastable recombination on the a' state. The branching ratios between these products for cluster sizes $n = 13, 17,$ and 20 are shown in Fig. 5.9. We do not observe any relaxation to the lower spin-orbit states of I_2^-. This is consistent with the mechanism

for spin-orbit relaxation of $I_2^-(CO_2)_n$ clusters discussed in Chapter 4.

The key step in the relaxation process involves bringing states of the upper and lower spin-orbit manifolds together in energy. This is possible because of the large differences in the solvent potential at each iodine atom which occur in asymmetric $I_2^-(CO_2)_n$ clusters. In contrast, the solute-solvent interactions are much weaker in $I_2^-Ar_n$ clusters, and the maximum magnitude of the solvent coordinate which can be attained with 20 argon atoms is only about a third of spin-orbit splitting energy of iodine. This explains why no products on the lower spin-orbit states are observed.

Consider now the excitation of I_2^- to the B state by the probe photon. The absorption originates on the X electronic state at a solute bondlength of roughly 4.4 Å. At this bondlength, the B state has nearly reached its dissociative limit. In the absence of a mechanism for spin-orbit relaxation, the photon energy is almost entirely converted into electronic energy of spin-orbit excited iodine and there is virtually zero kinetic energy released. This means that no additional solvent molecules are evaporated from the cluster and the photoproducts are identical to the products following absorption of only the pump pulse. Therefore, these products would be excluded from the experimental two-photon signal and no transient absorption feature would be detected.

The experimental signal should be compared to the overall rise of the simulated spectrum, which is due to the $X \rightarrow A'$ contribution. This is shown in Fig. 5.10. Although there is some ambiguity as to whether either signal has truly reached its asymptotic behavior, the simulated signal shows a faster initial recovery. The time scales for electronic and vibrational relaxation from our simulations agree well with those determined from FPES experiments [11, 17, 33] and so it is not clear what causes the discrepancy between these two pump-probe signals. One source of error may be the bondlength dependence of the transition dipole strengths as determined by our **ab initio** calculations.

Finally, we note that the fact that the transient peak involves excitation to the spin-

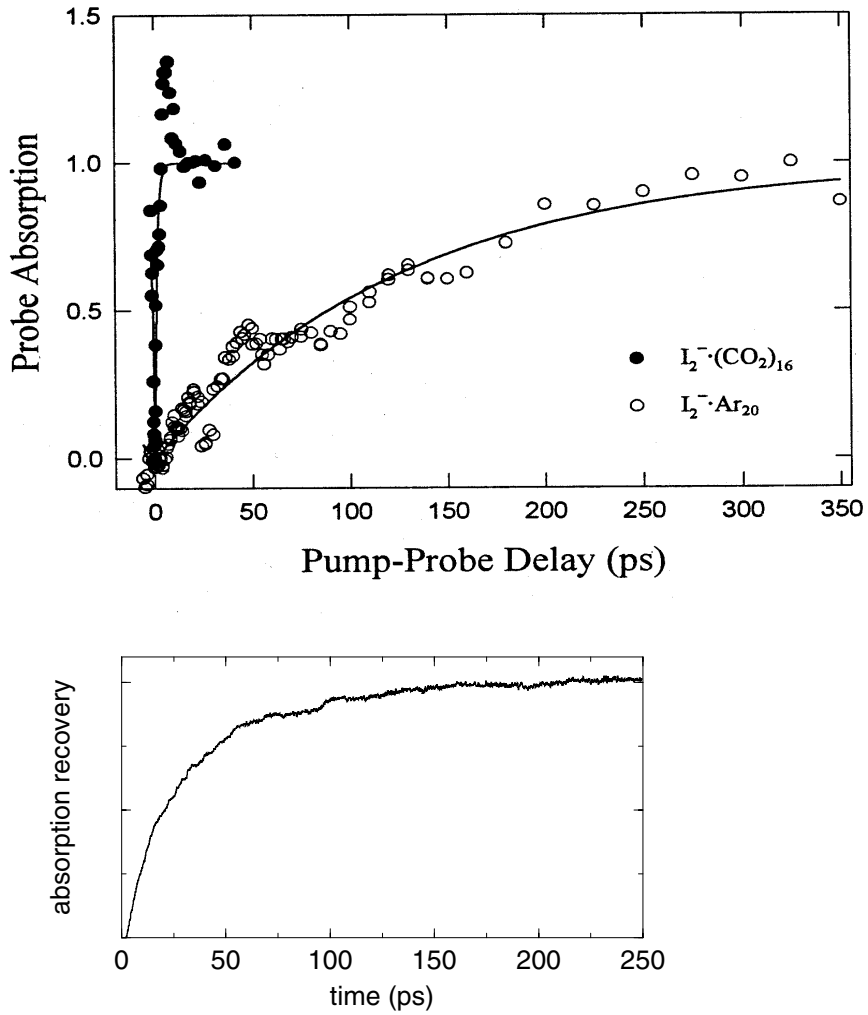

Figure 5.10: Aborption recovery of $I_2^- Ar_{20}$. Top panel shows experimental results from Ref. 6. Bottom panel shows longtime behavior of simulated spectrum.

orbit excited states affects the interpretation of the absorption recovery of $I_2^-(CO_2)_n$ clusters as well. While there is a mechanism for spin-orbit relaxation in these systems, the probability for return to the lower manifold varies with cluster size and is less than one at $n = 16$. Thus it is possible that some of the two-photon products are missing from the experimental signal in this system as well. Additional molecular dynamics simulations may be able to determine whether these products are separable from the one-photon products. This should be investigated before a quantitative comparison between the experimental and simulated absorption spectra is made.

5.3 Conclusions

Figures 5.2 and 5.3 lead to a physical picture for the photodissociation/recombination process in $I_2^-(CO_2)_n$ clusters that ties together the insights derived from earlier studies. After dissociation, some members of the ensemble temporarily recombine on the A state, but others hop directly to the ground state in less than 2 ps [16, 18]. As I and I^- recombine on the X state, they pass through the strong $X \rightarrow (a', B)$ absorption region at R=4–5 Å. This initial coherent passage gives rise to the 2 ps transient peak. Since recombined I_2^- loses energy very rapidly to the solvent, particularly near the top of the ground state well [34, 35], it never returns to the large-R absorption region, so the transient is not repeated. Instead, the solute relaxes vibrationally, giving rise to the main $X \rightarrow A'$ absorption recovery. This rapid vibrational relaxation is accompanied by a rapid loss of coherence in the ensemble, as seen in Fig. 5.6. At longer times the recovery signal is dominated by the slow build-up of population on the X state as the A state is electronically quenched, rather than by the very fast X-state vibrational relaxation. Since the simulations underestimate the electronic quenching rate, they overestimate the time scale for overall absorption recovery.

In summary, our simulations provide strong evidence that the 2 ps peak in the absorption recovery signal is due to transitions from the ground state to the spin-orbit excited states of I_2^-, not to transitions originating on the intermediate A state. The transient absorption occurs as the photofragments first begin to recombine, rather than at the inner turning point, and is strongly influenced by the solvent environment. The transient is not seen experimentally in $I_2^-Ar_n$ clusers because there is no efficient mechanism for quenching the spin-orbit excitation energy, and therefore the final products from these transitions are not included in the two-photon mass signal. This reassignment is consistent with all of the experimental evidence, and reinforces the physical picture of the recombination dynamics that has emerged from earlier simulations.

References for Chapter 5

[1] J. Papanikolas, V. Vorsa, M. Nadal, P. Campagnola, J. Gord, and W. C. Lineberger, J. Chem. Phys. **97**, 7002 (1992).

[2] J. Papanikolas, V. Vorsa, M. Nadal, P. Campagnola, H. Buchenau, and W. C. Lineberger, J. Chem. Phys. **99**, 8733 (1993).

[3] J. M. Papanikolas, I_2^- Photodissociation and Cage Recombination Dynamics in Size-Selected $I_2^-(CO_2)_n$ Clusters, PhD thesis, University of Colorado, 1994.

[4] D. A. V. Kliner, J. C. Alfano, and P. F. Barbara, J. Chem. Phys. **98**, 5375 (1993).

[5] P. K. Walhout, J. C. Alfano, K. A. M. Thakur, and P. F. Barbara, J. Phys. Chem. **99**, 7568 (1995).

[6] V. Vorsa, S. Nandi, P. J. Campagnola, M. Larsson, and W. C. Lineberger, J. Chem. Phys. **106**, 1402 (1997).

[7] S. Nandi, A. Sanov, N. Delaney, J. Faeder, R. Parson, and W. C. Lineberger, J. Phys. Chem. A **102**, 8827 (1998).

[8] A. E. Johnson, N. E. Levinger, and P. F. Barbara, J. Phys. Chem. **96**, 7841 (1992).

[9] G. Ashkenazi, U. Banin, A. Bartana, R. Kosloff, and S. Ruhman, Adv. Chem. Phys. **100**, 317 (1997).

[10] A. Sanov, S. Nandi, and W. C. Lineberger, J. Chem. Phys. **108**, 5155 (1998).

[11] B. J. Greenblatt, M. T. Zanni, and D. M. Neumark, Science **276**, 1675 (1997).

[12] B. J. Greenblatt, M. T. Zanni, and D. M. Neumark, Faraday Discuss. **108**, 101 (1997).

[13] V. S. Batista and D. F. Coker, J. Chem. Phys. **106**, 7102 (1997).

[14] J. Faeder, N. Delaney, P. Maslen, and R. Parson, Chem. Phys. Lett. **270**, 196 (1997).

[15] N. Delaney, J. Faeder, P. E. Maslen, and R. Parson, J. Phys. Chem. A **101**, 8147 (1997).

[16] J. Faeder, N. Delaney, P. Maslen, and R. Parson, Chem. Phys. **239**, 525 (1998).

[17] J. Faeder and R. Parson, J. Chem. Phys. **108**, 3909 (1998).

[18] C. Margulis and D. F. Coker, J. Chem. Phys. **110**, 5677 (1999).

[19] A. Sanov, T. Sanford, S. Nandi, and W. C. Lineberger, J. Chem. Phys. **111**, 663 (1999).

[20] N. Delaney, J. Faeder, and R. Parson, J. Chem. Phys. **111**, 651 (1999).

[21] P. E. Maslen, J. Faeder, and R. Parson, Chem. Phys. Lett. **263**, 63 (1996).

[22] A. J. Stone, The Theory of Intermolecular Forces, Oxford, New York, 1996.

[23] Y. Zhao, C. C. Arnold, and D. M. Neumark, J. Chem. Soc. Faraday Trans. **89**, 1449 (1993).

[24] C. S. Murthy, S. F. O'Shea, and I. R. McDonald, Mol. Phys. **50**, 531 (1983).

[25] L. Verlet, Phys. Rev. **159**, 98 (1967).

[26] M. P. Allen and D. J. Tildesley, Computer Simulation of Liquids, Clarendon Press, Oxford, 1987.

[27] J. C. Tully, J. Chem. Phys. **93**, 1061 (1990).

[28] S. Hammes-Schiffer and J. C. Tully, J. Chem. Phys. **101**, 4657 (1994).

[29] V. S. Batista and D. F. Coker, J. Chem. Phys. **106**, 6923 (1997).

[30] We compare to the "magic angle" absorption recovery, Fig. 9a of Ref. 2, in which the effects of cluster rotation have been removed by averaging the two absorption signals measured with the probe parallel and perpendicular to the pump. This is the appropriate signal with which to compare our simulation, because our calculated absorption intensities do not take into account the orientation of the transition dipole in the laboratory frame.

[31] E. C. M. Chen and W. E. Wentworth, J. Phys. Chem. **89**, 4099 (1985).

[32] M. T. Zanni, V. S. Batista, B. J. Greenblatt, W. Miller, and D. M. Neumark, JCP **110**, 3748 (1999).

[33] B. J. Greenblatt, Femtosecond Photoelectron Spectroscopy: A New Tool for the Study of Anion Dynamics, PhD thesis, University of California, 1999.

[34] I. Benjamin, P. F. Barbara, B. J. Gertner, and J. T. Hynes, J. Phys. Chem. **99**, 7557 (1995).

[35] J. M. Papanikolas, P. E. Maslen, and R. Parson, J. Chem. Phys. **102**, 2452 (1995).

Chapter 6

Summary of Solvated I_2^- Photodissociation Dynamics: Comparing Solvents

The goal of this chapter is to provide a review of the photodissociation dynamics of solvated I_2^- with a focus on comparing two different solvents: argon and carbon dioxide. Many additional solvents have been studied experimentally in the gas [1–6] and liquid [7–10] phases; this is the first step in generalizing our understanding beyond systems which have been simulated. Ultimately, we would like to develop a kinetic model for the dynamics which takes into account the effect of differing solute-solvent and solvent-solvent interactions on the rate of each mechanistic step. Such a model would allow a more detailed analysis of experimental absorption recovery signals.

6.1 Energetics and Structure

The nature of the solvent-solvent interaction is a key factor in determining how the solvent cluster is built up around the chromophore. In $I_2^-Ar_n$ clusters, the argon–argon interactions are relatively small ($\approx$10 meV) and isotropic, so the packing of argon atoms into the first solvent shell follows a simple pattern. Distinct six-membered rings form around the internuclear axis, beginning at the center of the I_2^- bond, filling the space around one I atom with a second ring and one atom at the axial site; the structure repeats around the other end [11]. These structures are shown in Fig. 6.1(a). On average, each argon atom is bound to the cluster by 74 meV. In $I_2^-(CO_2)_n$ clusters, sol-

vent molecules pack in the same general manner, starting at the waist, filling one end and then the other, but the details are different due to the non-spherical shape of CO_2 and the stronger solvent-solvent interactions. In small clusters, CO_2 molecules clump together on one side of the I_2^- bond as seen in the structure of $I_2^-(CO_2)_5$. The average binding energy for each CO_2 molecule is about 190 meV in the smaller cluster sizes and rises to 200 meV for clusters with 10–18 CO_2 molecules.

The distribution of the solvent around I_2^- may look rather similar for clusters with roughly half a solvent shell, but the forces exerted by these solvent configurations are actually quite different. This is why the asymmetry of the solvent environment is quantified **energetically** by the solvent coordinate, $\Delta\Phi$. As discussed in Chapter 2, $\Delta\Phi$ is the difference in the electrostatic potential at the two iodine nuclei. Figure 6.2 shows the average equilibrium magnitude of the solvent coordinate as a function of initial cluster size. For both solvents the maximum solvent asymmetry occurs for clusters with slightly more than half a solvent shell, but the maximum value is almost an order of magnitude larger in CO_2. This dramatic difference has decisive consequences for photodissociation and recombination in the two solvents.

6.2 Near-IR Photodissociation

We begin an overview of the photodissociation process by considering excitation to the A' state, and limiting the dynamics to the lower spin-orbit manifold. First, we describe how the photofragmentation products depend on the two solvents, and then we discuss the effects of varying the solvent on the excited state lifetimes, which ultimately determine the absorption recovery signals presented in the previous chapter.

6.2.1 A' state

One of the first and most dramatic results of our simulations was the observation of anomalous charge flow, or negative polarizability, of I_2^- in the A' electronic state

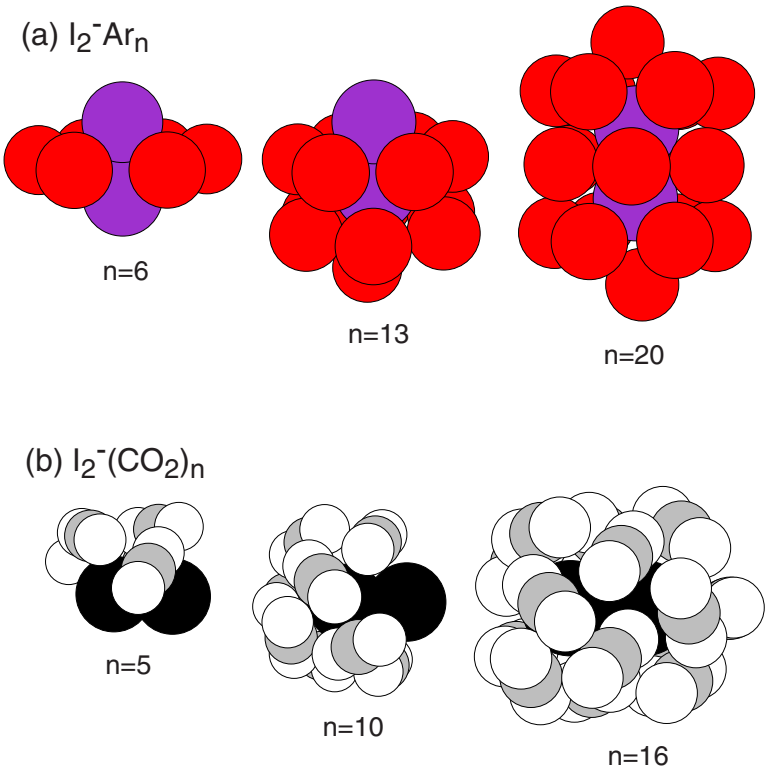

Figure 6.1: Equilibrium structures of (a) $I_2^-Ar_n$ and (b) $I_2^-(CO_2)_n$ clusters, for selected values of n, showing the build-up of the first solvent shell.

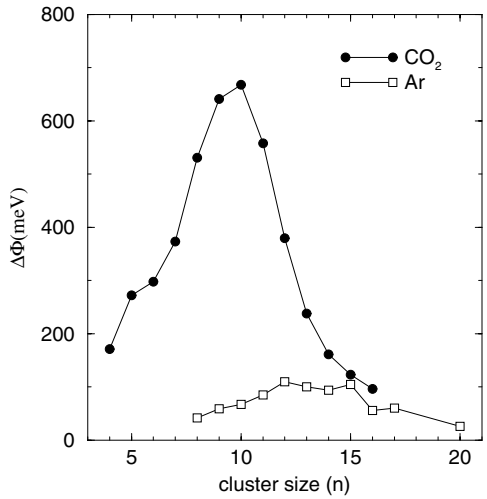

Figure 6.2: Ensemble average of the magnitude of the solvent coordinate as a function of cluster size.

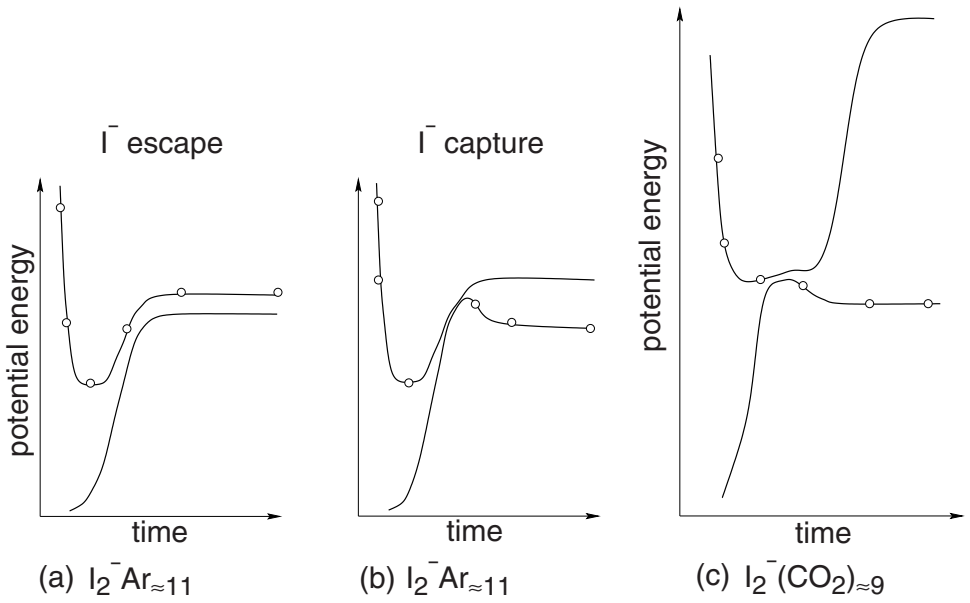

Figure 6.3: Qualitative sketches of the potential energy versus time, following excitation of I_2^-. The two states shown correspond to solvated I^- + I (lower state) and I^- + solvated I (upper state). The open circles indicate the occupied state. For $I_2^-Ar_{n\approx 11}$, (a) and (b), the asymptotes are separated by 50–250 meV. For $I_2^-(CO_2)_{n\approx 9}$, (c), the asymptotes are separated by nearly 1 eV.

[11]. The localization of charge away from the solvent cluster as I_2^- dissociates has a profound effect on the dynamics, and amplifies the disparity between different solvents. For example, the photodissociation of $I_2^-Ar_n$ clusters yields two channels of dissociative products: a lighter set of ionic fragments from clusters that dissociate directly on the A' state, where I^- is ejected from the cluster, and a heavier set of fragments from clusters that return to the A or X, normal charge flow, state prior to dissociation. In CO_2 clusters with four or more solvent molecules, only the second product channel is observed.

There are four electronic states directly involved in the photodissociation of solvated I_2^- at 720–790 nm, but there are only 2 distinct dissociation limits, namely, solvated I^- + I (X and A states) and I^- + solvated I (A' and a states). Figure 6.3 shows a cartoon of the potential energy versus time for one state from each asymptote, comparing $I_2^-Ar_{n\approx 11}$ and $I_2^-(CO_2)_{n\approx 9}$ to illustrate which dissociative channels are energetically accessible. The value of the potential energy of the occupied electronic state at $t = 0$

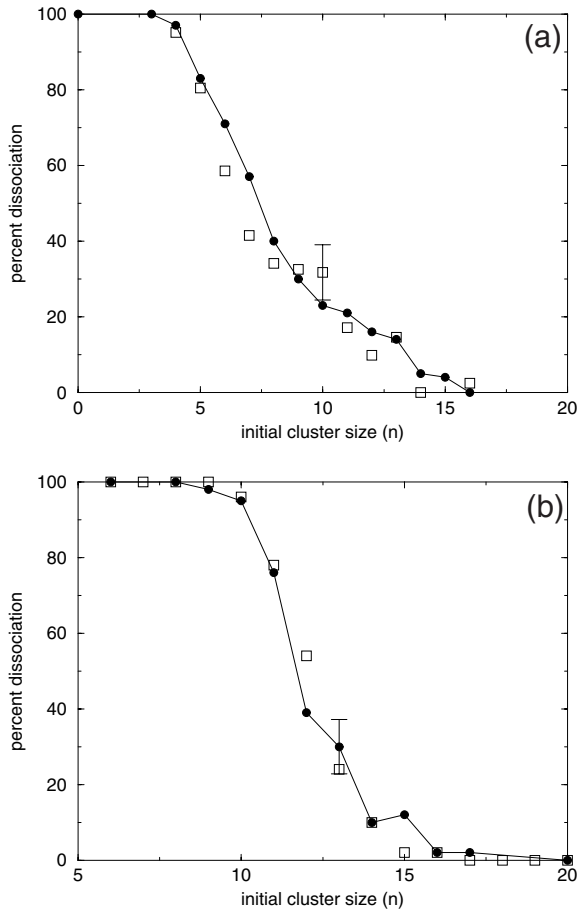

Figure 6.4: Percent dissociation of I_2^-, following 790 nm excitation as a function of initial cluster size, n, for (a) $I_2^-(CO_2)_n$ and (b) $I_2^-Ar_n$. The squares are the simulation results, the circles are experimental results of Lineberger and coworkers. The 1σ error bar is based on the statistical sampling of the simulations and is represenative of the error bars at all cluster sizes.

gives an upper bound for the energy available to the cluster. For $I_2^-Ar_{n\approx11}$, represented in Figure 6.3(a) and (b), the energetic difference between the two dissociative limits is only 50–250 meV, well below the ≈0.5 eV of excess kinetic energy. Recall that the initial solvent configuration is asymmetric and that the solvent must reorganize into a symmetric configuration to bring about transitions to the normal charge flow states, as described in Chapter 3. Therefore, branching between the two product channels is the result of a race between the dissociation of I_2^- and the reorganization of the solvent cluster. The situation is quite different in $I_2^-(CO_2)_{n\approx9}$. Because the Coulombic attrac-

tion between the solvent cluster and the nascent I^- ion is very strong, the normal and anomalous dissociative channels differ by about 1 eV, creating an insurmountable barrier to dissociation on the A'/a state. A nonadiabatic transition to the A or X state is, therefore, a prerequisite for dissociation of I_2^- in CO_2 clusters.

The same electrostatic caging that prevents the direct dissociation of $I_2^-(CO_2)_{n\geq 4}$ clusters on the A' electronic state accounts for the onset of I_2^- recombination in small CO_2 clusters. The percent dissociation of I_2^- as a function of initial cluster size is shown for the two solvents in Fig. 6.4. As I_2^- dissociates following photoexcitation in a CO_2 cluster, the neutral iodine fragment collides with the solvent cluster and dissipates its kinetic energy (kinematic caging), while the escaping ion is subjected to a strong, long-range Coulombic attraction (electrostatic caging). The anomalous charge flow, characteristic of the repulsive electronic state, sets up a cluster configuration which very effectively transfers the dissociation energy into the solvent degrees of freedom. In contrast, electrostatic caging is not as efficient in a cluster of structureless, weakly interacting, argon atoms; the recombination process relies much more heavily on kinematic caging, and therefore, dissociation is not quenched by clusters with less than half a solvent shell.

6.2.2 A state

In the previous section, we looked at the asymptotic behavior of the four lowest electronic states of I_2^- relevant to dissociation following excitation to the A' state. At large internuclear separations, the A and X states are degenerate, and for simplicity, they were considered together in Fig. 6.3. Now we consider the dynamics of recombination, so we turn our attention to the potential energy curves at shorter distances. The electronic coupling between the two iodine atoms is much stronger in the X state than in the A state. As a result, the X state well depth is 1.01 eV, corresponding to a bond order of 1/2, whereas the A state well depth is only about 160 meV, comparable

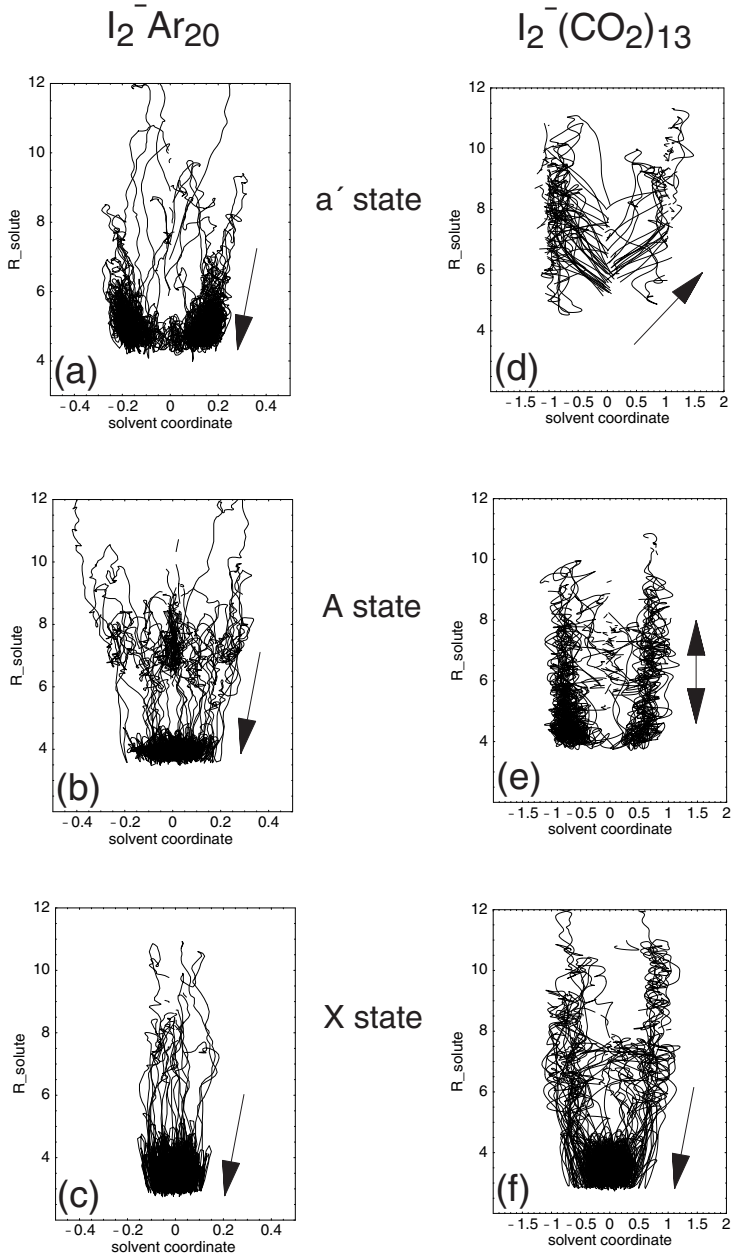

Figure 6.5: Two-dimensional maps of simulation trajectories comparing the three bonding states of I_2^- . $I_2^-Ar_{20}$: a' state dynamics from 395 nm excitation, A, X state dynamics from 790 nm excitation. $I_2^-(CO_2)_{13}$: all dynamics from 395 nm excitation.

to the solute-solvent interactions. Once again, the different binding energies of argon and CO_2 to the cluster are critical factors in determining the course of the dynamics.

Figure 6.5 displays examples of the molecular dynamics simulation trajectories

for $I_2^-Ar_{20}$ and $I_2^-(CO_2)_{13}$ on each of the three I_2^- electronic states that are predominantly bonding in character, and therefore exhibit normal charge flow. Panels (a) and (d) depict motion on the spin-orbit excited state, a', and will be discussed below. As described in Chapter 2, the motion of trajectories on a surface defined by the solute bondlength and the solvent coordinate reveals information about the competing forces of chemical bonding, which favors a delocalized charge distribution, and solvation, which favors a compact, localized charge distribution. Figures 6.5(b) and (c) show the A state dynamics of $I_2^-Ar_{20}$ and $I_2^-(CO_2)_{13}$, respectively. In argon clusters, I_2^- is known to recombine on the A state [11, 14–17] and remain bound for at least 5 μs [13]. The stability of the I_2^- bond in our simulations is indicated by the single well along the solvent coordinate at short solute bondlengths. In contrast, $I_2^-(CO_2)_n$ clusters in this electronic state trace out a double well potential with only rare passages between the two wells. In this case, the solvation forces are greater than the I_2^- bond strength; the CO_2 cluster solvates I^- and pushes the neutral iodine into the second solvation shell. On the A state, the $I_2^-(CO_2)_n$ cluster is better described as an I^- ion solvated by CO_2 and an iodine atom than as solvated I_2^-. This configuration is also referred to as a solvent-separated pair.

Although neutral I is not bound as tightly to I^- on the A state as the CO_2 molecules are, there is still a small attraction which delays the dissociation of I_2^-, and the trajectories do spend a considerable amount of time at short bondlengths where the energy gap between the X and A states is too large to permit transitions to the X state. The diffusive motion we observe for trajectories on the A state leads to the wide range of lifetimes we observe for this state. It can take less than one or more than 100 picoseconds for I_2^- to dissociate or undergo electronic relaxation. The FPES studies on $I_2^-(CO_2)_n$ clusters by Neumark and coworkers [18] also appear to indicate that some clusters are trapped on the A state, however, they cannot say with certainty how long the clusters remain trapped. One spectral feature attributed to trapping on the A state

disappears within 4 ps [18], while another, whose assignment is still tentative, may persist for as long as 200 ps [19]. The absorption recovery experiments of the Lineberger group suggest that the recombination dynamics are essentially complete within 40 ps, although it is possible that the experiment is not sensitive to a small tail of lingering excited state population ($\approx 10\%$). Currently, it seems likely that there are multiple mechanisms involved in quenching the A state population, and additional analysis of the simulations and experiments will be necessary to settle this issue.

As more experimental information about the A state lifetime becomes available, we will be able to assess the quality of the solvated A state potential, which is one possible source of error in the simulations. A second unknown factor is the correct rate of nonadiabatic transitions between electronic states. Also, the effect of neglecting intramolecular CO_2 vibrations on the vibrational relaxation of I_2^- in excited electronic states has not been examined. The relaxation dynamics on the ground electronic state have been studied using a model for flexible CO_2 molecules, and it was concluded that the CO_2 bending vibration only slightly enhanced the I_2^- vibrational relaxation rate [20]. However, the same study found that a hyperflexible CO_2 model resulted in the polarization of the solute even at its equilibrium geometry. In excited electronic states, where the solute bondstrength is reduced, the CO_2 bend may be an important factor missing from our simulations. Finally, the effect of CO_2 vibrations on the **electronic** relaxation rate of I_2^- is entirely unknown and should not be assumed inconsequential. The asymmetric stretch mode of CO_2, for example, carries a strong transition dipole moment which could couple strongly to the electronic charge flow, giving rise to additional electronic quenching channels.

6.2.3 X state

The dynamics of the clusters following return to the ground electronic state tells us about the vibrational relaxation of solvated I_2^- and also reflects the electronic relax-

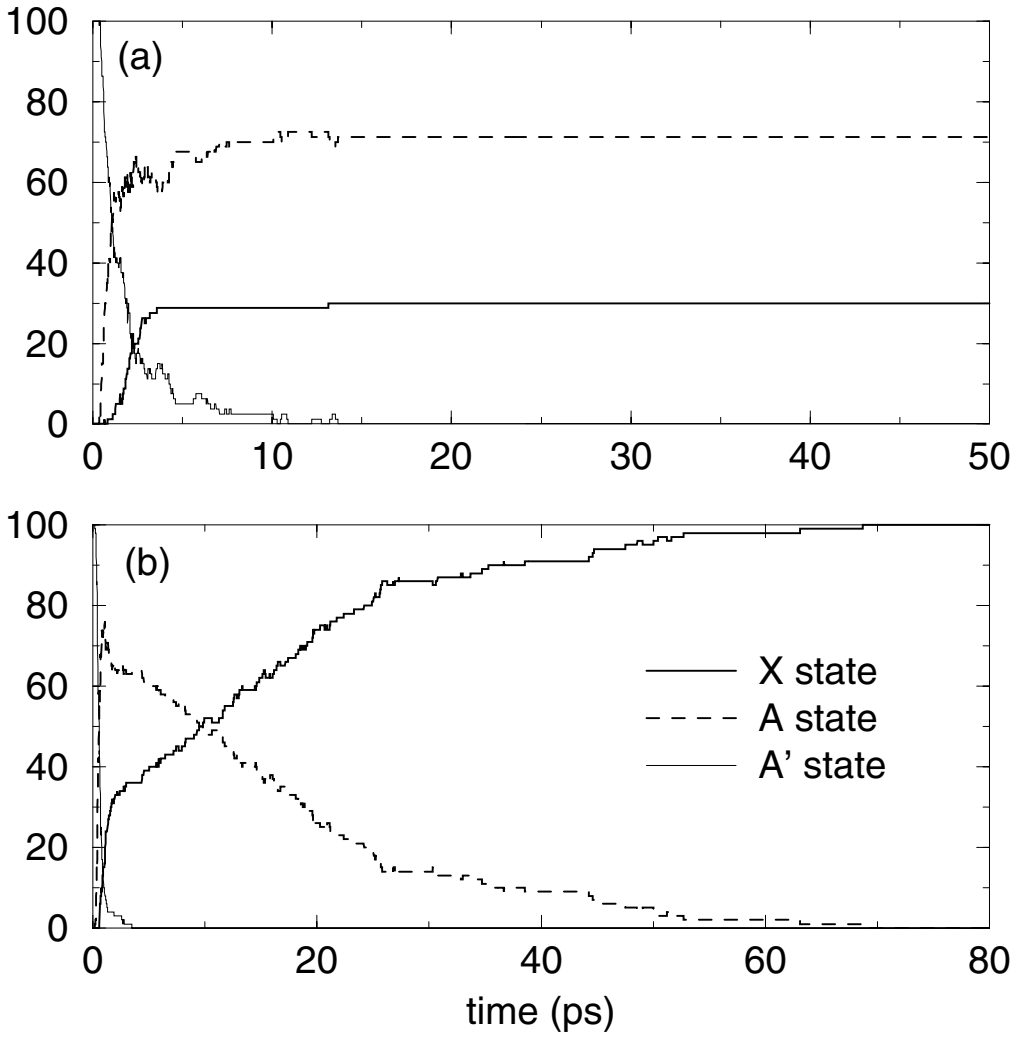

Figure 6.6: Population of each electronic state as a function of time following near-IR photodissociation of $I_2^-Ar_{20}$ and $I_2^-(CO_2)_{16}$ ensembles.

ation processes that produces the ground state population. Figure 6.6 shows the population of each electronic state as a function of time following excitation of $I_2^-Ar_{20}$ at 790 nm and $I_2^-(CO_2)_{16}$ at 720 nm. As we saw above, $I_2^-Ar_n$ clusters that enter the A state recombine there. The clusters that recombine on the X state, generally follow trajectories that relax directly from the A' state to the X state. Thus the electronic relaxation process is straightforward, and one can fit exponential timescales for recombination in each state. The time constants are $x = 5$–10 ps and $a = 15$ ps for recombination onto the ground and first excited state, respectively [15]. These are in agreement with the

values extracted from the FPES experiments [17].

The electronic relaxation of I_2^- in CO_2 clusters is more complicated because the trajectories that enter the A state are not permanently trapped there, but rather, ultimately leak out and return to the X state. Fig. 6.6(b) shows that about 30% of the trajectories relax directly from the A' state to the X state, as in $I_2^-Ar_{20}$. However, there appear to be two additional timescales for relaxation to the X state. By 25 ps, 80% of the trajectories have relaxed and by 75 ps the relaxation is essentially complete. These three timescales are evident in our simulations of $I_2^-(CO_2)_{16}$ at 790 nm as well, although they are not as distinct. In that study, which is discussed in Chapter 3, 20% recombined within 2 ps, 80% recombined within 25 ps, and 97% recombined within 75 ps. As mentioned in the previous section, further analysis of the dynamics simulations will be necessary to determine if there are mechanistic differences in the relaxation processes leading to these multiple timescales.

Ensemble averages of three properties of the ground state dynamics are particularly useful for describing the cluster relaxation. The solute bondlength and the energy in the solute bond give direct information about the vibrational relaxation of I_2^-, and the number of solvent molecules remaining gives information about the transfer of energy to the cluster and its removal through evaporative cooling. These quantities are shown in Fig. 6.7.

For $I_2^-Ar_{20}$, the ensemble can be divided into two parts, corresponding to recombination on the ground and first excited electronic states, and the ensemble averages provide a straightforward picture of the relaxation process. Focusing on the X state dynamics, we see that the maximum extension of the solute bond occurs at 2.5 ps and the solute energy at this point is essentially at its dissociative limit. By 10 ps, I_2^- has recombined on the X state. The solute energy shows that a large fraction of the vibrational excitation has been dissipated, and this is tracked closely by evaporation of argon atoms. The remaining vibrational relaxation is extremely slow because most of

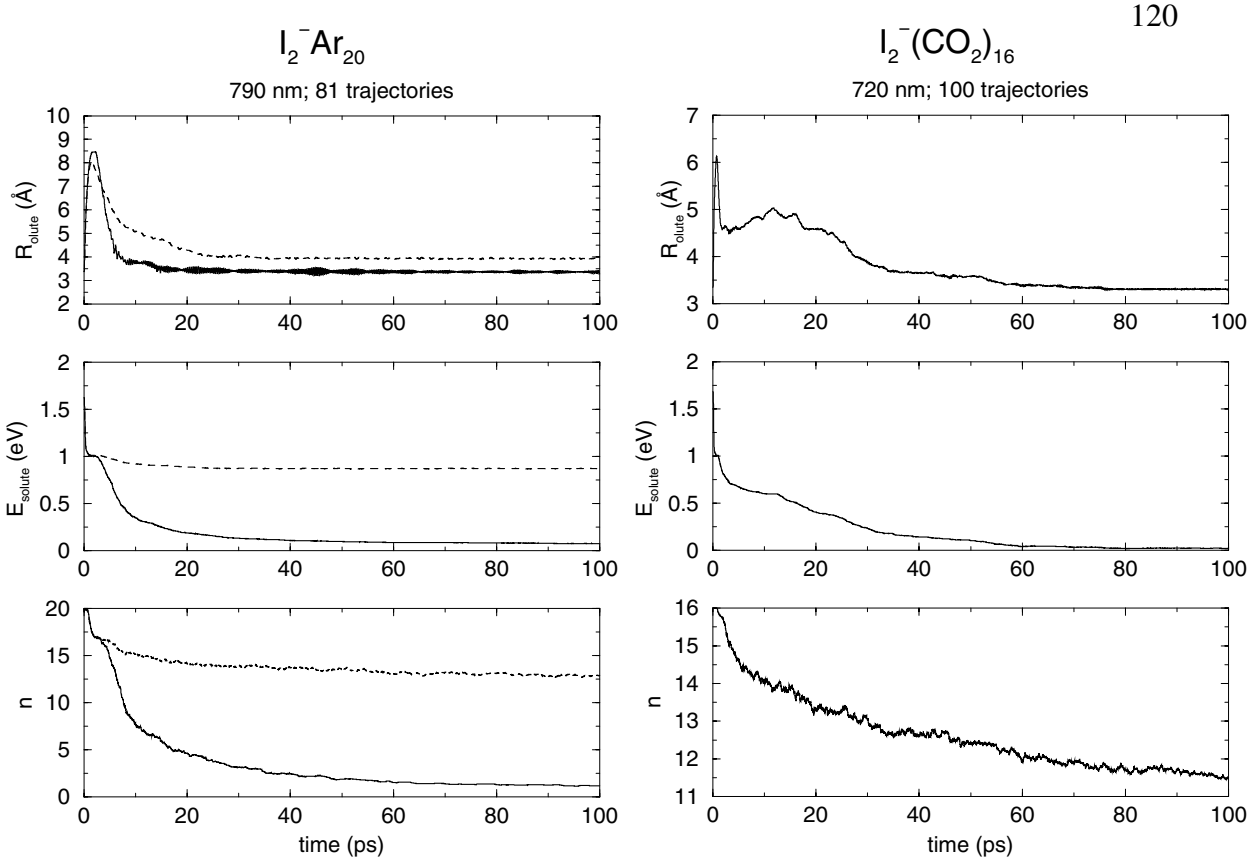

Figure 6.7: Ensemble averages of the solute bondlength, solute energy and number of solvent molecules in the cluster for $I_2^-Ar_{20}$ and $I_2^-(CO_2)_{16}$

the solvent cluster has been evaporated.

For $I_2^-(CO_2)_{16}$, the broad range of A state lifetimes yields complicated kinetics, and the averages are difficult to interpret beyond 1 or 2 ps. To filter out the complications introduced by the electronic relaxation dynamics, the same averages are plotted in Fig. 6.8 with time offset for each trajectory such that $t_0 \equiv t_{recombination}$. The recombination time is defined as the first passage through the equilibrium bondlength. By aligning all of the trajectories this way we can isolate and study the process of vibrational relaxation. For $I_2^-(CO_2)_{16}$, oscillations in the average solute bondlength collapse to a very narrow range around R_e within about 5 ps of recombination. During this same time frame, the energy in the solute bond drops to 25 meV, indicating that vibrational relaxation is essentially complete.

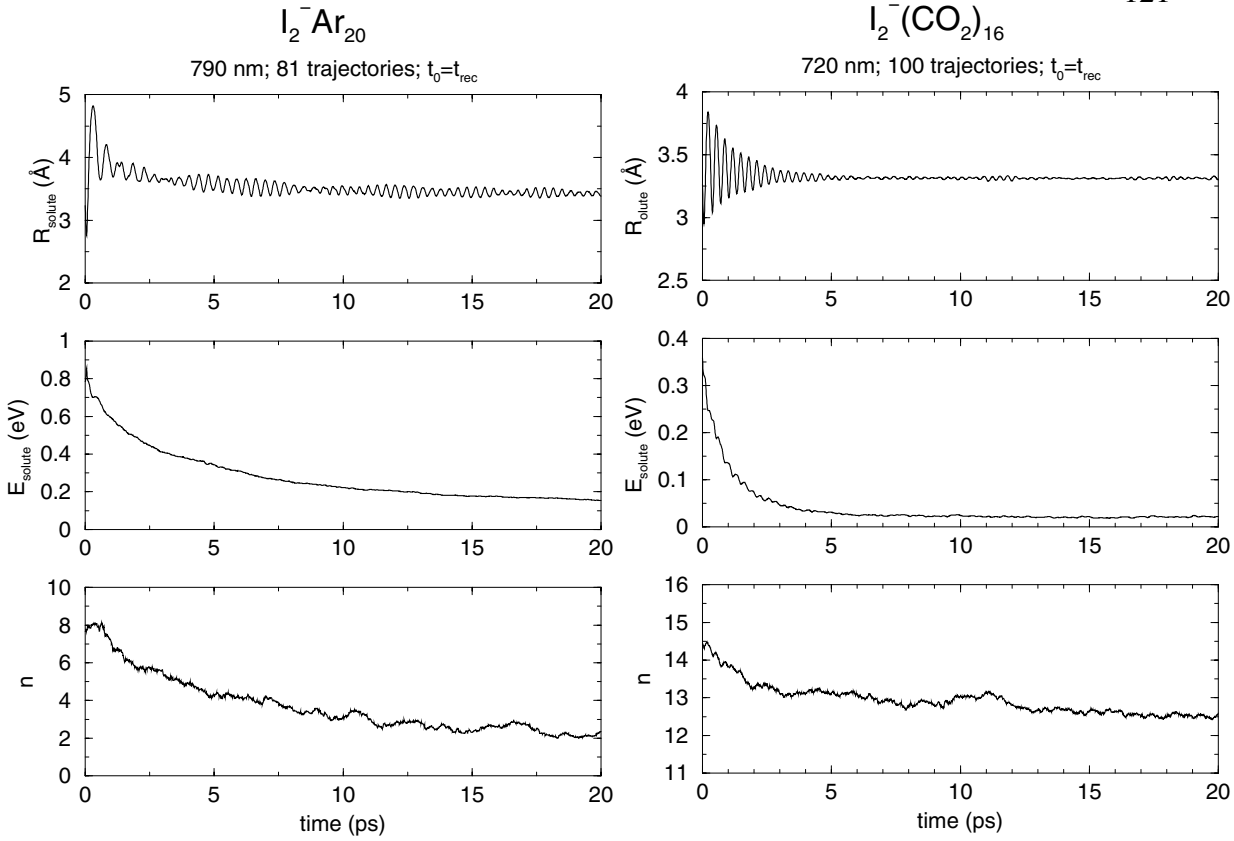

Figure 6.8: Ensemble averages of the solute bondlength, solute energy and number of solvent molecules in the cluster for $I_2^- Ar_{20}$ and $I_2^-(CO_2)_{16}$ with $t_0 \equiv t_{recombination}$.

There is a striking difference in the initial value of the solute energy for the two solvents in these plots. For argon, $E_{\rm solute} \approx$ 1eV, but for CO_2 $E_{\rm solute} \approx$ 0.35 eV. This is a consequence of setting $t_0 \equiv t_{recombination}$ and it tells us that the very first compression of the I_2^- bond in CO_2 clusters is extremely efficient at removing vibrational energy. By the time I_2^- crosses R_e for the first time, almost two-thirds of the vibrational excitation has been quenched. This result is consistent with previous studies of the vibrational relaxation of solvated I_2^- [21–23], which found that the delocalization of the ionic charge during recombination interacts with the electrict field of the solvent environment, creating a frictional force that diverts energy from the solute to the solvent.

The internal modes of CO_2 can accept energy from the solute and also contribute to the faster vibrational relaxation rate observed, relative to argon clusters. In our

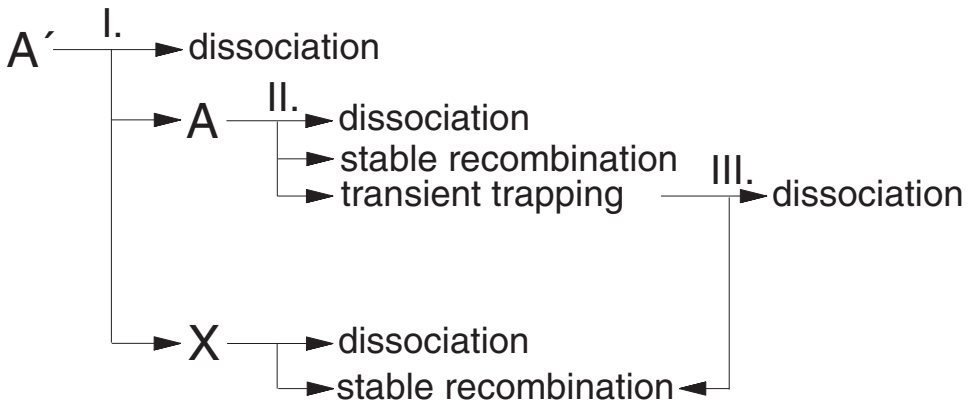

Figure 6.9: Summary of reaction pathways following near-IR excitation of I_2^-. Branching points I. II. and III. are discussed in the text.

model, CO_2 is rigid and so rotations are the only additional accepting modes. However, the strong solvent–solvent interactions have a distinctly preferred orientation and these modes are very good at damping I_2^- vibrations. The vibrations of CO_2 are neglected in the simulations presented here, but their effect on the vibrational relaxation rate has been shown to be small [20].

Finally, the greater binding energy of CO_2 to the cluster means that evaporation of each solvent molecule is more effective at cooling than each argon atom. The bottom panel of Fig. 6.8 shows that 20 ps after recombination there are, on average, 13.5 CO_2 molecules remaining, but only 2 argon atoms. A larger cluster of argon atoms is needed to dissipate all of the I_2^- vibrational energy.

6.2.4 Absorption Recovery

Figure 6.9 outlines the reaction pathways we have observed following near-IR photodissociation of solvated I_2^-. The strength of solvation forces, relative to the electronic coupling within the solute, is a major factor in determining the dynamics at each branching point. To help visualize the effects of the solvent cluster, Fig. 6.10 shows a schematic set of potential curves for the A', A, and X states of solvated I_2^-. Mul-

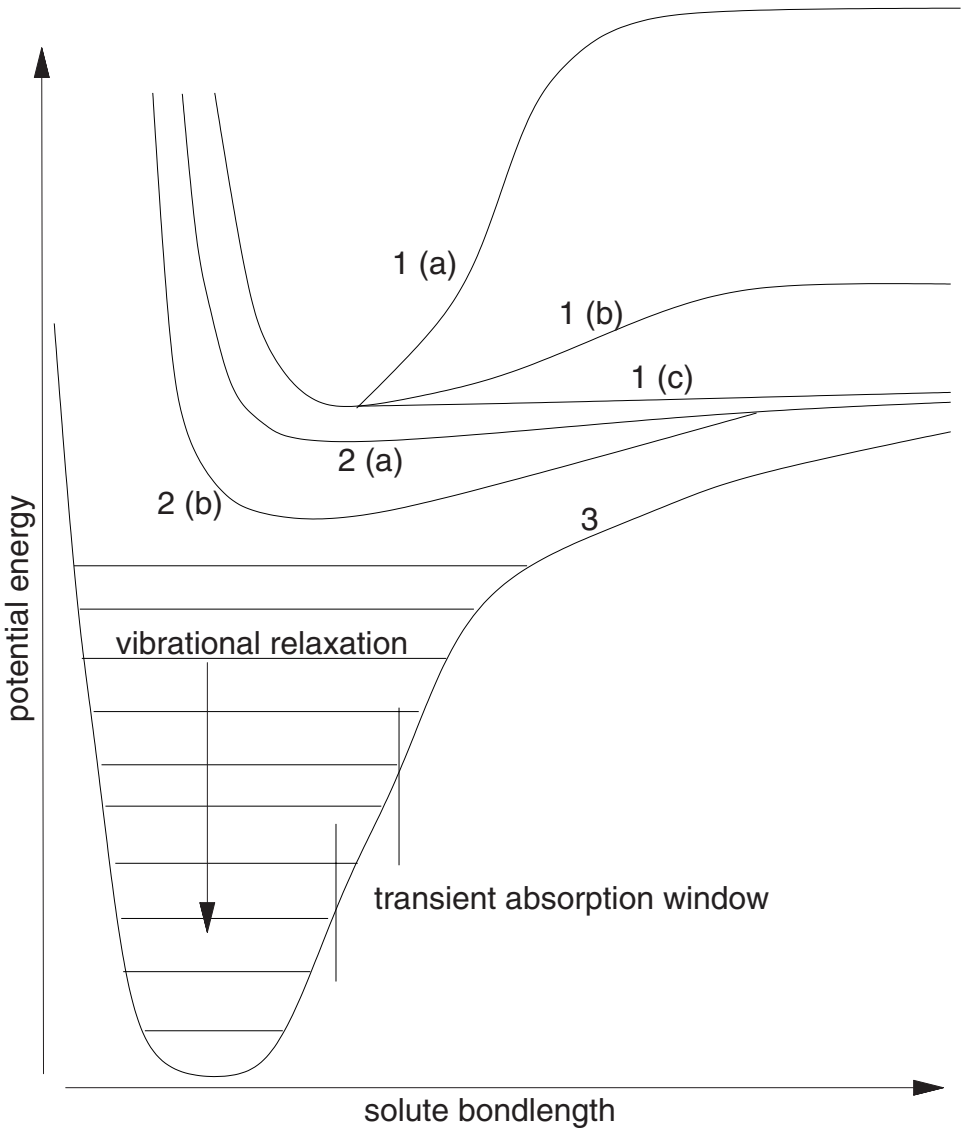

Figure 6.10: Schematic solvated I_2^- potentials. 1(a) A' dissociation, strong solvent. 1(b) A' dissociation, weak solvent. 1(c) Symmetric solvent cluster linking anomalous and normal charge flow states. 2(a) Trapping on A state, strong solvent. 2(b) Recombination on A state, weak solvent. 3 X state recombination. Rate of vibrational relaxation depends on solvent and cluster size.

tiple curves are shown for the A' and A states to characterize both strong and weak solvent environments. We emphasize that this is just a qualitative picture to illustrate key points that should be considered when interpreting the dynamics of these systems. Using Fig. 6.9 and Fig. 6.10 as guides, we summarize the dynamics and discuss how it

manifests itself in the absorption recovery signal.

I. Dissociation begins on the A' electronic state. Since this state exhibits anomalous charge flow, direct dissociation entails ejecting I^- from the cluster. This is only energetically possible if the solvation forces are smaller than the excess photon energy. Fig. 6.10, curve 1(b) illustrates a weakly interacting solvent which would allow dissociation on the A' state. In contrast, Fig. 6.10, curve 1(a) shows a strongly interacting solvent which prevents I^- escape and forces electronic relaxation to the A and X states. Of the trajectories that relax to normal charge flow states, approximately 3/4 enter the A state and 1/4 enter the X state. This is probably due to the fact that the A' and A states come into resonance at a shorter bondlength than do the A' and X states. In larger clusters, where recombination is the dominant product channel, the 25% of trajectories that enter the X state directly are the most likely to contribute to the transient absorption peak, as discussed below.

II. On the A state, the evaporation of a few weakly bound solvent molecules can remove enough energy to stabilize the I_2^- bond, as shown in Fig. 6.10, curve 2(b). In argon clusters, A state I_2^- photoproducts are detected 5 μs after excitation [13]. In systems with stronger solvent–solvent and solvent–I^- interactions, the A state I_2^- bond is destabilized by the solvent and solvent-separated pairs may form.

III. Ultimately, I^- and I separate and dissociate completely or recombine on the X state. The lifetime for transient trapping is not well characterized at this time, and it appears that multiple relaxation mechanisms are available.

As discussed in Chapter 5, the absorption recovery signal measures the overall relaxation of I_2^- from the A' state to the bottom of the X state well, with additional contributions that arise when the X state population passes through the transient absorption window shown in Fig. 6.10. The longer the time spent in the absorption window, the larger the integrated intensity of the transient feature. Systems with slower vibrational relaxation rates spend more time in the absorption window and so are expected to have

greater intensity in the transient peak. Whether or not the transient absorption produces a peak which is clearly distinct from the overall recovery signal is determined by the relative rates of population flowing into the ground state (electronic relaxation) and passing through the enhanced absorption region (vibrational relaxation). In the case of $I_2^-Ar_{20}$, electronic relaxation into the X state is complete within 15 ps of the initial excitation, while vibrational relaxation requires more than 200 ps. This combination produces the distinct, intense transient absorption peak evidenced in our simulations. In $I_2^-(CO_2)_{16}$, the electronic relaxation process is more complicated due to population which is temporarily trapped in the A state. We do observe a transient peak due to the 25% of the population that relaxes promptly to the X state, but the peak is not as intense as in $I_2^-Ar_{20}$ because the vibrational relaxation time in $I_2^-(CO_2)_{16}$ is only a few picoseconds, therefore trajectories quickly relax below the transient absorption window.

6.3 UV Photodissociation

Our simulations of the photodissociation of solvated I_2^- at 395 nm revealed an efficient mechanism for relaxation of the solute spin-orbit energy through a charge transfer process that occurs in highly asymmetric solvent configurations, as described in Chapter 4.

6.3.1 B state

In several ways, the dynamics on the spin-orbit excited states echo behavior seen in the near-IR studies. Excitation at 395 nm places I_2^- on the B electronic state, which exhibits anomalous charge flow, as does the A' state accessed at 720-790 nm. Direct dissociation on such a state involves ejection of an ion from the cluster, which is inhibited by the Coulombic force between the fragments. At 720-790 nm excitation, this ion ejection mechanism was seen to be feasible in $I_2^-Ar_n$ clusters, but was completely suppressed in the more strongly bound $I_2^-(CO_2)_n$ clusters. In the latter, dissociation could

only occur after an electronic transition to a normal charge flow state. The situation is somewhat different for excitation at 395 nm, which places I_2^- 1.1 eV above the I^- + I^* dissociative limit. This energy is comparable to the amount required to remove I^- from a small cluster of CO_2 molecules, and in our simulations we do observe a small amount (1-2%) of I^- ejection from $I_2^-(CO_2)_n$ clusters with $n \leq 8$, in addition to facile I^- ejection from the $I_2^-Ar_n$ clusters. While this is a small effect in the CO_2 clusters, it is useful to know that the possibility of I^- ejection from even a tightly bound solvent exists. It is something that must be considered in future studies as it adds another possible component to the overlapping product distributions.

6.3.2 a' state

The a' electronic state is the third normal charge flow state in our model of the I_2^- electronic structure and provides a final opportunity to examine the competition between the solvent and chemical bonding forces. The well depth determined from the **ab initio** calculation of Maslen et al. is about 80 meV, about half that calculated for the A state. While we do not yet have any independent measure of the absolute accuracy of these values, we may hope that the the relative magnitudes are approximately correct. In any case, it is useful to know the well depth of these bonds in our dynamics, relative to the solute-solvent interactions. Figure 6.5 shows $I_2^-Ar_{20}$ clusters on the a' electronic state. We observe trapping that persists for at least 100 ps. Note, though, that the trajectories behave differently than on the A state. On the a' state, trajectories do still cross through $\Delta\Phi = 0$ –an indication that the solute bond has reformed– but the trajectories appear to spend more time on one side or the other; there appear to be 2 wells centered at ± 0.15 eV. The reduction of the bond strength from 160 meV to 80 meV means that the solvent-solute interaction of 75 meV per solvent atom creates a collective solvent force that can destabilize the bond. This illustrates the transition from a strong bond to strong solvation, which may be useful in constructing a statistical model for the excited

state lifetime.

The glaring difference between argon and CO_2 clusters is the order of magnitude difference in the range of accessible solvent coordinates. As shown in Chapter 4, the dynamics on the a' electronic state change dramatically when the solvent coordinate is as large as the spin-orbit splitting of the solute. When this threshold condition is met, the possibility of a charge transfer transition, quenching the spin-orbit excitation of I_2^-, arises. This occurs in our simulations for clusters with $n \geq 8$. Since a large solvent asymmetry is required for this pathway, and the charge transfer places I_2^- on an anomalous charge flow state, where very symmetric solvent configurations are optimal, this mechanism effectively transfers energy from the solute to the solvent. As a result, we observe the onset of caging with about half a solvent shell even though more than 3 eV of photon energy is put into the solute bond.

6.4 Closing Remarks

While much of the disscussion presented here focuses on interpreting and understanding specific experimental results, we have also tried to develop conceptual models of the effects of solvation on dissociation reactions that we hope will be more generally applicable. For example, the discovery of a solvent mediated spin-orbit relaxation mechanism, decribed in Chapter 4, represents a major change in perspective regarding the types of reaction pathways that are available, compared to previous work on dihalide photodissociation. Nevertheless, our explanation of the mechanism requires only a minor generalization of the well-established theory of electron transfer reactions in solution. Indeed, the foundations of this approach had already been laid 6 years ago by the work of Barbara and coworkers [9, 10] and Hynes and coworkers [22, 24–27], who described I_2^- vibrational relaxation in the electronic ground state by means of a Marcus electron transfer picture; our major contribution lay in extending these ideas to describe dynamics on multiple, strongly coupled electronic excited states.

The characteristics of the $I_2^-(CO_2)_n$ systems, which led to the efficient spin-orbit relaxation mechanism are hardly unique: multiple product channels, separated by energy gaps that are comparable in size to the solvation forces, and a mix of bonding and antibonding states. The key ingredient here is a strong, anisotropic solvent environment that can respond to changes in the electronic structure of the solute. It will be interesting to see if the concepts (if not the simulation methods) presented here can be extended to describe reactions in much larger systems, for example, the interaction between an enzyme, which is the epitome of a custom-crafted solvent environment, and a substrate.

In the meantime, there is a wealth of experimental information on dihalide anion photodissociation waiting to be explored. In addition to the experiments of the Lineberger group and the Neumark group that we have discussed, Barbara and coworkers have investigated the photodissociation of I_2^- in a variety of liquid solutions and at a variety of probe wavelengths [7–10, 22]. These direct absorption measurements map out the dynamics on the A electronic state as well as the X state, however, to date there has been insufficient understanding of the dynamics and spectroscopy of excited I_2^- to extract all of the information locked in the experimental signals. The overview of the dynamics presented here and its effects on the absorption recovery signal serve as a starting point for building a kinetic model that will assist in interpreting these experiments.

References for Chapter 6

[1] M. Nadal, The Study of the Photodissociation and Recombination Dynamics of Mass-Selected Cluster Ions: Solvent Effects on the Structure and Dynamics of the Ionic Chromophore, PhD thesis, University of Colorado, 1996.

[2] S. Nandi, A. Sanov, N. Delaney, J. Faeder, R. Parson, and W. C. Lineberger, J. Phys. Chem. A **102**, 8827 (1998).

[3] M. E. Nadal, S. Nandi, D. W. Boo, and W. C. Lineberger, J. Chem. Phys. (1998), to be submitted.

[4] A. Sanov, S. Nandi, and W. C. Lineberger, J. Chem. Phys. **108**, 5155 (1998).

[5] A. Sanov, T. Sanford, S. Nandi, and W. C. Lineberger, J. Chem. Phys. **111**, 663 (1999).

[6] M. E. Nadal, P. D. Kleiber, and W. C. Lineberger, J. Chem. Phys. **105**, 504 (1996).

[7] A. E. Johnson, N. E. Levinger, and P. F. Barbara, J. Phys. Chem. **96**, 7841 (1992).

[8] D. A. V. Kliner, J. C. Alfano, and P. F. Barbara, J. Chem. Phys. **98**, 5375 (1993).

[9] J. Alfano, Y. Kimura, P. K. Walhout, and P. F. Barbara, Chem. Phys. **175**, 147 (1993).

[10] P. K. Walhout, J. C. Alfano, K. A. M. Thakur, and P. F. Barbara, J. Phys. Chem. **99**, 7568 (1995).

[11] J. Faeder, N. Delaney, P. Maslen, and R. Parson, Chem. Phys. Lett. **270**, 196 (1997).

[12] J. Papanikolas, J. Gord, N. Levinger, D. Ray, V. Vorsa, and W. C. Lineberger, J. Phys. Chem. **95**, 8028 (1991).

[13] V. Vorsa, P. J. Campagnola, S. Nandi, M. Larsson, and W. C. Lineberger, J. Chem. Phys. **105**, 2298 (1996).

[14] V. S. Batista and D. F. Coker, J. Chem. Phys. **106**, 7102 (1997).

[15] J. Faeder and R. Parson, J. Chem. Phys. **108**, 3909 (1998).

[16] B. J. Greenblatt, M. T. Zanni, and D. M. Neumark, Science **276**, 1675 (1997).

[17] B. J. Greenblatt, M. T. Zanni, and D. M. Neumark, Faraday Discuss. **108**, 101 (1997).

[18] B. J. Greenblatt, Femtosecond Photoelectron Spectroscopy: A New Tool for the Study of Anion Dynamics, PhD thesis, University of California, 1999.

[19] B. J. Greenblatt, M. T. Zanni, and D. M. Neumark, private communication.

[20] B. M. Ladanyi and R. Parson, J. Chem. Phys. **107**, 9326 (1997).

[21] J. M. Papanikolas, P. E. Maslen, and R. Parson, J. Chem. Phys. **102**, 2452 (1995).

[22] I. Benjamin, P. F. Barbara, B. J. Gertner, and J. T. Hynes, J. Phys. Chem. **99**, 7557 (1995).

[23] I. Benjamin and R. M. Whitnell, Chem. Phys. Lett. **204**, 45 (1993).

[24] H. J. Kim and J. T. Hynes, J. Chem. Phys. **96**, 5088 (1992).

[25] B. J. Gertner, K. Ando, R. Bianco, and J. T. Hynes, Chem. Phys. **183**, 309 (1994).

[26] R. Bianco and J. T. Hynes, J. Chem. Phys. **102**, 7885 (1995).

[27] R. Bianco and J. T. Hynes, J. Chem. Phys. **102**, 7864 (1995).

Chapter 7

Modeling $I_2^-(OCS)_n$ Clusters

This chapter documents work in progress to develop a potential model for $I_2^-(OCS)_n$ clusters that can be used with the molecular dynamics simulation methods described in Chapter 2 to study the photodissociation of this system. The photofragmentation and photodissociation dynamics of $I_2^-(OCS)_n$ clusters have been investigated at 790 nm and 395 nm by Lineberger and coworkers [1, 2]. They have also conducted two-color pump-probe studies to gain more information about the cluster dynamics [3, 4].

7.1 Parametrizing the Interaction Hamiltonian

The model Hamiltonian discussed in Chapter 2 is a sum of the Hamiltonians of the isolated molecules, plus terms describing the solute–solvent and solvent–solvent interactions. Here we discuss the process of designing model potentials required for evaluating the interaction terms. These terms include long-range electrostatic and induction forces (Coulomb forces) and short-range dispersion and repulsion. In ionic systems we expect the long-range interactions to dominate the attractive region of the interaction potential. We therefore approximate the short-range interactions with state-independent pairwise potentials and rely on them primarily to set the repulsive wall of the potential in the correct place. As we will see below, the general approach for fitting our interaction potential is to calculate the long-range interactions using the model Hamiltonian and then seek out a short-range potential, which when added to the Coulombic in-

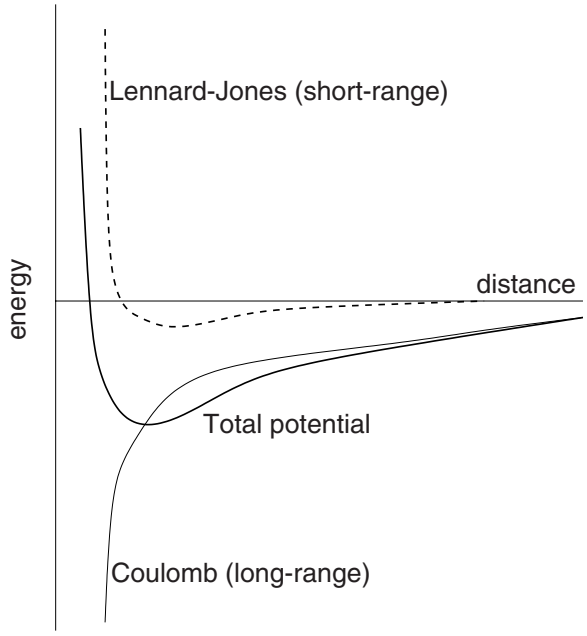

Figure 7.1: The solute–solvent, solvent–solvent interaction potential is a sum of the long-range Coulomb potential and short-range Lennard-Jones potential. The model parameters are chosen so that $R_{\rm e}$ and $D_{\rm e}$ of the total potential agree with known quantities.

teraction, produces a potential surface that has an equilibrium geometry (R_e and D_e) consistent with a known experimental or **ab initio** potential, see Fig. 7.1.

In our model, the solvent charge distribution is treated classically, represented by a distributed multipole expansion [5, 6]. For $I_2^-(CO_2)_n$ we have found that the five point charge model of Murthy et al. [7], combined with a single polarization site at the solvent center of mass provides an adequate description of the CO_2 charge distribution [6, 8]. We anticipate that a similar model will be acceptable for OCS. The short-range interactions in our model are typically treated by atom-atom Lennard-Jones potentials. The availability of empirical data to fit these potentials for OCS–OCS interactions is discussed in the following section.

To model the solute-solvent interactions, we also need to parametrize the short-range solute-solvent interactions. Since there is very little information available for interaction potentials of I_2^- with various solvents, we typically fit to data for interac-

tions of the solvent with the I^- and I fragments. Scattering data and photoelectron spectroscopy have been used to characterize these potentials for CO_2 and argon [9, 10], however this information is not available for OCS. This is the topic of the next section. Finally, we note that in modeling $I_2^-(CO_2)_n$, we find that the same short-range potentials can be used to describe the interaction of the solvent with both the I^- and neutral I fragments, and we assume this to be valid for OCS as well.

In summary, we need to select the following parameters for the solvent–solvent and solute-solvent interactions: point charges for OCS, molecular polarizability of OCS, Lennard-Jones parameters for O–O, C–C, S–S, O–C, O–S, C–S, I–O, I–C, and I–S.

7.2 Available Data

Ideally, we would fit our model potentials to experimentally determined values for equilibrium structures of I(OCS), I^-(OCS), I_2^-(OCS) and $(OCS)_n$ clusters; however, very little empirical data is available for any of these systems. To the best of our knowledge, a recent **ab initio** calculation by Sanov et al. [1] represents all that is known about the I_2^-–OCS and I^-–OCS potentials. There are differing reports about the structure and binding energy of OCS dimer [11–13]. In this section, we describe the data available for the interactions we are modeling and in the following section we describe our attempts to reproduce what we believe are the most important attributes of these potentials.

Figure 7.2(b) shows a contour plot of the two-dimensional potential surface for I^-(OCS) as determined from electronic structure calculations [1]. The global minimum of this potential surface corresponds to a linear configuration with sulfur nearest I^-. This dipole-bound minimum has a dissociation energy of 220 meV, and the S–I distance is 3.6 Å. There is a secondary, quadrupole-bound minimum, which is nearly T-shaped and bound by 67 meV. Calculations for I_2^-(OCS) were peformed at selected geometries

Table 7.1: Geometries and energies of OCS dimer minima

structure	R (Å)	Θ (deg)	Energy (meV) MP2	model
Fig. 7.2(a)	3.6388	90.5	-60.9	-57.2
Fig. 7.2(b)	4.2529	47.1	-47.8	-44.8
Fig. 7.2(c)	3.9979	116.2	-48.8	-41.8
Fig. 7.3(a)	3.5665	88.5	–	-57.9
Fig. 7.3(b)	–	–	–	-65.6

and the minimum energy configuration was determined to be T-shaped with the sulfur end pointing toward the I_2^- waist. The dissociation energy for this complex is 137 meV, and the distance between sulfur and the I_2^- center of mass is 3.7 Å.

There is no consensus in the literature on the structure or binding energy of the OCS dimer. Molecular beam deflection studies by Lobue et al. [13] indicate that the dimer is polar, while IR absorption measurements by Randall et al. [12] conclude that the dimer is centrosymmetric. These conflicting results suggest the possibility that multiple, stable isomers of the dimer exist. **Ab initio** calculations by Bone suggest that the geometry reported by Randall et al. is the global minimum [11]; however, these calculations were restricted to planar geometries. Three configurations investigated in that study are shown in Fig. 7.3. All three structures correspond to stable points on the **ab initio** potential surface, and the configuration in Fig. 7.3(a) is most similar to the geometry reported by Randall et al. In two configurations the monomers are arranged antiparallel, one with the sulfur atoms internal, the other with the oxygen atoms internal. In the third configuration the monomers are parallel to one another. The energetics of these structures are given in Table 7.1. As discussed in the next section, we use these structures and energies as reference points for assessing the accuracy of the solvent-solvent interactions in our model potential.

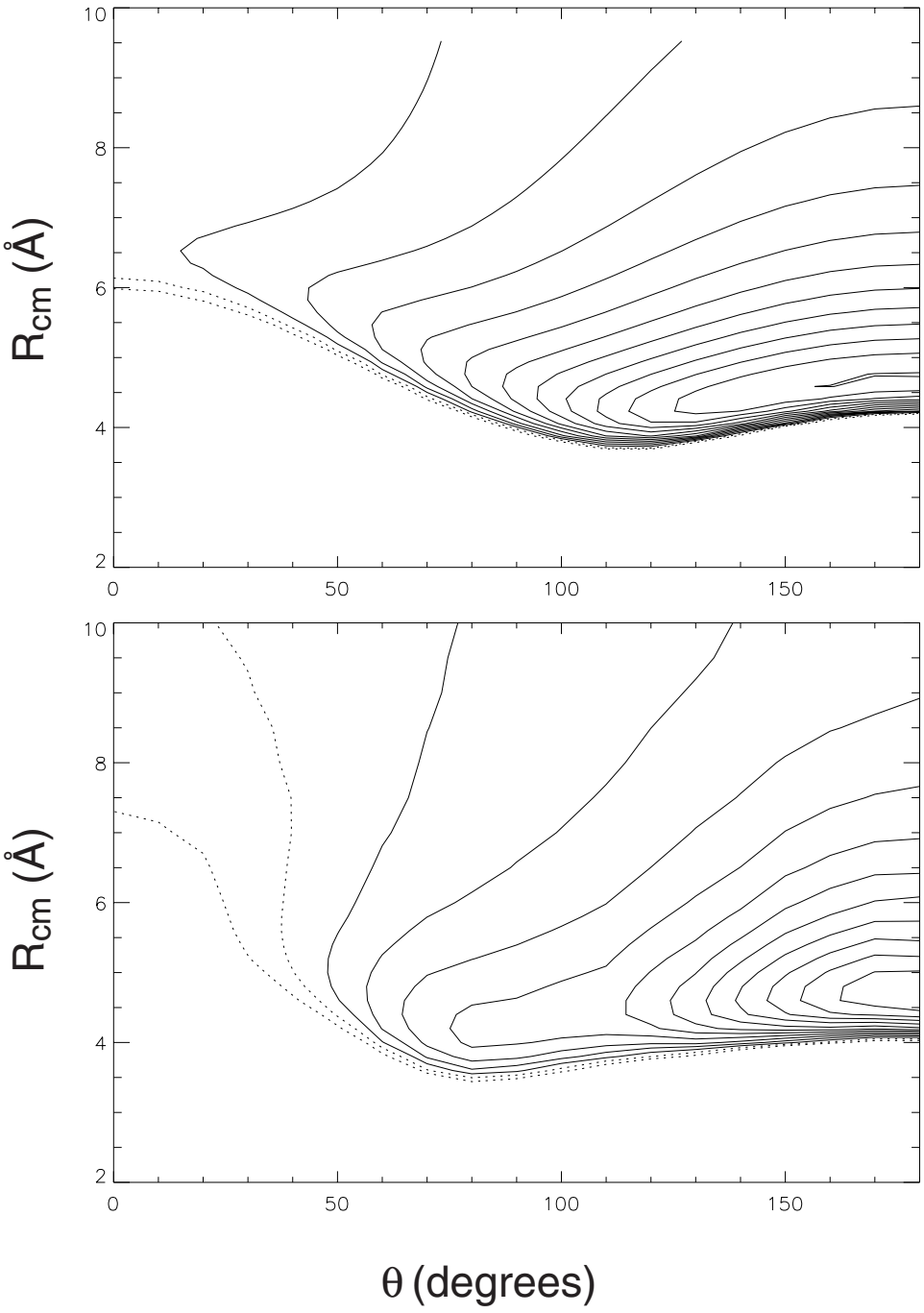

Figure 7.2: Two-dimensional contour plots of the I^-(OCS) potential from (a) our interaction model, and (b) the electronic structure calculation of Ref. 1.

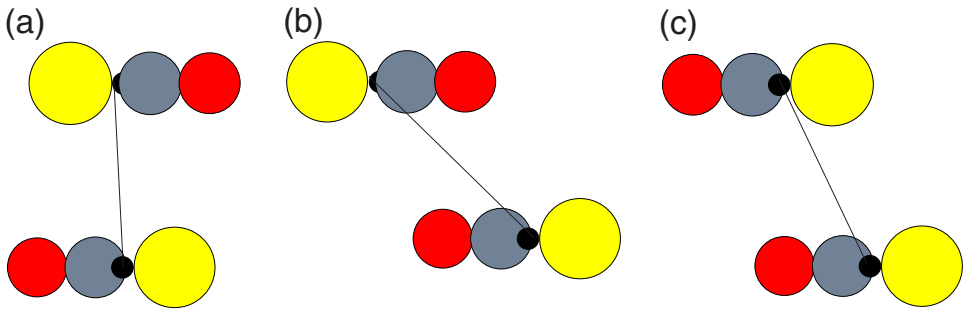

Figure 7.3: Stable structures for the OCS dimer calculated by Bone.

Table 7.2: Model parameters for OCS

atom	charge (a.u.)	Lennard-Jones parameters for interaction with I	
		σ (a.u.)	ϵ (a.u.)
O	-0.07663	8.5	6×10^{-4}
C	+0.03816	8.5	6×10^{-4}
S	+0.03847	7.1	6×10^{-4}

7.3 Fitting Parameters

We assign a three point charge model for OCS by solving a system of linear equations for the charge, dipole and quadrupole moments of OCS, which are 0, 0.7152 D and -0.79 D Å, respectively [14]. The resulting charges on each nucleus are listed in Table 7.2. We note that this is an overly simple method for selecting point charges and we do not expect it to describe the OCS charge distribution accurately; however, it serves as a starting point. The molecular polarizability, $\alpha = 5.21$ Å^3 and the polarizability anisotropy, $\gamma = 4.67$ Å^3 [14], were used to determine the parallel and perpendicular polarizabilities of 58.5 au and 25.7 au, respectively.

With this model for OCS, we calculate the electrostatic and induction energy of linear I^-—SCO as a function of the I—S distance. In this case, the charge distribution of I^- is also classical and is modeled by a single charge of $-e$ at the iodine nucleus. The Coulombic interaction energy for this system is shown in Fig. 7.4.

The basic method of handling the short-range interactions places isotropic, pair-

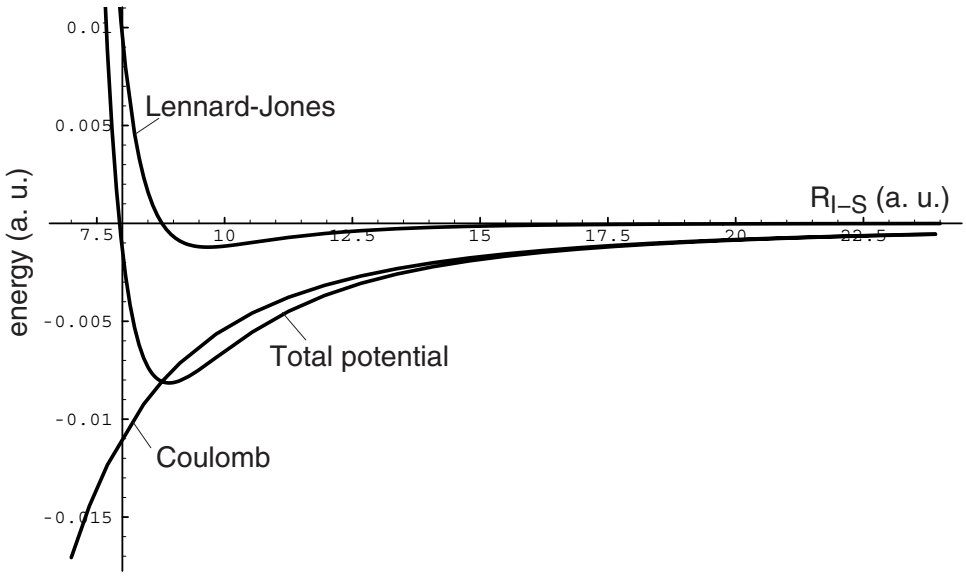

Figure 7.4: Sum of long-range and short-range contributions to model interaction potential, with parameters fit to reproduce the calculated equilibrium I^-—S distance of 3.6 Å and well depth of 220 meV.

wise Lennard-Jones (LJ) sites on all the nuclei,

$$\hat{H}^{\rm sr} = \sum_{ij}{}' \, 4\epsilon_{ij} \left(\frac{\sigma_{ij}^{12}}{R_{ij}^{12}} - \frac{\sigma_{ij}^{6}}{R_{ij}^{6}} \right), \tag{7.1}$$

where the indices i and j run over all the atomic sites in the system, and the sum is restricted to include only pairs where the sites reside on different molecules. Since the global minimum of the I^-(OCS) potential corresponds to a linear configuration with sulfur nearest I^-, we expect σ_{IS} and ϵ_{IS} to be the most important parameters in determining the short-range interaction potential. Initially, we used the I–O and I–C parameters fit for $I_2^-(CO_2)_n$ clusters and varied the I–S parameters to reproduce the equilibrium geometry determined by the electronic structure calculation. The well depth and equilibrium bondlength of the total potential in Fig. 7.4 are 220 meV and 3.6 Å, as desired.

Next, we sought to reproduce secondary features of the calculated potential using the same general technique, but mapping the surface in two dimensions: $\mathbf{R}$ is the distance from I^- to the OCS center of mass, and θ is the angle between $\mathbf{R}$ and the

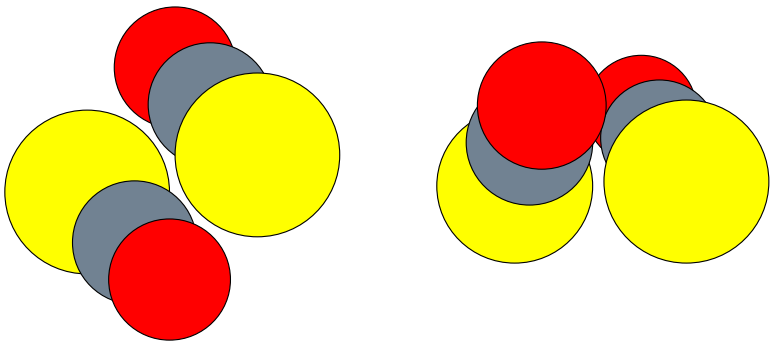

Figure 7.5: Structures for the OCS dimer calculated from the model interaction potential. (a) Planar, bound by 60 meV. (b) Nonplanar, bound by 65 meV.

O–C bond. The I–O and I–C parameters given in Table 7.2 were selected to create a repulsive potential as I^- approaches the O end of OCS and to match the energy of the t-shaped configuration found in the **ab initio** calculation. However, the shape of the model potential, seen in Fig. 7.2, clearly differs from the ab initio potential. In particular, bending about the I^-–SCO minimum is too facile in the model potential. Consequently, the I_2^-(OCS) binding energy is about 230 meV, considerably larger than determined from the electronic structure calculation [1]. Experimentation with a wide range of Lennard-Jones parameters indicated that the angular dependence of the I^-(OCS) potential cannot be significantly improved in this manner. Alternatively, we propose improving the crude electrostatic model for OCS, as discussed below.

Lennard-Jones parameters for OCS–OCS interactions were taken from simulations of liquid OCS [15, 16]. Table 7.1 compares the energy of the OCS dimer calculated by our model potential to the MP2/TZ2P BSSE-corrected results of Bone's **ab initio** calculation at three of the geometries considered in that work [11]. While the agreement is not too bad, none of these geometries correspond to minima on our potential surface. We find two low-lying minima, shown in Fig. 7.5. The structure on the left is bound by about 60 meV, comparable to the minimum calculated by Bone, but the second structure is X-shaped (nonplanar) and bound by 65 meV. At this point it is

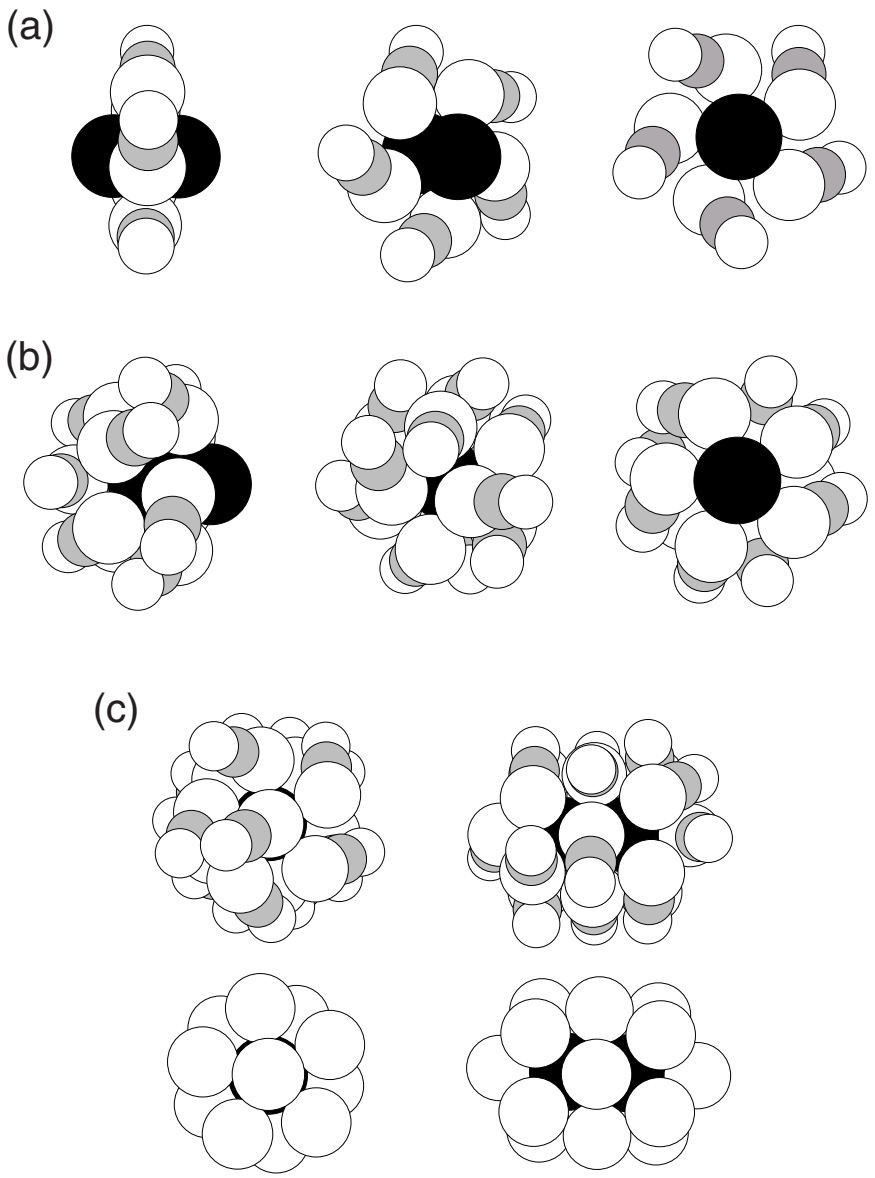

Figure 7.6: Calculated structures for $I_2^-(OCS)_n$ clusters. (a) $n = 5$. (b) $n = 11$. (c) $n = 17$, also shown with C and O removed.

unclear whether this is an artifact of our potential model or if this isomer exists.

7.4 Results for $I_2^-(OCS)_n$

Using the above model to determine structures for $I_2^-(OCS)_n$, we find that OCS molecules arrange themselves first about the waist of I_2^- with the sulfur ends nearest

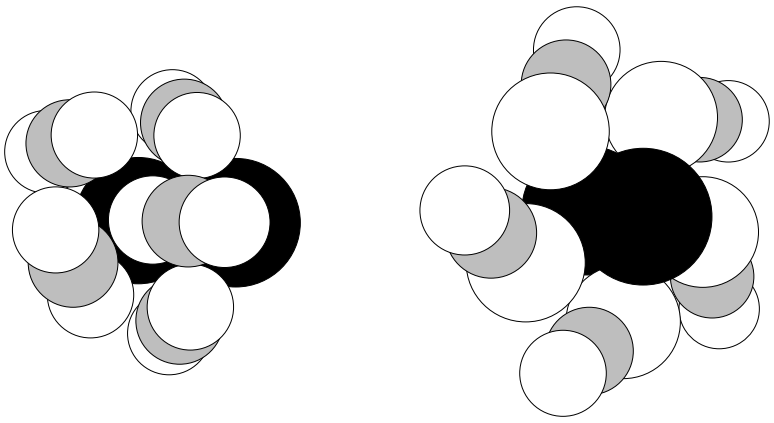

Figure 7.7: Comparison of cluster structures for $I_2^-(CO_2)_5$ and $I_2^-(OCS)_5$.

the solute. The solvent molecules are tilted towards one another, rather than pointing radially outward, see Fig. 7.6(a). The sulfur atoms are 3.57 Å from the I_2^- center of mass. Five OCS molecules complete a ring around I_2^-. Additional OCS molecules form a second ring around one end of the solute, then a single OCS molecule fills the axial site, completing the half-shell structure shown in Fig. 7.6(b). The other side is filled in the same fashion, completing the first solvent shell at $n = 17$, shown in Fig. 7.6(c). The $n = 17$ structures are also shown with carbon and oxygen removed to reveal the underlying structure.

In contrast, for $I_2^-(CO_2)_n$ clusters, discussed in Chapter 3, the dominant charge-quadrupole interactions result in CO_2 molecules lying flat with respect to I_2^-. In small clusters, CO_2 molecules pack together on one side of the I_2^- core rather than forming a ring. A comparison of the $n = 5$ cluster for the two solvents is shown in Fig. 7.7.

In the current model, the I_2^-–(OCS) interaction energy is overestimated. As the model improves, and this energy is reduced, we expect the OCS–OCS interaction to become more important in determining the packing of solvent molecules around I_2^-. For the model described here, secondary minima for the I_2^-–$(OCS)_5$ cluster feature solvent molecules clustered on one side of I_2^- rather than forming a ring structure. The energy

of this configuration is -1.17 eV, compared to -1.21 eV for the ring structure. However, OCS is fundamentally different from CO_2 in that OCS points carbon and oxygen away from I_2^- while CO_2 lies on its side with carbon nearest the solute. Overall, we expect that the underlying structure of sulfur atoms in $n = 17$ will persist as the model is improved, but the tilt of OCS could change significantly, and we would not be surprised to see smaller clusters with OCS molecules localized on one side of I_2^-.

We have performed limited studies of the dynamics with this model. Photodissociation simulations of I_2^-–$(OCS)_6$ at 790 nm were computed for an ensemble of 100 trajectories. We observed 70% caging, compared to 40% caging in the experiment [1]. This tells us that the interaction model is inadequate, but doesn't tell us what needs to be improved. However, we expect that the three point charge model for the OCS charge distribution is the weakest aspect of the current model.

7.5 Recommendations for Improving the Model

We have not found a five point charge model for OCS in the literature, however, Randall et al. report a five point distributed multipole expansion for the OCS charge distribution which includes charge, dipole and quadrupole moments [12]. The current implementation of our model is not coded to compute the long-range interaction terms of order R^{-5}, which would be required to include the quadrupole-quadrupole contributions to the interaction. This would be a straightforward modification, but the disadvantage would be a considerable increase in the computing time required. This could prove to be prohibitive for running dynamics simulations of moderate-sized clusters. Perhaps a better approach would be to develop a five point charge model, derived from the larger multipole expansion.

As a preliminary test, we used the electrostatic model of Randall et al. to calculate the long-range I^-—(SCO) interaction, excluding terms of order R^{-4} and higher and fit I–OCS Lennard-Jones parameters for this model. We were able to greatly improve

the shape of our potential, particularly with regard to stiffening the I^-—SCO bend. The I_2^-(OCS) binding energy was lowered to 160 meV, much closer to the **ab initio** value of 137 meV. Unfortunately, this model gave unreasonable results for the solvent-solvent interactions. We were unable to reproduce any of the reported structures for the OCS dimer, despite attempts to calculate the structures using another program, Orient [17], which is designed to include terms of the order, R^{-5}. The source of error has not been determined, but the general lesson is that an improved model for the OCS charge distribution appears to be the best way to improve the overall interaction potential.

References for Chapter 7

[1] S. Nandi, A. Sanov, N. Delaney, J. Faeder, R. Parson, and W. C. Lineberger, J. Phys. Chem. A **102**, 8827 (1998).

[2] A. Sanov, T. Sanford, S. Nandi, and W. C. Lineberger, J. Chem. Phys. **111**, 663 (1999).

[3] A. Sanov and W. C. Lineberger, private communication.

[4] A. Sanov, S. Nandi, and W. C. Lineberger, J. Chem. Phys. **108**, 5155 (1998).

[5] A. J. Stone, The Theory of Intermolecular Forces, Oxford, New York, 1996.

[6] J. Faeder, N. Delaney, P. Maslen, and R. Parson, Chem. Phys. **239**, 525 (1998).

[7] C. S. Murthy, K. Singer, and I. R. McDonald, Mol. Phys. **44**, 135 (1981).

[8] N. Delaney, J. Faeder, P. E. Maslen, and R. Parson, J. Phys. Chem. A **101**, 8147 (1997).

[9] Y. Zhao, C. C. Arnold, and D. M. Neumark, J. Chem. Soc. Faraday Trans. **89**, 1449 (1993).

[10] Y. Zhao, I. Yourshaw, G. Reiser, C. C. Arnold, and D. M. Neumark, J. Chem. Phys. **101**, 6538 (1994).

[11] R. G. A. Bone, Chem. Phys. Lett. **206**, 260 (1993).

[12] R. W. Randall, J. M. Willkie, B. J. Howard, and J. S. Muenter, Mol. Phys. **69**, 839 (1990).

[13] J. M. Lobue, J. K. Rice, and S. E. Novick, Chem. Phys. Lett. **112**, 376 (1984).

[14] C. G. Gray and K. E. Gubbins, Theory of Molecular Fluids, volume 1, Clarendon, Oxford, 1984.

[15] H. Stassen, T. Dorfmüller, and J. Samios, Mol. Phys. **77**, 339 (1992).

[16] J. Samios and H. Stassen, Chem. Phys. **170**, 193 (1993).

[17] ORIENT, a program for studying interactions between molecules by A. J. Stone, A. Dullweber, P. L. A. Popelier, and D. J. Wales, version 3.2 (1995).

Bibliography

[1] M. Alexander, N. Levinger, M. Johnson, D. Ray, and W. C. Lineberger, Recombination of Br_2^- photodissociated within mass selected ionic clusters, J. Chem. Phys. **88**, 6200 , (1988).

[2] M. L. Alexander, Photodissociation Studies of Mass-Selected Ionic Clusters, PhD thesis, University of Colorado, 1987.

[3] J. Alfano, Y. Kimura, P. K. Walhout, and P. F. Barbara, Photodissociation and vibrational relaxation of I_2^- in water, ethanol, and ethanol-d_1, Chem. Phys. **175**, 147 , (1993).

[4] M. P. Allen and D. J. Tildesley, Computer Simulation of Liquids, Clarendon Press, Oxford, 1987.

[5] F. G. Amar and L. Perera, Energetics and structure in $I_2^-(CO_2)_n$ clusters, Z. Phys. D **20**, 173 , (1991).

[6] H. C. Andersen, Rattle: A "velocity" version of the Shake algorithm for molecular dynamics calculations, J. Comput. Phys. **52**, 24 , (1982).

[7] D. W. Arnold, S. E. Bradforth, E. H. Kim, and D. M. Neumark, Study of halogen-carbon dioxide clusters and the fluoroformyloxyl radical by photodetachment of $X^-(CO_2)$ (X=I, Cl, Br) and FCO_2^-, J. Chem. Phys. **102**, 3493 , (1995).

[8] D. W. Arnold, S. E. Bradforth, E. H. Kim, and D. M. Neumark, Study of $I^-(CO_2)_n$, $Br^-(CO_2)_n$, and $I^-(N_2O)_n$ clusters by anion photoelectron spectroscopy, J. Chem. Phys. **102**, 3510 , (1995).

[9] G. Ashkenazi, U. Banin, A. Bartana, R. Kosloff, and S. Ruhman, Quantum description of the impulsive photodissociation dynamics of I_3^- in solution, Adv. Chem. Phys. **100**, 317 , (1997).

[10] K. R. Asmis, T. R. Taylor, C. S. Xu, and D. M. Neumark, Anion photoelectron spectroscopy of I_2^- and $I_2^-Ar_n$ (n = 1-14, 16, 20) clusters, J. Chem. Phys. **109** , (1998).

[11] U. Banin, A. Bartana, S. Ruhman, and R. Kosloff, Impulsive excitation of coherent vibrational motion ground surface dynamics induced by intense short pulses, J. Chem. Phys. **101**, 8461 , (1994).

[12] U. Banin, R. Kosloff, and S. Ruhman, Vibrational relaxation of nascent diiodide ions studied by femtosecond transient resonance impulsive stimulated Raman scattering (TRISRS); experiment and simulation, Chem. Phys. **183**, 289 , (1994).

[13] U. Banin and S. Ruhman, Ultrafast photodissociation of I_3^-. coherent photochemistry in solution, J. Chem. Phys. **98**, 4391 , (1993).

[14] U. Banin and S. Ruhman, Ultrafast vibrational dynamics of nascent diiodide fragments studied by femtosecond transient resonance impulsive stimulated Raman scattering, J. Chem. Phys. **99**, 9318 , (1993).

[15] U. Banin, A. Waldman, and S. Ruhman, Ultrafast photodissociation of I_3^- in solution: Direct observation of coherent product vibrations, J. Chem. Phys. **96**, 2416 , (1992).

[16] V. S. Batista and D. F. Coker, Nonadiabatic molecular dynamics simulation of ultrafast pump- probe experiments on I_2 in solid rare gases, J. Chem. Phys. **106**, 6923 , (1997).

[17] V. S. Batista and D. F. Coker, Nonadiabatic molecular dynamics simulations of the photofragmentation and geminate recombination in size-selected $I_2^-Ar_n$ clusters, J. Chem. Phys. **106**, 7102 , (1997).

[18] V. S. Batista, M. T. Zanni, B. J. Greenblatt, D. M. Neumark, and W. Miller, Femtosecond photoelectron spectroscopy of the I_2^- anion: A semiclassical molecular dynamics simulation method, JCP **110**, 3736 , (1999).

[19] A. V. Benderskii, R. Zadoyan, and V. A. Apkarian, Caged spin-orbit excited $I^*(^2P_{1/2})$ + $I^*(^2P_{1/2})$ atom piars in liquids and in cryogenic matrices: Spectroscopy and dipolar quenching, J. Chem. Phys. **107**, 8437 , (1997).

[20] I. Benjamin, U. Banin, and S. Ruhman, Ultrafast photodissociation of I_3^- in ethanol: A molecular dynamics study, J. Chem. Phys. **98**, 8337 , (1993).

[21] I. Benjamin, P. F. Barbara, B. J. Gertner, and J. T. Hynes, Nonequilibrium free energy functions, recombination dynamics, and vibration relaxation of I_2^- in acetonitrile: Molecular dynamics of charge flow in the electronically adiabatic limit, J. Phys. Chem. **99**, 7557 , (1995).

[22] I. Benjamin and R. M. Whitnell, Vibrational relaxation of I_2^- in water and ethanol: Molecular dynamics simulation, Chem. Phys. Lett. **204**, 45 , (1993).

[23] R. Bianco and J. T. Hynes, VB resonance theory in solution. I. Multistate formulation, J. Chem. Phys. **102**, 7864 , (1995).

[24] R. Bianco and J. T. Hynes, VB resonance theory in solution. II. I_2^- to or from I $+ I^-$ in acetonitrile, J. Chem. Phys. **102**, 7885 , (1995).

[25] R. Bianco, J. J. I. Timoneda, and J. T. Hynes, Equilibrium and nonequilibrium solvation and solute electronic structure. 4. quantum theory in a multidiabatic state formulation., J. Phys. Chem. **98**, 12103 , (1994).

[26] R. G. A. Bone, An investigation of the structure of weakly bound $(OCS)_2$, Chem. Phys. Lett. **206**, 260 , (1993).

[27] D. Booth and R. M. Noyes, J. Am. Chem. Soc. **82**, 1868 , (1960).

[28] E. C. M. Chen, J. G. Dojahn, and W. E. Wentworth, Characterization of homonuclear diatomic ions by semiempirical Morse potential energy curves. 2. The rare gas positive ions, J. Phys. Chem. A **101**, 3088 , (1997).

[29] E. C. M. Chen and W. E. Wentworth, Negative ion states of the halogens, J. Phys. Chem. **89**, 4099 , (1985).

[30] T. Chuang, G. Hoffman, and K. Eisenthal, Picosecond studies of the cage effect and collision induced predissociation of iodine in liquids, Chem. Phys. Lett. **25**, 201 , (1974).

[31] N. Delaney, J. Faeder, P. E. Maslen, and R. Parson, Photodissociation, recombination and electron transfer in cluster ions: A nonadiabatic molecular dynamics study of $I_2^-(CO_2)_n$, J. Phys. Chem. A **101**, 8147 , (1997).

[32] N. Delaney, J. Faeder, and R. Parson, Simulation of uv photodissociation of $I_2^-(CO_2)_n$: Spin-orbit quenching via solvent mediated electron transfer, J. Chem. Phys. **111**, 651 , (1999).

[33] J. G. Dojahn, E. C. M. Chen, and W. E. Wentworth, Characterization of homonuclear diatomic ions by semiempirical Morse potential energy curves. 1. The halogen atoms, J. Phys. Chem. **100**, 9649 , (1996).

[34] R. Englman, The Jahn-Teller Effect in Molecules and Crystals, Wiley-Interscience, 1972.

[35] J. Faeder, The X_2^- Files: Modeling Structure and Dynamics of Solvated Molecular Ions, PhD thesis, University of Colorado, 1998.

[36] J. Faeder, N. Delaney, P. Maslen, and R. Parson, Charge flow and solvent dynamics in the photodissociation of cluster ions: A nonadiabatic molecular dynamics study of $I_2^- \cdot Ar_n$, Chem. Phys. Lett. **270**, 196 , (1997).

[37] J. Faeder, N. Delaney, P. Maslen, and R. Parson, Modeling structure and dynamics of solvated molecular ions: Photodissociation and recombination in $I_2^- \cdot (CO_2)_n$, Chem. Phys. **239**, 525 , (1998).

[38] J. Faeder and R. Parson, Dynamics of $ICl^-(CO_2)_n$ photodissocia tion , in preparation.

[39] J. Faeder and R. Parson, Ultrafast reaction dynamics in cluster ions: Simulation of the transient photoelectron spectrum of $I_2^- Ar_n$ photodissociation, J. Chem. Phys. **108**, 3909 , (1998).

[40] J. Franck and E. Rabinowitch, Trans. Faraday Soc. **30**, 120 , (1934).

[41] E. Gershgoren, U. Banin, and S. Ruhman, Caging and geminate recombination following photolysis of triiodide in solution, J. Phys. Chem. A **102**, 9 , (1998).

[42] B. J. Gertner, K. Ando, R. Bianco, and J. T. Hynes, Bihalide ion combination reactions in solution: Electronic structure and solvation aspects, Chem. Phys. **183**, 309 , (1994).

[43] C. G. Gray and K. E. Gubbins, Theory of Molecular Fluids, volume 1, Clarendon, Oxford, 1984.

[44] B. J. Greenblatt, Femtosecond Photoelectron Spectroscopy: A New Tool for the Study of Anion Dynamics, PhD thesis, University of California, 1999.

[45] B. J. Greenblatt, M. T. Zanni, and D. M. Neumark, Photodissociation dynamics of the I_2^- anion using femtosecond photoelectron spectroscopy, Chem. Phys. Lett. **258**, 523 , (1996).

[46] B. J. Greenblatt, M. T. Zanni, and D. M. Neumark, Time-resolved photodissociation dynamics of $I_2^- Ar_n$ clusters using anion femtosecond photoelectron spectroscopy, Science **276**, 1675 , (1997).

[47] B. J. Greenblatt, M. T. Zanni, and D. M. Neumark, Time-resolved studies of dynamics in molecular and cluster anions, Faraday Discuss. **108**, 101 , (1997).

[48] S. Hammes-Schiffer, Mixed quantum/classical dynamics of hydrogen transfer reactions, J. Phys. Chem. A **102**, 10444 , (1998).

[49] S. Hammes-Schiffer and J. C. Tully, Proton transfer in solution: Molecular dynamics with quantum transitions, J. Chem. Phys. **101**, 4657 , (1994).

[50] D. Husain and R. J. Donovan, Electronically excited halogen atoms, in Advances in Photochemistry, edited by J. N. Pitts, Jr, G. S. Hammond, and W. A. Noyes, Jr, volume 8, pp. 1–75, Wiley-Interscience, New York, 1971.

[51] A. E. Johnson, N. E. Levinger, and P. F. Barbara, Photodissociation dynamics of I_2^- in water and alcohols, J. Phys. Chem. **96**, 7841 , (1992).

[52] H. J. Kim and J. T. Hynes, Equilibrium and nonequilibrium solvation and solute electronic structure. I. Formulation, J. Chem. Phys. **93**, 5194 , (1990).

[53] H. J. Kim and J. T. Hynes, Equilibrium and nonequilibrium solvation and solute electronic structure. III. Quantum theory, J. Chem. Phys. **96**, 5088 , (1992).

[54] D. A. V. Kliner, J. C. Alfano, and P. F. Barbara, Photodissociation and vibrational relaxation of I_2^- in ethanol, J. Chem. Phys. **98**, 5375 , (1993).

[55] A. I. Krylov, R. B. Gerber, and R. D. Coalson, Nonadiabatic dynamics and electronic energy relaxation of Cl (^2P) atoms in solid Ar, J. Chem. Phys. **105**, 4626 , (1996).

[56] B. M. Ladanyi and R. Parson, Structure and dynamics of molecular ions in clusters: I_2^- in flexible CO_2, J. Chem. Phys. **107**, 9326 , (1997).

[57] F. W. Lampe and R. M. Noyes, J. Am. Chem. Soc. **76**, 2140 , (1954).

[58] N. E. Levinger, Spectroscopy and Dynamics of Large Cluster Ions, PhD thesis, University of Colorado, 1990.

[59] C. Lienau and A. Zewail, Femtochemistry at high pressures. Solvent effect in the gas- to-liquid transition region, Chem. Phys. Lett. **222**, 224 , (1994).

[60] Q. Liu, J.-K. Wang, and A. H. Zewail, Femtosecond dynmaics of dissociation and recombination in solvent cages, Nature **364**, 427 , (1993).

[61] Q. Liu, J.-K. Wong, and A. H. Zewail, Solvation ultrafast dynamics of reactions. 10. Molecular dynamics studies of dissociation, recombination, and coherence, J. Phys. Chem. **99**, 11321 , (1995).

[62] J. M. Lobue, J. K. Rice, and S. E. Novick, Qualitative structure of $(CO_2)_2$ and $(OCS)_2$, Chem. Phys. Lett. **112**, 376 , (1984).

[63] R. A. Marcus, Ann. Rev. Phys. Chem. **15**, 155 , (1964).

[64] R. A. Marcus, Faraday Symp. Chem. Soc. **10**, 60 , (1975).

[65] R. A. Marcus, Schrödinger equation for a strongly coupled electron transfer system, J. Phys. Chem. **96**, 1753 , (1992).

[66] C. Margulis and D. F. Coker, Nonadiabatic molecular dynamics simulations of the photofragmentation and geminate recombination in size-selected $I_2^-(CO_2)_n$ clusters, J. Chem. Phys. **110**, 5677 , (1999).

[67] P. E. Maslen, J. Faeder, and R. Parson, Ab initio calculations of the ground and excited states of I_2^- and ICl^-, Chem. Phys. Lett. **263**, 63 , (1996).

[68] P. E. Maslen, J. Faeder, and R. Parson, An effective Hamiltonian for an electronically excited solute in a polarisable molecular solvent, Mol. Phys. **94**, 693 , (1998).

[69] P. E. Maslen, J. M. Papanikolas, J. Faeder, R. Parson, and S. V. ONeil, Solvation of electronically excited I_2^-, J. Chem. Phys. **101**, 5731 , (1994).

[70] L. F. Meadows and R. M. Noyes, J. Am. Chem. Soc. **82**, 1872 , (1960).

[71] C. S. Murthy, S. F. O'Shea, and I. R. McDonald, Electrostatic interactions in molecular crystals: Lattice dynamics of solid nitrogen and carbon dioxide, Mol. Phys. **50**, 531 , (1983).

[72] C. S. Murthy, K. Singer, and I. R. McDonald, Interaction site models for carbon dioxide, Mol. Phys. **44**, 135 , (1981).

[73] M. Nadal, The Study of the Photodissociation and Recombination Dynamics of Mass-Selected Cluster Ions: Solvent Effects on the Structure and Dynamics of the Ionic Chromophore, PhD thesis, University of Colorado, 1996.

[74] M. E. Nadal, P. D. Kleiber, and W. C. Lineberger, Photofragmentation of mass-selected $ICl^-(CO_2)_n$ cluster ions: Solvation effects on the structure and dynamics of the ionic chromophore, J. Chem. Phys. **105**, 504 , (1996).

[75] M. E. Nadal, S. Nandi, D. W. Boo, and W. C. Lineberger, Photodissociation and recombination dynamics of I_2^- in N_2O clusters, J. Chem. Phys. , (1998), to be submitted.

[76] S. Nandi, A. Sanov, N. Delaney, J. Faeder, R. Parson, and W. C. Lineberger, Photodissociation of $I_2^-(OCS)_n$ cluster ions: Structural implications, J. Phys. Chem. A **102**, 8827 , (1998).

[77] D. J. Nesbitt and J. T. Hynes, Slow vibrational relxation in picosecond iodine recombination in liquids, J. Chem. Phys. **77**, 2130 , (1982).

[78] M. D. Newton and N. Sutin, Electron transfer reactions in condensed phases, Ann. Rev. Phys. Chem. **35**, 437 , (1984).

[79] ORIENT, a program for studying interactions between molecules by A. J. Stone, A. Dullweber, P. L. A. Popelier, and D. J. Wales, version 3.2 (1995).

[80] J. Papanikolas, J. Gord, N. Levinger, D. Ray, V. Vorsa, and W. C. Lineberger, Photodissociation and geminate recombination dynamics of I_2^- in mass-selected $I_2^-(CO_2)_n$ cluster ions, J. Phys. Chem. **95**, 8028 , (1991).

[81] J. Papanikolas, V. Vorsa, M. Nadal, P. Campagnola, H. Buchenau, and W. C. Lineberger, I_2^- photodissociation and recombination dynamics in size-selected $I_2^-(CO_2)_n$ cluster ions, J. Chem. Phys. **99**, 8733 , (1993).

[82] J. Papanikolas, V. Vorsa, M. Nadal, P. Campagnola, J. Gord, and W. C. Lineberger, I_2^- photofragmentation/recombination dynamics in size-selected $I_2^-(CO_2)_n$ cluster ions: Observation of coherent I...I^- vibrational motion, J. Chem. Phys. **97**, 7002 , (1992).

[83] J. M. Papanikolas, I_2^- Photodissociation and Cage Recombination Dynamics in Size-Selected $I_2^-(CO_2)_n$ Clusters, PhD thesis, University of Colorado, 1994.

[84] J. M. Papanikolas, P. E. Maslen, and R. Parson, Recombination and relaxation of molecular ions in size-selected clusters: Monte Carlo and molecular dynamics simulations of $I_2^-(CO_2)_n$, J. Chem. Phys. **102**, 2452 , (1995).

[85] R. Parson and J. Faeder, Ultrafast reaction dynamics in molecular cluster ions, Science **276**, 1660 , (1997).

[86] L. Perera and F. G. Amar, Charge localization in negative ion dynamics: Effect on caging of Br_2^- in Ar_n and $(CO_2)_n$ clusters, J. Chem. Phys. **90**, 7354 , (1989).

[87] S. L. Price, A. J. Stone, and M. Alderton, Explicit formulae for the electrostatic energy, forces and torques between a pair of molecules of arbitrary symmetry, Mol. Phys. **52**, 987 , (1984).

[88] R. W. Randall, J. M. Willkie, B. J. Howard, and J. S. Muenter, Infrared vibration-rotation spectrum and structure of OCS dimer, Mol. Phys. **69**, 839 , (1990).

[89] D. Ray, N. Levinger, J. Papanikolas, and W. C. Lineberger, Time-resolved measurements of the photodissociation and recombination dynamics of I_2^- in mass selected cluster ions, J. Chem. Phys. **91**, 6533 , (1989).

[90] J. Samios and H. Stassen, Time correlation functions of liquid OCS. a molecular dynamics simulation study, Chem. Phys. **170**, 193 , (1993).

[91] A. Sanov, S. Nandi, and W. C. Lineberger, Transient solvent dynamics and incoherent control of photodissociation pathways in I_2^- cluster ions, J. Chem. Phys. **108**, 5155 , (1998).

[92] A. Sanov, T. Sanford, S. Nandi, and W. C. Lineberger, Spin-orbit relaxation and recombination dynamics in $I_2^-(CO_2)_n$ and $I_2^-(OCS)_n$ cluster ions, J. Chem. Phys. **111**, 663 , (1999).

[93] G. C. Schatz and M. A. Ratner, Quantum Mechanics in Chemistry, chapter 10, Prentice Hall, Englewood Cliffs, 1993.

[94] R. J. Silbey, Electronic energy transfer in molecular crystals, Ann. Rev. Phys. Chem. **27**, 203 , (1976).

[95] H. Stassen, T. Dorfmüller, and J. Samios, Molecular dynamics investigations of the electrostatic interactions in liquid carbonyl sulfide, Mol. Phys. **77**, 339 , (1992).

[96] A. J. Stone, Distributed multipole analysis, or how to describe a molecular charge distribution, Chem. Phys. Lett. **83**, 233 , (1981).

[97] A. J. Stone, The Theory of Intermolecular Forces, Oxford, New York, 1996.

[98] J. C. Tully, Nonadiabatic processes in molecular collisions, in Dynamics of Molecular Collisions, edited by W. H. Miller, volume Part B, Plenum, New York, 1976.

[99] J. C. Tully, Molecular dynamics with electronic transitions, J. Chem. Phys. **93**, 1061 , (1990).

[100] L. Verlet, Computer "experiments" on classical fluids. I. Thermodynamical properties of Lennard-Jones molecules, Phys. Rev. **159**, 98 , (1967).

[101] V. Vorsa, Photodissociation Dynamics of Mass-Selected Anions and Anionic Clusters, PhD thesis, University of Colorado, 1996.

[102] V. Vorsa, P. J. Campagnola, S. Nandi, M. Larsson, and W. C. Lineberger, Photofragmentation of $I_2^- \cdot Ar_n$ clusters: Observation of metastable isomeric ionic fragments, J. Chem. Phys. **105**, 2298 , (1996).

[103] V. Vorsa, S. Nandi, P. J. Campagnola, M. Larsson, and W. C. Lineberger, Recombination dynamics of photodissociated I_2^- in size selected Ar and CO_2 clusters, J. Chem. Phys. **106**, 1402 , (1997).

[104] P. K. Walhout, J. C. Alfano, K. A. M. Thakur, and P. F. Barbara, Ultrafast experiments on the photodissociation, recombination, and vibrational relaxation of I_2^-: Role of solvent-induced solute charge flow, J. Phys. Chem. **99**, 7568 , (1995).

[105] C. Wan, M. Gupta, J. Baskin, Z. Kim, and A. Zewail, Caging phenomena in reactions: femtosecond observation of coherent, collisional confinement, J. Chem. Phys. **106**, 4353 , (1997).

[106] J.-K. Wong, Q. Liu, and A. H. Zewail, Solvation ultrafast dynamics of reactions. 9. Femtosecond studies of dissociation and recombination of iodine in argon clusters, J. Phys. Chem. **99**, 11309 , (1995).

[107] Y. Yan, R. Whitnell, K. Wilson, and A. Zewail, Femtosecond chemical dynamics in solution. Wavepacket evolution and caging of I_2, Chem. Phys. Lett. **193**, 402 , (1992).

[108] H. Yasumatsu, U. Kalmbach, S. Koizumi, A. Terasaki, and T. Kondow, Dynamic solvation effects on surface-impact dissociation of $I_2^-(CO_2)_n$, Z. Phys. D **40**, 51 , (1997).

[109] H. Yasumatsu, S. Koizumi, A. Terasaki, and T. Kondow, Energy redistribution in cluster-surface collision: $I_2^-(CO_2)_n$ onto silicon surface, J. Chem. Phys. **105**, 9509 , (1996).

[110] H. Yasumatsu, S. Koizumi, A. Terasaki, and T. Kondow, Energy redistribution in $I_2^-(CO_2)_n$ collision on silicon surface, J. Phys. Chem. A **102** , (1998), in press.

[111] H. Yasumatsu, A. Terasaki, and T. Kondow, Splitting a chemical bond with a molecular wedge via cluster-surface collisions, J. Chem. Phys. **106**, 3806 , (1997).

[112] I. Yourshaw, Y. Zhao, and D. M. Neumark, Many-body effects in weakly bound anion and neutral clusters: Zero electron kinetic energy spectroscopy and threshold photodetachment spectroscopy of Ar_nBr^- (n =2–9) and Ar_nI^- (n =2–19), J. Chem. Phys. **105**, 351 , (1996).

[113] R. Zadoyan, Z. Li, C. Martens, and V. Apkarian, The breaking and remaking of a bond: caging of I_2 in solid Kr, J. Chem. Phys. **101**, 6648 , (1994).

[114] R. Zadoyan, M. Sterling, M. Ovchinnikov, and V. A. Apkarian, Predissociation dynamics of I_2(B) in liquid CCl_4 observed through femtosecond pump-probe measurements: Electronic caging through solvent asymmetry, J. Chem. Phys. **107**, 8446 , (1997).

[115] M. T. Zanni, V. S. Batista, B. J. Greenblatt, W. Miller, and D. M. Neumark, Femtosecond photoelectron spectroscopy of the I_2^- anion: Characterization of the $A'\,^2\Pi_{g,1/2}$ excited state, JCP **110**, 3748 , (1999).

[116] M. T. Zanni, T. R. Taylor, B. J. Greenblatt, B. Soep, and D. M. Neumark, Characterization of the I_2^- anion ground state using conventional and femtosecond photoelectron spectroscopy, J. Chem. Phys. **107**, 7613 , (1997).

[117] Y. Zhao, C. C. Arnold, and D. M. Neumark, Study of the $I{\cdot}CO_2$ van der Waals complex by threshold photodetachment spectroscopy of I^-CO_2, J. Chem. Soc. Faraday Trans. **89**, 1449 , (1993).

[118] Y. Zhao, I. Yourshaw, G. Reiser, C. C. Arnold, and D. M. Neumark, Study of the $ArBr^-$, ArI^-, and KrI^- anions and the corresponding neutral van der Waals complexes by anion zero electron kinetic energy spectroscopy, J. Chem. Phys. **101**, 6538 , (1994).

[119] J. Zimmerman and R. M. Noyes, J. Chem. Phys. **21**, 2086 , (1950).

Appendix A

The Blind Men and the Elephant

A Hindu parable set in verse by John Godfrey Saxe (1816-1887)

It was six men of Indostan
To learning much inclined,
Who went to see the Elephant
(Though all of them were blind),
That each by observation
Might satisfy his mind.

The First approached the Elephant,
And happening to fall
Against his broad and sturdy side,
At once began to bawl:
'God bless me! but the Elephant
Is very like a wall!'

The Second, feeling of the tusk,
Cried, 'Ho! what have we here
So very round and smooth and sharp?
To me 'tis mighty clear
This wonder of an Elephant
Is very like a spear!'

The Third approached the animal,
And happening to take
The squirming trunk within his hands,
Thus boldly up and spake:
'I see,' quoth he, 'the Elephant
Is very like a snake.'

The Fourth reached out his eager hand,
And felt about the knee.
'What most this wondrous beast is like

Is mighty plain,' quoth he;
''Tis clear enough the Elephant
Is very like a tree!'

The Fifth who chanced to touch the ear,
Said: 'E'en the blindest man
Can tell what this resembles most:
Deny the fact who can,
This marvel of an Elephant
Is very like a fan!'

The Sixth no sooner had begun
About the beast to grope,
Than, seizing on the swinging tail
That fell within his scope,
'I see,' quoth he, 'the Elephant
Is very like a rope!'

And so these men of Indostan
Disputed loud and long,
Each in his own opinion
Exceeding stiff and strong,
Though each was partly in the right,
And all were in the wrong!

So, oft in theologic wars,
The disputants, I ween,
Rail on in utter ignorance
Of what each other mean,
And prate about an Elephant
Not one of them has seen!

Appendix B

Model Hamiltonian for Spin-Orbit Quenching by Charge Transfer

Electron and exciton transfer in condensed media are commonly described by means of semiempirical one-electron Hamiltonians [1–3], which help to identify the key molecular parameters that determine the reaction rate. We present here a model of this type that is suitable for describing the interplay between charge transfer and spin-orbit coupling in solvated dihalide ions. This model provides a Hamiltonian to go along with the qualitative potential curves sketched in Fig. 4, and provides further insight into the mechanism of solvent-induced spin-orbit quenching.

We begin by reviewing the traditional spin-boson Hamiltonian for a two-level electronic system coupled linearly to a single coordinate representing the nuclear degrees of freedom [2–4]. In solution-phase electron transfer this coordinate is usually the solvent orientational polarization [1, 5], while in solid-state electron or exciton transfer it may include both lattice and intramolecular vibrations [2, 3]; in our clusters, it describes the overall motion of the solvent cage from one side of the solute to the other. We will primarily use the language of solution-phase electron transfer in our discussion. We adopt a diabatic representation in which the basis states describe an electron localized on either of two atoms, labelled A and B, having local site energies ϵ_A and ϵ_B. The model Hamiltonian then takes the form:

$$\mathsf{H} = \begin{bmatrix} \epsilon_A & \beta \\ \beta & \epsilon_B \end{bmatrix} + \left(\frac{p^2}{2m} + u(q) \right) \begin{bmatrix} 1 & 0 \\ 0 & 1 \end{bmatrix} + \begin{bmatrix} -\gamma q & 0 \\ 0 & \gamma q \end{bmatrix}, \qquad \text{(B.1)}$$

where β is the electronic resonance integral that parametrizes the chemical bonding interaction between the two sites, q and p are the solvent coordinate and its corresponding momentum, $u(q)$ is the potential energy associated with deforming the solvent configuration, and γ measures the strength of the coupling between the electronic and solvent degrees of freedom. (The product $2\gamma q$, which measures the energy gained by localizing the charge on one site and deforming the solvent around that site, corresponds to the "solvent coordinate" $\Delta\Phi$ used in the main text of this paper.) Eq. B.1 can be rewritten as the sum of an adiabatic electronic hamiltonian H^{el} and a solvent kinetic energy term T:

$$\mathsf{H} = \begin{bmatrix} \epsilon_A + u(q) - \gamma q & \beta \\ \beta & \epsilon_B + u(q) + \gamma q \end{bmatrix} + \left(\frac{p^2}{2m} \right) \begin{bmatrix} 1 & 0 \\ 0 & 1 \end{bmatrix} \equiv \mathsf{H}^{el} + \mathsf{T}, \qquad \text{(B.2)}$$

The diagonal elements of H^{el}, considered as functions of q, trace out the diabatic potential curves, while the eigenvalues of H^{el} yield the corresponding adiabatic curves. If the solvent coordinate is treated as a harmonic oscillator, $u(q)$ is quadratic and the diabatic curves are a pair of displaced parabolas. The resonance coupling β depends strongly (typically exponentially) upon the interatomic separation R. The diabatic representation is most useful at large R, where β is small; in this regime an electronic transition between the diabatic states can be viewed as a charge transfer event. These transitions occur primarily where the diabatic curves cross, $\epsilon_A - \epsilon_B = 2\gamma q$, , with a probability proportional $|\beta|^2$. For a homonuclear diatomic solute, $\epsilon_A = \epsilon_B$ and the diabatic curves cross at q=0.

The Hamiltonian above describes a single electron in a state space that includes one orbital per site. Since the dihalide ions are one electron short of a closed shell, their electronic structure can be described in terms of a single-hole picture which is isomorphic to a one-electron picture; however, the state space must be expanded to include the three valence p-orbitals on each atom. We then have two resonance integrals, β_Σ and β_Π, which correspond to chemical bonding interactions between p-orbitals that are respectively parallel and perpendicular to the internuclear axis. For the time being we neglect spin-orbit coupling. In the localized diabatic representation, the six-state adiabatic electronic Hamiltonian consists of three 2×2 blocks, two of which are degenerate:

$$\begin{bmatrix} \epsilon_A + u(q) - \gamma q & \beta_\Sigma & & & & \\ \beta_\Sigma & \epsilon_B + u(q) + \gamma q & & & & \\ & & \epsilon_A + u(q) - \gamma q & -\beta_\Pi & & \\ & & -\beta_\Pi & \epsilon_B + u(q) + \gamma q & & \\ & & & & \epsilon_A + u(q) - \gamma q & -\beta_\Pi \\ & & & & -\beta_\Pi & \epsilon_B + u(q) + \gamma q \end{bmatrix}. \tag{B.3}$$

The signs of the off-diagonal elements have been chosen so that when β_Σ and β_Π are positive, the sigma-bonding state will have ungerade (u) symmetry while the pi-bonding states will have g-symmetry, as in the actual molecule.

The spin-orbit coupling operator $\zeta \vec{l} \cdot \vec{s}$ mixes the Σ and Π blocks. Because the model Hamiltonian has cylindrical symmetry, we may choose linear combinations within the Π subspace so that only one pair couples to the Σ states; these are the states with a total angular momentum projection $\Omega = \frac{1}{2}$. The $\Omega = \frac{3}{2}$ states remain pure Π states and we leave them out. The resulting four-state electronic Hamiltonian is

$$\mathsf{H}^a = \begin{bmatrix} \epsilon_A + u(q) - \gamma q & \beta_\Sigma & -\frac{\zeta}{\sqrt{2}} & 0 \\ \beta_\Sigma & \epsilon_B + u(q) + \gamma q & 0 & -\frac{\zeta}{\sqrt{2}} \\ -\frac{\zeta}{\sqrt{2}} & 0 & \epsilon_A + u(q) - \gamma q + \frac{\zeta}{2} & -\beta_\Pi \\ 0 & -\frac{\zeta}{\sqrt{2}} & -\beta_\Pi & \epsilon_B + u(q) + \gamma q + \frac{\zeta}{2} \end{bmatrix}. \tag{B.4}$$

We now transform this Hamiltonian from the Hund's Case (a) representation, in which the spin-orbit terms couple basis states that are purely Σ or Π in character, to the Hund's Case (c) representation in which the spin-orbit terms appear on the diagonal. Case (c) is appropriate when the spin-orbit splitting exceeds the resonance coupling, as is always the case at sufficiently large interatomic distances; for isolated I_2^- the electronic wave functions are well described in Hund's Case (c) for R greater than about $6\mathring{A}$ [6]. Since the transformation mixes Σ and Π states, one ends up with localized basis states that interact through linear combinations of β_Σ and β_Π:

$$\mathsf{H}^c = \begin{bmatrix} \epsilon_A + u(q) - \gamma q + \zeta & \frac{1}{3}(\beta_\Sigma - 2\beta_\Pi) & 0 & \frac{\sqrt{2}}{3}(\beta_\Sigma + \beta_\Pi) \\ \frac{1}{3}(\beta_\Sigma - 2\beta_\Pi) & \epsilon_B + u(q) + \gamma q + \zeta & \frac{\sqrt{2}}{3}(\beta_\Sigma + \beta_\Pi) & 0 \\ 0 & \frac{\sqrt{2}}{3}(\beta_\Sigma + \beta_\Pi) & \epsilon_A + u(q) - \gamma q - \frac{1}{2}\zeta & \frac{1}{3}(2\beta_\Sigma - \beta_\Pi) \\ \frac{\sqrt{2}}{3}(\beta_\Sigma + \beta_\Pi) & 0 & \frac{1}{3}(2\beta_\Sigma - \beta_\Pi) & \epsilon_B + u(q) + \gamma q - \frac{1}{2}\zeta \end{bmatrix}. \tag{B.5}$$

The upper 2×2 block of H^c describes the resonance interaction between an I^- ion and an I^* atom, and the lower to the interaction between I^- and I in its spin-orbit ground state. Indeed, one can think of the linear combinations of β_Σ and β_Π as arising from p-orbitals that are tilted away from the internuclear axis by 30 and 60 degrees. The diagonal elements of H^c, considered as functions of q, correspond to the diabatic potential curves in Fig. 4 (although Fig. 4 also includes the $\Pi_{3/2}$ states that have been omitted here). Within each spin-orbit block, charge transfer occurs primarily near q=0 where the diabatic curves cross. However, Eq. B.5 also includes

matrix elements $\frac{\sqrt{2}}{3}(\beta_\Sigma + \beta_\Pi)$ that couple the spin-orbit blocks. Since these matrix elements are also made up from interatomic resonance integrals, they also describe charge-transfer events, and they will become important when the diabatic curves arising from **different** spin-orbit blocks cross, as in Fig. 4. In the homonuclear case ($\epsilon_A = \epsilon_B$) the condition for such a crossing is that

$$\frac{3}{2}\zeta = \pm 2\gamma q \equiv \Delta\Phi, \tag{B.6}$$

i.e., the differential solvation energy is equal to the spin-orbit splitting in the iodine atom. Thus, these are the matrix elements responsible for spin orbit relaxation via solvent-induced charge transfer.

At a given R, we expect that β_Σ will be much larger than β_Π since a p orbital hole that is aligned with the internuclear axis will have a larger overlap with the charge cloud on the I^- ion than one which is aligned perpendicular to that axis. This expectation is confirmed by the relative depths of the Σ and Π state wells in I_2^-: the ground state ($^2\Sigma_{u,1/2}$) is bound by 1.01 eV [7] while the binding energy in the first excited state ($^2\Pi_{g,1/2}$) is estimated to be about 0.1 eV [6]. To a first approximation, we may regard all the charge-transfer events as driven by β_Σ ,whose amplitude is distributed in varying amounts over the spin-orbit coupled Hund's Case (c) states. All of the charge-transfer matrix elements in H^c are then of the same order of magnitude; if anything, the terms associated with charge-transfer between the two spin-orbit manifolds are somewhat larger than those associated with charge transfer in the spin-orbit excited state. Thus there are no matrix-element restrictions on spin-orbit relaxation by charge transfer: the electron hops to whichever orbital is closest in energy. When the two atoms are equally solvated ($q \approx 0$), the charge is transferred within a spin-orbit manifold, but in a highly asymmetric solvent environment ($2\gamma q \approx \pm\frac{3}{2}\zeta$), charge transfer involves a transition between the spin-orbit manifolds.

The model outlined above has one significant unphysical property: the Hamil-

tonian is cylindrically symmetric. This is a result of compressing the solvent effects into a single coordinate that describes only the overall difference between the solvation energies at the two atoms, not the finer details of the complicated electrostatic environment around the solute. When these details are included, as they are in our simulations, Ω is no longer a good quantum number and the electronic Hamiltonian cannot be reduced to four states. As a result the spin-orbit excited states are quenched into all four lower states, rather than into one pair as in the model above. This is seen in the simulations. Aside from this, the Hamiltonian model describes well the overall features of the solvent-mediated spin-orbit quenching mechanism: the process does not occur at all until a threshold value of the solvent coordinate is reached, but once this criterion is met the process is highly efficient.

References for Appendix B

[1] M. D. Newton and N. Sutin, Ann. Rev. Phys. Chem. **35**, 437 (1984).

[2] G. C. Schatz and M. A. Ratner, Quantum Mechanics in Chemistry, chapter 10, Prentice Hall, Englewood Cliffs, 1993.

[3] R. J. Silbey, Ann. Rev. Phys. Chem. **27**, 203 (1976).

[4] R. Englman, The Jahn-Teller Effect in Molecules and Crystals, Wiley-Interscience, 1972.

[5] R. A. Marcus, Ann. Rev. Phys. Chem. **15**, 155 (1964).

[6] P. E. Maslen, J. Faeder, and R. Parson, Chem. Phys. Lett. **263**, 63 (1996).

[7] M. T. Zanni, T. R. Taylor, B. J. Greenblatt, B. Soep, and D. M. Neumark, J. Chem. Phys. **107**, 7613 (1997).